UNIVERSITA' DEGLI STUDI DI PARMA

Dottorato di ricerca in Scienza e Tecnologia dei Materiali Innovativi

Ciclo XXII

MATERIAL ENGINEERING IN HYBRID SPINTRONIC DEVICES

Coordinatore:

Chiar.ma Prof.ssa Anna Painelli

Tutor interno:

Chiar.mo Prof. Massimo Solzi

Tutor esterno:

Chiar.mo Dott. Valentin Dediu

Dottorando: Patrizio Graziosi

Thesis Objectives

The main objectives of this thesis is to achieve an overall progress of the quality of hybrid organic-inorganic devices for spintronic applications by improving the material quality of the main device components. Their list is presented below:

(1) Improving considerably the roughness of the manganite films while keeping high and robust their surface magnetism. This objective is very challenging, as the manganite growth is intrinsically characterized by the formation of outgrowth and other defects. On the other hand, in many cases the reduction of the surface roughness in manganites was accompanied by a significant deterioration of the surface magnetism.

(2) Engineering the interfaces in vertical devices in order to achieve a high efficiency of spin transfer and high reproducibility of devices operation. The fulfillment of this objective requires an initial accurate and deep investigation of the starting interface quality by different available techniques. Further different interface engineering solutions will be investigated.

(3) Achieving a deep and quantitative understanding of the growth process of organic semiconductor films on the most utilized magnetic substrate in organic spintronics – $La_{0.7}Sr_{0.3}MnO_3$ manganite.

(4) Achieving a considerable improvement of the magnetic and structural quality of the top electrodes in vertical devises represented by (magnetic) metals grown on organic layers.

(5) Documenting the main achievements arising from improved quality of the components via device characterizations.

0. General introduction

Transport and manipulation of information is the driving force of the information technology. Traditionally, integrated circuits have been based on transport and control of charge in semiconductor devices[1]. Complementary Metal Organic Semiconductor (CMOS) is the basic electronic unit for electronic circuits and computer processors. Further shrinking of CMOS features will face fundamental physical limitations[2]. It is clear that in order to continue the long-term progress in the field of information technology, new unconventional ideas for information storage and processing are required to circumvent the fundamental limitations of traditional, silicon-based electronics.

The development of conceptually new materials following a "double beyond" trend, that is going "beyond CMOS" with "beyond silicon" materials, is one of the most challenging issues for the next generation of products for Information and Communication Technologies (ICT) applications. Future devices for information processing able to increase the public wealth and occupation require a further material downscaling, together with a considerable reduction of power consumption and associated costs. While there exist still some room for moving in this direction inside the "silicon field", it is widely accepted that the development of new materials and new paradigms is becoming increasingly imperative. For example, Intel experts consider possible to produce "only" three more generations of silicon processors before shifting to new materials[3]. The year 2017 is considered as a possible break point where at least a partial switching to new materials might become mandatory.

It is a matter of fact that electrons have a charge and a spin, which adds a new degree of freedom to conventional charge-based electronics (the spin moment of the charge carrier). Besides, electronic devices are traditionally based only on the charge, neglecting the spin. Examples of devices based on manipulation of electron charges are: field-effect transistors mainly used for information processing in tiny computer chips or operating in flat LCD computer displays; semiconductor diode lasers which read information stored in CDs and DVDs and reproduce sounds and pictures and others. Spin is a pure quantum concept and has no classical analogue. Electron spin carries a magnetic moment and so spin can be detected and controlled by magnetic

[1] Int. Technol. Roadmap on Semiconductors http://public.itrs.net.
[2] P. Rutten et al., Kellogg TechVenture 2001 Anthology.
[3] P. Otellini at Web 2.0 summit 2009, "Intel CEO bullish on 2010 prospects", at The Inquirer, 23 october 2009

fields. Spin-based devices have impacted on computer industry in 90's by introducing highly sensitive metal-based read heads for reading out information stored in hard drives, leading to a breakthrough in hard drive capacities towards hundreds of gigabytes. Such read heads are nowadays common in personal computers and notebooks.

In the current evolution into second-generation spintronic devices, there is a strong need for the development of novel, multifunctional materials and heterostructures with desirable magnetic and transport properties able to promote innovative properties. The ***Organic semiconductors*** (OSC) and various hybrid materials based on OSC which form the basis of the well established field of organic electronics are among the most interesting and promising candidates for such a development[4].

The advancement of OSC over the past decade has been spectacular. Numerous new materials based on small molecule semiconductors and polymeric semiconductors have been developed. Display products based on polymer LEDs have already become available to consumers and organic photovoltaic devices are challenging existing commercial applications.

Recently it came out that OSC are especially promising for spintronics applications, mainly due to the low spin-scattering amplitudes attainable in these materials. The spin orbit interaction, which provides usually the dominant spin scattering source, is very low – only about a few meV, well below the molecular vibration and rotational characteristic energies.

By injecting, transporting, manipulating and detecting spin-polarized currents, new spin-based multifunctional devices can be realized, including spin valves (magneto-resistive devices), spin-FETs (field effect transistors with spin polarized source and drain), spin-LEDs (spin polarized light-emitting diodes), and quantum bits for quantum computation and communication[4]. On the other hand, organic electronics offers the greatest advantage of low cost materials, cheap fabrication and processing methods, easy tuning of electronic and optical properties and others.

Similarly to elder organic electronics, one of the most serious challenges is the interface control, namely the way to insert and extract electrically driven information, interfacing fragile organic blocks with hard metallic or oxide electrodes. It has to be noted, on the other hand, that the hybrid nature of most organic based devices has also positive aspects, providing routes for large and fundamental modifications of the properties of the OSC, especially in the interface region. Effects of various nature, such as structural (molecular orientation at interfaces), electric (modification of the dielectric constant of OSC in the vicinity of a metal), optical (exciton quenching), introduce new properties and the device engineering has to carefully account for them.

[4] V. Dediu, L.E. Hueso, I. Bergenti, C. Taliani, Nat. Mat. 2009, **8**, 707.

The magnetic proximity effects at hybrid interfaces are expected to endow with an enormous potential for the modification of the spin transfer rates in hybrid materials with magnetic components. Understanding and tuning the properties of ***hybrid inorganic-organic interfaces*** is of fundamental importance for the optimization of device performance, stability, and reproducibility.

The presented thesis proposes an investigation which resides at the intersection of two important areas: ***spintronics***[5] and ***organic electronics*** [6]. The PhD thesis work, developed by the author for the period: 2007-2009, was concentrated on the engineering of materials and interfaces focused on the improvement of the know-how in the Spintronics Division at ISMN-CNR, Bologna, led by Dr. V. Dediu.

[5] S. A. Wolf et al., Science 2001, **294**, 1488.
[6] Friend et al., Nature 1999, **397**, 121.

1. Basic concepts

Spintronics

General principles

Spintronics relies on the different transport properties of the two spin populations (majority and minority spin) in a device. The information is stored, transported, manipulated, by acting on the spin of the carrier instead of its charge. Spin-electronics differs from the traditional parent since its development strategy is looking for new conception devices, not integration and scaling.

An electron current is named spin polarized when the electrons spin moments are completely or partially aligned. Usually in spintronic devices a very low current is enough to process the information, i.e. to generate, to vary or to read the current polarization, providing devices able to work at low power consumption and very low current leakage[7]. Nevertheless spintronic devices different from the early full metallic spin valves were put in the market only in 2006[8] and worked at mA currents also when the device size is reduced, causing a difficult scalability[9].

The first useful spin-devices were based on the anisotropic magneto-resistance (AMR) effect: the resistance changed with the direction of the applied magnetic field. In 1991 IBM introduced a magnetoresistive read-head based on AMR[10].

The first properly said spin-electronic device was the giant magnetoresistance based (GMR) read-head, introduced in the market by IBM in 1997 to replace the AMR sensor[11]. This device, based on the discoveries by Fert and co-workers and Grunberg and co-workers[12] and developed further by Parkin[13], consists in multilayer stacks of alternated ferromagnetic and diamagnetic metals.

---

[7] S. Bandhyopadhyay, B. Das, A. E. Miller, Nanotech. 1994, **5**, 113;
S. Das Sarma, American Scientist 2001, **89** 516;
M.E. Flatté, IEEE Trans. Electr. Devices 2007, **54** 907.
[8] H. Zabel, Superlattices and Microstructures, 2009, **46**, 541.
[9] G.W. Burr, B.N. Kurdi, J.C. Scott, C.H. Lam, K. Gopalakrishnan, R.S. Shenoy, IBM J. Res. & Dev. 2008, **52**, 449.
[10] A. Moser, K. Takano, D.T. Margulies, M. Albrecht, Y. Sonobe, Y. Ikeda, S. Sun and E.E. Fullerton, J. Phys. D 2002, **35** R157.
[11] A. Fert, Angewandte Chemie International Edition **47** (2008) 5956.
[12] M.N. Baibich, J. M. Broto, A. Fert, F. Nguyen Van Dau, F. Petroff, P. Etienne, G. Creuzet, A. Friederich, J. Chazelas, *Phys. Rev. Lett.* 1988, **61**, 2472; G. Binasch, P. Grünberg, F. Saurenbach, W. Zinn, *Phys. Rev. B* 1989, **39**, 4828.
[13] S.S.P. Parkin, N. More, K. P. Roche, *Phys. Rev. Lett.* 1990, **64**, 2304.

A most standard configuration for a spintronic device is based on two ferromagnetic electrodes separated by a spacer (an insulator, a semiconductor or a metal). Making an analogy to optics, the first electrode acts as a spin polarizer while the second electrodes is a spin analyzer: the band structure of the analyzer will accept the incoming electrons according to their spin orientation. The fundamental idea is tuning the relative orientation of the electrodes in order to observe a change in the resistance. When the electrodes are parallel polarized the majority spin electrons in the two electrodes have the same orientation and the band structure of the electrode acting as analyzer will accept the electrons from the first electrode, in the opposite case it will not do. So the basic requirement is that the electrons travel towards the analyzer through the spacer, or across it. In the first case the spacer between the electrodes is a transport medium: the spin device requires spin injection, transport, and detection (device called *spin valve:* SV). In the latter case the electrons reach the analyzer by tunneling through the barrier (device named *magnetic tunnel junction,* MTJ). Figure 1 sketches the magnetic field dependence of the resistance, it is called ***magnetoresistance*** (***MR***).

Figure 1: Sketch of the resistive switch in a spintronic device; the arrows at the top of the figure show the orientation of the magnetization of the electordes; H is the applied magnetic field and $H_{c1,2}$ are the coercive fields of the electrodes 1 and 2. Organge arrows shows from positive to negative fields, the blue ones from negative to positive field values.

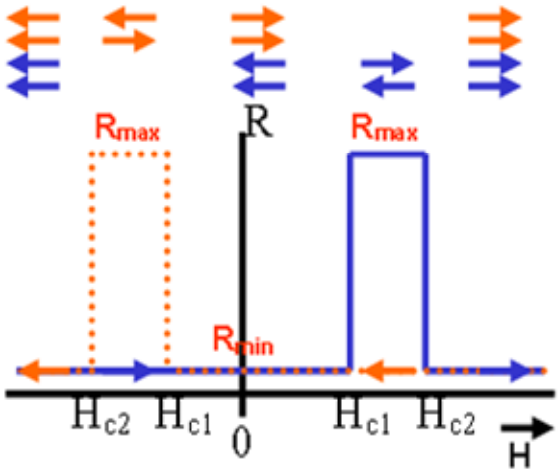

Several difficulties are encountered when the spin polarized current is wanted to be injected in a semiconductor[14]: this is known as *conductivity mismatch.* The behavior of ferromagnetic metals is traditionally comprised by the "two channel model" by Mott[15]. In a transition metal two Brillouin zones, say two spin sub-bands, exist for majority and minority spins respectively. Suppose the spin polarized current is injected from the ferromagnetic metal electrode into a non

[14] G. Schmidt, J. Phys. D: Appl. Phys. 2005, **38**, R107.
[15] N.F. Mott, Proc. Phys. Soc. A, 1935, **47**, 571; N.F. Mott, Proc. Roy. Soc. A, 1936, **156**, 368.

ferromagnetic semiconductor, whose resistance (Rsc) is five (let's say) orders of magnitude higher than the resistance of the metal[16]. Keeping the two spin bands picture, each band contributes with a 2Rsc. So the injection causes an imbalance in the population of the two spin bands in the semiconductor and a significant spin flip shall occur to restore the equilibrium.

In order to overcome this difficult one could introduce a spin selective tunnel barrier at the interface. Another solution is represented by the so-called ***half-metals***: a metal with only one spin band at the surface/interface, such as $La_{0.7}Sr_{0.3}MnO_3$ (LSMO) manganite, as probed by spin-polarized tunneling in LSMO/STO/LSMO MTJs[17] and by spin-resolved photoemission spectroscopy on LSMO surface[18]. With a fully polarized electrode there is injection only in the majority spin band and the intrinsic limitation to the spin injection disappears, the polarization transfer to the final electrode is now limited by the spin transport.

Finally we stress that this picture is strictly related to the concepts of bands and equilibrium. In a material in which the transport doesn't occur by bands but by hopping between localized states (as in OSCs) the conductivity mismatch argument seems inappropriate[19]. The injection process from a metal into an OSC is a tunneling event from the metal Fermi level in the first molecules orbitals, and the hopping process, responsible for the charge transport in the OSC, is a tunneling between the overlapping orbital wave functions of two different molecules. Since in the tunneling the spin does not flip, the conductivity mismatch picture should not be applied for organics.

Very recently (November 2009), spin injection, transport, manipulation by Hanle effect (spin precession around the applied Magnetic field), and detection was achieved in heavily doped (high conductivity) silicon, both n-type and p-type[20]. This experiment provides a strong basis for silicon based spintronics integrated with standard electronics. The authors combined together two strategies to circumvent the conductivity mismatch: they used heavily doped, low resistivity, silicon and at the same time inserted tunneling barriers.

[16] C. Kittel, "Introduction to Solid State Physics", WILEY; 8th edition (November 11, 2004).
[17] M. Bowen, A. Barthélémy, M. Bibes, E. Jacquet, J.P. Contour, A. Fert, D. Wortmann, S. Blügel, J. Phys.: Condens. Matter. 2005, **17**, L407.
[18] J. H. Park, E. Vescovo, H. J. Kim, C. Kwon, R. Ramesh, and T. Venkatesan, Nature 1998, **392**, 794.
[19] V. Dediu, L.E. Hueso, I. Bergenti, C. Taliani, Nat. Mat. 2009, **8**, 707.
[20] S.P. Dash, S. Sharma, R.S. Patel, M.P. de Jong, R. Jansen, Nature 2009, **462**, 491.

The role of the interfaces

Interfaces play a determinant role in the spin injection process and their relevance appeared clear since the first all metallic GMR devices[21]. The basic structure of these devices was a trilayer Fe/Cr/Fe, the current flowed in the plane of the film and the layers thickness was minor than the mean free path of the conduction electron. The huge MR signal was ascribed to the spin dependent scattering at the interfaces between the interlayer and the ferromagnetic layer, which is a consequence of the different density of states (DOS) in the spin up and spin down bands for ferromagnetic and non ferromagnetic metals (in the latter case the DOSs are the same), and to the roughness of the interface.

About the injection from a ferromagnetic metal in a non magnetic semiconductor, Fert an coworkers[22] show that the polarization of the injecting current reaches the wanted value when the interface resistance r_b^* is much higher than the sum of the resistances of the metal and of the semiconductor. But r_b^* has not to be too high, because it would prevent the injection; the highest limit for r_b^* is related to the spin diffusion length in the semiconductor, as obtained by Fert and co-workers[22]. A too transparent interfacial resistance enhances the proportion of spin flips on the electrode side of the interface, while a too cloudy one forbids the injection.

For OSCs, the state of the art is not as advanced as for inorganic ones , but the absence of band transport makes the picture possibly different.

The interfacial insulating layer not only increases r_b^*, but also makes the interface spin selective, depending on the electrode-barrier materials combination and structure, as pointed out by several studies on magnetic tunnel junction devices (MTJ) on both theoretical[23] and experimental sides[24]. In particular chemical bonding at the interface and symmetry arguments seem to be the two parameters determining the spin path in the tunneling event. The more clear experimental evidence come from MTJs LSMO/tb/Co (tb stands for tunnel barrier) featuring the inversion of the magnetoresistive response (MR) according to the material of the insulating space: it is experimentally found that when the tb material is amorphous Al_2O_3 MR was positive while

[21] A. Fert, P. Grunberg, A. Barthélémy, F. Petroff, W. Zim, J. Magn. Magn. Mater. 1995, **140**, 1.
[22] A. Fert, J. George, H. Jaffres, and R. Mattana, IEEE Trans. Electron Dev. 2007, **54**, 921.
[23] E.Y. Tsymbal, K.D .Belashchenko, J.P. Velev, Prog. Mater. Sci. 2007, **52**, 401; J.P. Velev, P.A. dowben, E.Y. Tsymbal, S.J. Jenkins, A.N. Caurso, Surf. Sci. Rep. 2008, **63**, 400.
[24] S.S. Parkin, MRS Bulletitn, 2006, **31**, 389.

when the tb is epitaxial $SrTiO_3$ the MR was negative[25]. Additional experimental work shows that the MR sign for LSMO/amorphous $SrTiO_3$/Co is positive[26]. Astonishing MR was detected in polycrystalline MgO based MTJ with CoFeB electrodes[27,28] (up to 604% at room temperature[28]). Furthermore the same structure at room temperature gives MR~220% with highly oriented MgO and ~70% with amorphous Al_2O_3[24]. Tunneling is not only a matter of insulting barrier, but also of symmetry, involving an active role in the spin selection, for the electronic states of the tunnel barrier.

The Co/Al_2O_3 system was studied by varying the Co electrode saturation moment by using a CoPt or CoV alloy, and by varying the insulating barrier composition by using AlN[29]. The tunneling through the insulating barrier appears to be closely connected with the strength of chemical bonds between the electrode atom and oxygen and the concept of ***chemically engineered interface*** comes out. Other experimental evidences of the relevance of the chemical bonds at the interface between the electrode and the barrier layer are observed in LSMO/Co junction with epitaxial $SrTiO_3$, with controlled termination layer, as tunnel barrier. The MR sign was negative for TiO_2 termination, both signs for SrO termination, and shifts towards positive value by increasing the oxygen vacancies concentration. Spin independent channel via O vacancies, which can induce non resonant scattering and reduce spin selectivity, is considered the best explanation for the observed behavior[30].

Provided a band structure, the above described concepts involved also a voltage dependence. By varying the applied bias the resonance between different states can be tuned, as experimentally observed with Ta_2O_5/Al_2O_3 tunnel barrier sandwiched between permalloy electrodes[31]

Organic Spintronics

State of art

Taking into account the difficulties for the injection of a spin polarized current into an inorganic semiconductor, OSCs suitability for spintronics started to be explored. OSCs are thought to be very promising for novel electronic applications, not as materials for high switching speed

[25] J.M. De Teresa, A. Barthélémy, A. Fert, J.P. contour, R. Lyonnet, F. Montaigne, P. Seneor, A. Vaurès, Phys. Rev. Lett. 1998, **82**, 4288.
[26] A. Thomas, J.S. Moodera, B. Satpati, Journ. Appl. Phys. 2005, 9, 10C908.
[27] S.S. Parkin, C. Kaiser, A. Panchula, P.M. Rice, B, Hughes, M. Samant, S.-H. Yang, Nat. Mat. 2004, **3**, 862.
[28] S. Ikeda, J. Hayakawa, Y. Ashizawa, Y.N. Lee, K. Miura, H. Hasegawa, M. Tsunoda, F. Matsukura, H. Ohno, Appl. Phys. Lett. 2008, **93**, 082508.
[29] See the section "influence of chemical bending on spin-polarized tunnelig" in ref.24.
[30] I.J. Vera Murin, F.M. Postma, J.C. Lodder, R. Jansen, Phys. Rev. B 2007, **76**, 064426.
[31] M. Sharma, S.X. Wang, J.H. Nickel, Phys. Rev. Lett. 1999, **82**, 616.

devices, but as low cost, flexible, light and large area coverage materials[32]. Two peculiar features characterize these materials: the low atomic number of their constituent (typically carbon, hydrogen, oxygen, nitrogen) and the π–conjugation of their molecular orbitals. Speaking about spin polarized carriers transport, the former means low spin-orbit scattering, the latter low hyperfine interaction scattering[33]. So OSCs turn out to be promising candidates as charge transport media in spintronics devices.

As a matter of fact Dediu and co-workers[34] showed, for the first time, in 2002, the successful employment of an OSC (sexithiophene, T6) as spin transport material which showed a spin diffusion length of at least 70 nm and a spin life time around 10^{-6}s: the field of organic spintronics saw the light. In 2004, Xiong and coauthors demonstrated the first organic spin valve with a vertical structure[35]. They sandwiched a Tris(8-hydroxyquinoline)-aluminum(III) (Alq_3) layer between a bottom LSMO electrode and a top Co electrode reporting a giant MR (GMR) of 40% at 11 K and of about 4% at 80 K. Unexpectedly the spin valve effect was inverse, that is the lowest resistance corresponded to antiparallel orientation of the electrodes. The effect was constrained in a ± 1 V voltage interval and vanished above about 240-250 K. Starting from this work, the vertical geometry has acquired a preeminent role in organic spintronics, mainly because of its technological simplicity compared to planar devices, which require a substantial involvement of lithography. Most studied OSCs are T6[34], Alq_3[36], NPB[37], P3HT[38]. Several groups have confirmed the so-called inverse spin valve effect not only in LSMO/Alq_3/Co devices: also α-NPD (*N*,*N*-bis 1-naphtalenyl-*N*,*N*-bis phenylbenzidiane) and CVB (4,4'-(Bis(9-ethyl-3-carbazovinylene)-1,1'-biphenyl) were demonstrated to behave very similarly to Alq3 with LSMO and Co set of magnetic electrodes: inverse spin valve effect (around 10% at low temperatures) and fast decrease of the magnetoresistance with increasing temperature, vanishing between 210 and 240 K[39]. Since these discoveries, organic spintronics was object of intense efforts.

Ferromagnetic oxide $La_{0,7}Sr_{0,3}MnO_3$ (LSMO) is the most used electrode in organic spintronics due to its successful applications. Devices with LSMO electrode show spin valve

[32] Forrest S., Nature 2004, **428**,911.
[33] V. Dediu, L.E. Hueso, I. Bergenti, C. Taliani, Nat. Mat. 2009, **8**, 707.
[34] V. Dediu, M. Murgia, F. C. Matacotta, C. Taliani, S. Barbanera, Sol. St. Comm. 2002, **122**,181.
[35] Z.H. Xiong, D. Wu, Z.V. Vardeny, J. Shi, Nature 2004, **427**, 821.
[36] E. Arisi, I. Bergenti, V. Dediu, M.A. Loi, M. Muccini, M. Murgia, G. Ruani, C. Taliani, R. Zamboni, J. Appl. Phys. 2003, **93**, 7682; Z.H. Xiong, D. Wu, Z.V. Vardeny, J. Shi, Nature 2004, **427**, 821; F.J. Wang, Z.H. Xiong, D. Wu, J. Shi, Z.V. Vardeny Synth. Met, 2005, **155**, 172;
[37] E. Arisi *et al. Ibid.*
[38] S. Majumdar, R. Laiho, P. Laukkanen, I.J. Väyrynen, Appl. Phys. Lett. 2006, **89**,122114.
[39] F. J. Wang, C.G. Yang, Z.V. Vardeny, X. G. Li , Phys. Rev. B 2007, **75**, 245324.

behavior up to room temperature[40]. An important point to mention is that devices with manganite electrodes operate almost up to the Curie transition temperature of the LSMO. On the other hand, devices with only transition metals electrodes (whose Curie temperature is far above R.T.) stop working well before their characteristic temperature: interfaces play a definitely crucial role[41].

In addition, only recently magnetoresistive behavior up to R.T. in spin valve devices with 3d metals electrodes[42] was achieved. The detected MR was positive in both injection and tunneling devices, where the organic layer is thought to act as a tunneling layer instead of transport media[43]. Positive MR of about 15% at liquid helium temperature and a few per cent at room one were achieved.

Hybrid MTJ based on Alq_3/MgO which features spin diffusion length much higher than 10 nm has been fabricated[44] and MR around 12% was obtained at room temperature. Furthermore the inversion of the sign of the MR was detected with the voltage, positive for $V < 250$ mV and negative for $V > 250$ mV. It may be related to the exchange splitting of the energy of the tunneling electrode, but when crystalline MgO is substituted by amorphous aluminum oxide the inversion does not happen. Possibly the inversion is due to the different states which are in resonance at different applied voltages, and the resonance is mediated by the interfacial states of ordered MgO, as observed in fully inorganic MTJs.

A very recent work on current injection in amorphous rubrene (Rb) by tunneling gives insight into the role of the interface[45]. Devices with rubrene sandwiched between a bottom Co electrode and a Fe top electrode were produced for transport and MR measurements, while for tunneling spectroscopy Rb was sandwiched between Al electrodes. Each device had a twin in which the bottom interface was engineered by the deposition of a seed layer of alumina (aluminum deposition and plasma oxidation) on top of which the amorphous rubrene (Rb) was deposited at room temperature. The whole deposition was performed by all *in situ* thermal evaporation. The Rb films thickness ranged from 10 to 25 nm. They observed a very different molecular ordering for the two different surfaces (metals or oxide). Combining thickness measurements with inelastic tunneling spectroscopy (which gives a sort of vibrational spectroscopy on the levels involved in the transport) and transport measurements, they conclude that Rb molecules dispose vertically on

[40] V. Dediu, L.E. Hueso, I. Bergenti, A. Riminucci, F. Borgatti, **P. Graziosi**, C. Newby, F. Casoli, M.P. de Jong, C. Taliani, Y. Zhan, Phys. Rev. B 2008, **78**, 115203.
[41] Dediu, L.E. Hueso, I. Bergenti, C. Taliani, Nat. Mat. 2009, **8**, 707.
[42] Y.Liu, T. Lee, H. E. Katz and D. H. Reich, J. Appl. Phys. 2009, **105**, 07C708; Y.Liu, S. M. Watson, T. Lee, J. M. Gorham, H. E. Katz, J. A. Borchers, H.D.Fairbrother and D. H. Reich, Phys. Rev. B 2009, **79**, 075312.
[43] T.S. Santos, J.S. Lee, P. Migdal, I.C. Lekshmi, B. Satpati, J.S. Moodera, Phys. Rev. Lett. 2007, **98**, 016601; J.H. Shim, K.V. Raman, Y.J. Park, T.S. Santos, G.X. Miao, B. Satpati, J.S. Moodera Phys. Rev. Lett. 2008, **100,** 226603.
[44] G. Szulczewski, H. Tokuc, K. Oguz, J.M.D. coey, Appl. Phys. Lett. 2009, **95**, 202506.
[45] K.V. Raman, S.M. Watson, J.H. Shim, J.A. Borchers, J. Chang, J.S. Moodera, Phys. Rev. B 2009, **80**, 195212.

the oxide surface with a higher order than the flat lying molecules observed for the direct Rb deposition on the metal (Al or Co). When Rb is deposited on the oxide surface it features best order and injection and transport properties, although it is not clear if the best injection is due to the Al_2O_3 presence or to the different molecular orientation. The MR was detected at 100 mV, it persisted up to room temperature only for the Rb/Al_2O_3 situation and for Rb thicknesses up to 25 nm. The experiment above summerized[45] points out the definite relevance of the interface and the extreme difference of OSC in respect to metal or oxide surfaces.

Alq_3 is a popular OSC from the early stages of xerographic and optoelectronics applications[46]. This material might look somehow as a strange choice for transport-oriented applications, as Alq_3 has very low mobility values and a permanent electric dipole[47]. These two factors are in principle able to compromise spin transport but in spite of the expected problems with Alq_3, strong spin-mediated effects have been constantly reported by different groups. The wide use of Alq_3 is probably due to the good quality thin films which can be grown on various ferromagnetic substrates by standard UHV evaporation.

The following, and the rest of the thesis, will focus only on spin valve (injection) devices, where the spin information is transported by the OSC electronic levels. This choice helps to elucidate most efficiently the interface role in organic spintronic devices.

Problems

Spin devices based on organic materials offer several promising features[48], but some relevant aspects are still open and unclear. First of all, focusing on the application potential of organic spintronics devices, the most important quantitative parameters, the strength of the spin valve effect, the value of MR, must be defined. The first report on GMR in an organic spin valve is that of -40 % by Xiong and co-workers[35] and in 2006 a GMR of 80% was reported for the LSMO/RR-P3HT(100nm)/Co system at 5 K [38]. Looking for a general definition of MR, we define it as the percent difference in resistance between the parallel and antiparallel states, so that the difference is maximized. By this definition, the MR is -30% in the former case ((25-17,5) KΩ / 25 KΩ looking at figure 2a of the paper[35]) and to 60% in the latter. These values are smaller (in absolute terms) than the ones reported above because our definition eliminates MR effects other than those associated with the hysteresis of the electrodes magnetization. To reach of an unambiguous definition for the strength of MR is of extreme practical relevance.

[46] C.W. Tang, S.A. van Slyke, Appl. Phys. Lett. 1987, **51**, 913-915.
[47] A. Curioni, M. Boero, W. Androni, Chem. Phys. Lett. 1993, **70**, 1473; A. N. Caruso, D. L. Schulz, P. A. Dowben, Chem.Phys. Lett. 2005, **413**, 321.
[48] V. Dediu *et al.*, Nat. Mat. 2009, cited.

The device operation temperature dependence is an experimental topic which requires accurate studies. It was explained in the previous section that the maximum temperature for a hybrid spin valve to work does not depend on the Curie temperature of the electrodes: what is the connection between the magnetic properties of the electrodes and the device, what determines the device magnetic properties, is a crucial matter not yet fully understood. Furthermore the above described rapid decrease of the MR with temperature, which fits very well with the loss of the surface magnetization of the LSMO with increasing temperature, indicates that it is the surface electrode magnetization to drive the temperature behavior of the spin device. But it is still a fact that Co, Fe or permalloy based devices do not work up to temperature so much high as their T_C should let; the reason evokes the electronic and spin structure of the interface, nevertheless it has not been fully explained yet.

A second group of open questions concerns the spin injection and transport in the organic material. A barrier exists to the carrier injection to be overcome[49]. Spin valves operate at voltages two orders of magnitude smaller than this barrier. Moreover the spintronic behavior of the organic spin valves disappears increasing the bias at values similar to the voltage operation in OLEDs and OFETs: the I-V characteristics persists, but the spin transport is suppressed…or, better, not detectable. Also the decoherence mechanisms in organic are being subject of intense research. In a naïve approach it is clear that spin-orbit coupling in OSC is very small, but a detailed and predictive description has been lacking. Currently, alternative mechanisms for spin decoherence are being considering. Recently Bobbert et al.[50] have advanced the idea that the precession of the carriers spins in the random hyperfine fields of hydrogen nuclei (around 5 mT) represents the dominant source for spin scattering in OSC. The authors have derived the spin diffusion length l_S in a typical OSC and they obtain a very weak dependence of l_S on temperature, in good agreement with recent experimental data[51]. Surprisingly, it was also shown that the spin scattering strength is much less sensitive to disorder than the carrier mobility, a result that could shed light on the apparent discrepancy between low mobility and long spin diffusion lengths in OSC. A clear comprehension of these aspects should have a huge positive impact in the development of the organic spintronics.

The sign of the magnetoresistance is another relevant aspect. A clear and reproducible experimental result is that devices with LSMO and Co electrodes show a negative MR with several OSCs and the substitution of the LSMO electrode by Fe has removed the inversion of the

[49] V.I. Arkhipov, E.V. Emelianova, H.Y.Tak, H. Bassler, J. Appl. Phys. 1998, **84**, 848.
[50] P.A. Bobbert, W. Wagemans, F.W.A. van Oost, B. Koopmans, M. Wohlgenannt, Phys. Rev. Lett. 2009, **102**, 156604.
[51] V. Dediu *et al.*, Phys. Rev. B 2008, cited.

spin valve effect[52]. Moreover tunneling experiment show that the Co/Alq_3 is positively polarized: the inversion is strongly caused by the manganite properties. A model attempting to explain it has been developed[53]. It introduces a very narrow hopping channel in the OSC, connecting at some given voltage the spin-up bands of one of the electrodes with the spin-down bands of the opposite one. While in principle feasible, this model can be applied for the n-type carriers only and works mainly at voltages about 1 V or higher, that is values at which spintronics effects in LSMO/Alq_3/Co devices generally vanish, while highly efficient performances are constrained in a narrower interval of about 100 - 200 mV. This situation clearly indicates the limits of the overall comprehension of the main laws governing both the spin injection and transport in organic spintronics.

Experiments on Alq_3 underline that when the energy landscape is so that electrons are injected in Alq_3 the devices feature MR response, while when Alq_3 is used as hole transporter, the magnetoresistance is not detected[54]. The definition of the polarization of the current should take account for the velocity of the spin carriers, since transport involves not only their density of states, but also their mobility. If the electrons were much faster than the holes the absence of MR in hole-transporter Alq_3 devices would be explained.

Finally, the structural and electro-magnetic quality of the interfaces does matter. The sharpness of the surfaces (smoothness and absence of intermixing, penetration, reactions...) is a problem in vertical devices, while the definition of lithography protocols able to preserve the spin injection ability from the lithographed sides is useful in planar technology.

Thin film growth

In this section the main concepts about thin film growth and the morphological characterization will be reviewed.

Thin films growth - the basics

Thin films are bidimensional layers obtained by depositing the film material on surfaces of different substrates. Nucleation and growth of thin films include processes described by different

[52] Y.Liu, T. Lee, H. E. Katz and D. H. Reich, J. Appl. Phys. 2009, **105**, 07C708.
[53] V. Dediu *et al.*, Phys. Rev. B 2008, cited
[54] J.S. Jiang, J.E. Pearson, S.D. Bader, Phys. Rev. B 2008, **77**, 035303.

time and length scales spanning over many orders of magnitude. Some of the phenomena that occur are inherently stochastic in nature, and we must consider fluctuations (intrinsically not deterministic in nature) considering the film growth, possibly including only the necessary ones.

In Figure 2 [55] a picture of the main possible interaction is presented. Atoms or molecules are deposited onto the substrate surface with a deposition flux *F*; sometimes it is termed deposition rate *R*, both measured typically in monolayers per second. Once atoms are on the surface as adatoms, they can diffuse with a diffusion constant *D*. Adatoms can meet other adatoms to form a dimer, or attach to existing islands. Once adatoms are attached to an island, they can detach from or diffuse along the island edge. Deposition of adatoms on top of islands and the corresponding processes have to be considered as well, including the interlayer diffusion, i.e. the fact that an atom can migrate from the surface inside the island, intermixing can also take place between the ad-atom and the substrate, if there is a certain affinity; at high temperatures some adatoms can re-evaporate. Moreover a dimer can be stable or it can dissociate. After a certain number of adatoms or admolecules meet, the energy of the nucleus is lower than the sum of the separate admolecules energy: the nucleus is stable in respect to the dissociation. The minimum number of atoms or molecules needed to form a stable nucleus is named *critical size* and labeled as *i**.

Figure 2: Surface processes.

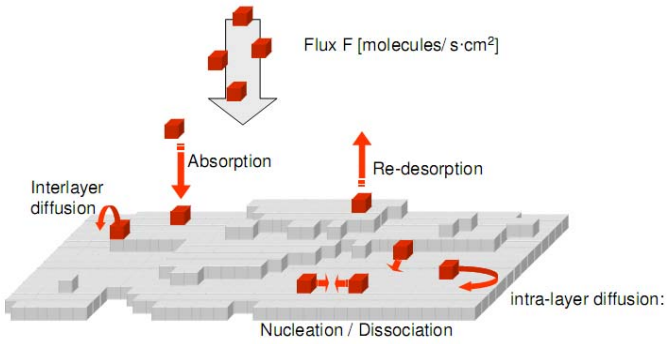

Each process is characterized by an activation energy and a characteristic time. The final effective pathway depends on activation barriers for the relevant atomistic processes, rather than just on the interaction energies. The slowest process will limit, and dominate, the whole growth[56].

For the work described in the present thesis, it is important to underline the basic peculiar features of organic thin film deposition in comparison to the inorganic counterpart[55]. Organic semiconductors consists in molecules, which are composed by several atoms. So they have got

[55] S. Kowarik, A. Gerlach, F. Schreiber, J. Phys.: Condens. Matter, 2008, **20**, 184005.
[56] C. Ratsch and A. J. Venables, J. Vac. Sci. Technol. A 2003, **21**, S96.

vibrational degrees of freedom which can impact the ad-molecules thermalization, since they could absorb translational kinetic energy and the molecule-substrate interaction. Molecules have also conformational degrees of freedom letting them to bend in order to accommodate possible stresses. The orientational degrees of freedom lead to a preferential orientation. Due to their orientational flexibility the molecules can give rise to tilt domains. All these degrees of freedom do not exist in inorganic thin films, and often are not included in traditional thin film growth theories.

The dispersive van der Waals type interaction between molecules are quite weak if compared with bonds between inorganic atoms (metals, oxides, inorganic semiconductor). Nevertheless, summing over all the atoms in a molecule, one can have binding energies of the order of eV along preferential directions (because of the orientational and conformational degrees of freedom) like in the case of two pentacene molecules facing each other[57]. Moreover one must consider that molecule size is larger even than a whole unit cell of inorganic elements and compounds, so the interaction potential is spread out over a relatively large distances and the corrugation of the substrate at the atomic scale are mediated and quite less relevant for the molecules.

Finally we note that if it is quite difficult to expect an interdiffusion between molecules and the inorganic substrate, intermixing between incoming molecules and already bonded ones is very possible due to chemical similarity and to the large amount of degrees of freedom described.

As a consequence the ad-molecules impinging the inorganic substrate feel an energy landscape, and a number of possible events, very different from what experienced by the following molecules landing on other, identical, molecules. So what happens in the sub-monolayer regime or in a multilayer regime where the substrate effect still persists, is completely different from what occurs in regimes where the substrate effect is lost. This explains the rapid roughening observed in organic semiconductor thin films[58].

Once stable nuclei are formed, they can grow in bidimensional fashion or in a three dimensional one, according to thermodynamics resulting from a competition between the old surface energy of the substrate (γ_s) and the new surface energy given by the sum of the contributions from the film surface (γ_f) and the film-substrate interface (γ_i).

In the former mode, named layer-by-layer, or Frank-van der Merwe (FM), nuclei are usually one atom or one molecule high and extend in a bidimensional fashion. FM mode occurs when the interface energy between the film and the substrate plus the film surface energy is lower than the surface energy of the substrate. There is an energy gain in forming the interface film/substrate. An

[57] S. Pratontep, F. Nüesch, L. Zuppiroli, M. Brinkmann, Phys. Rev. B, 2005, **72**, 085211.
[58] S. Kowarik, A. Gerlach, F. Schreiber, J. Phys.: Condens. Matter, 2008, **20**, 184005.

atom, or molecule, arriving on top of a nucleus will not bond to the top of the nucleus but to the edge, creating a bond also with the substrate. Nuclei grow and, when meet, coalesce; the nuclei meeting happens by growth or by migration. The following layer starts to grow when the bottom one is completed.

On the contrary, when the energetic interaction between the film atoms themselves is favorite in respect to the bonding with the substrate, the nucleus develops vertically in a three-dimensional fashion, named Volmer-Weber (VW) growth mode. Atoms or molecules arriving on the substrate arrange in islands and let the substrate surface not covered until the coalescence (due to lateral growth o to migration) of the islands. In the VW growth, each single island could grow in a layered fashion, but each island grows vertically before the complete coverage of the substrate: a simultaneous multilayer growth[59].

Finally, a transition between the two former modes often happens: a fluctuation breaks the strained 2D growth and the process switches to VW mode: Stranski-Krastanov (SK) transition or SK growth mode. There are several reasons for the SK mode to occur, such as a change in lattice parameter or symmetry or molecular orientation, or the release of elastic stress by creating line defects, as it happens in epitaxy. The thickness for the SK to occur depends also on the deposition conditions such as the substrate temperature[60].

When stable nuclei meet each other, as a consequence of nuclei diffusion or lateral growth, they coalesce. This process leads to a decreased islands density and shifts the nuclei size distribution peak towards higher values: this is referred as film coarsening, the driving force is the reduction of the step edge total free energy of the islands. Together with the coarsening due to stable islands migration (known as Smoluchowski ripening) it could happen that large islands grow at the expense of small ones. People refer to the latter ageing effect as Ostwald ripening (initially observed for solutions). It requires adatoms detachment from a small islands edge and attachment to the edge of a bigger islands. It depends on the atoms number on the island edge and on their mobility and is led by thermodynamics. Its reason lies in the fact that smaller grains have a higher surface/volume ratio, and so they have less energy per atom than bigger islands, and so they are thermodynamically less stable.

[59] M.G. Barthès, A. Rolland, Thin Solid Films 1981, **76**, 45; A. Rolland, M.G. Barthès, C. Argile, Thin solid Films 1981, **82**, 201.
[60] See, as example, V. Dediu, A. Kursumovic, O. Greco, F. Biscarini, C. Matacotta, Phys. Rev. B 1996, **54**, 1564, for the temperature dependence of the onset of the SK transition in $GdBa_2Cu_3O_{7-\delta}$ thin films.

Figure 3: Conventional growth modes.

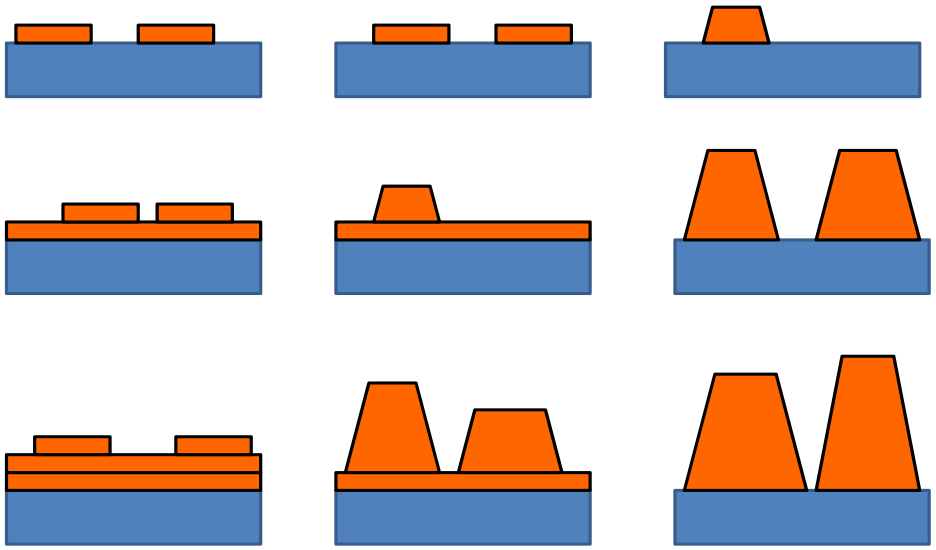

When an atom, or a group of atom, or a molecule, lands over a nucleus, it goes towards two possibilities: stay on top of that nucleus or jump down. Previously we addressed this topic by means of thermodynamic arguments involving interfacial and surface energies. We now consider that when this atom comes to the edge of a terrace, a lower density of unsaturated bonds prevents it going over the edge[61]. The atom which wants to jump has to go through a very uncomfortable state of very low coordination, poor binding, higher energy. So a barrier exists to the diffusion from a terrace to another, which is known as Ehrlich-Schwoebel barrier E_{ES}. It contributes in determining the growth mode; e.g. if E_{ES} high enough the atoms landed on top of an island will be confined there and the nucleus develop is straightforward three-dimensional. This regards the second layer nucleation.

Each film growth technique introduces additional kinetic processes and energy contributions, according to the way it operates. Thus different techniques add different process to the simple models previously described, which are derived from a simple condensation from a vapor phase.

Now a few words will be spent for epitaxy: a peculiar type of thin film growth which aims to grow a film which mimics the crystal structure of the substrate: epi-taxy comes from the Greek epi (above) taxis (structure, order). Epitaxy concerns about the oriented growth of one crystal (the film) to another one (the substrate or a bottom film). So a single crystalline substrate is required and the crystal structure of materials we want to grow on top has to be a lattice parameter similar to that of the substrate. The key parameter is the lattice mismatch ε, i.e. the relative difference in

[61] M. Lagally and Z. Zhang, Nature, 2002, **417**,907.

the unit cell parameters in the plane. It is defined as $\varepsilon = \frac{a_s - a_f}{a_s}$, where a_f is the lattice parameter of the film and a_s that of the substrate. ε changes according to the crystallographic orientation, i.e. it can be vary along two direction in the substrate surface. If $\varepsilon > 0$ the film will feel a tensile strain in the plane directions and a compression in the vertical one while the opposite for $\varepsilon < 0$.

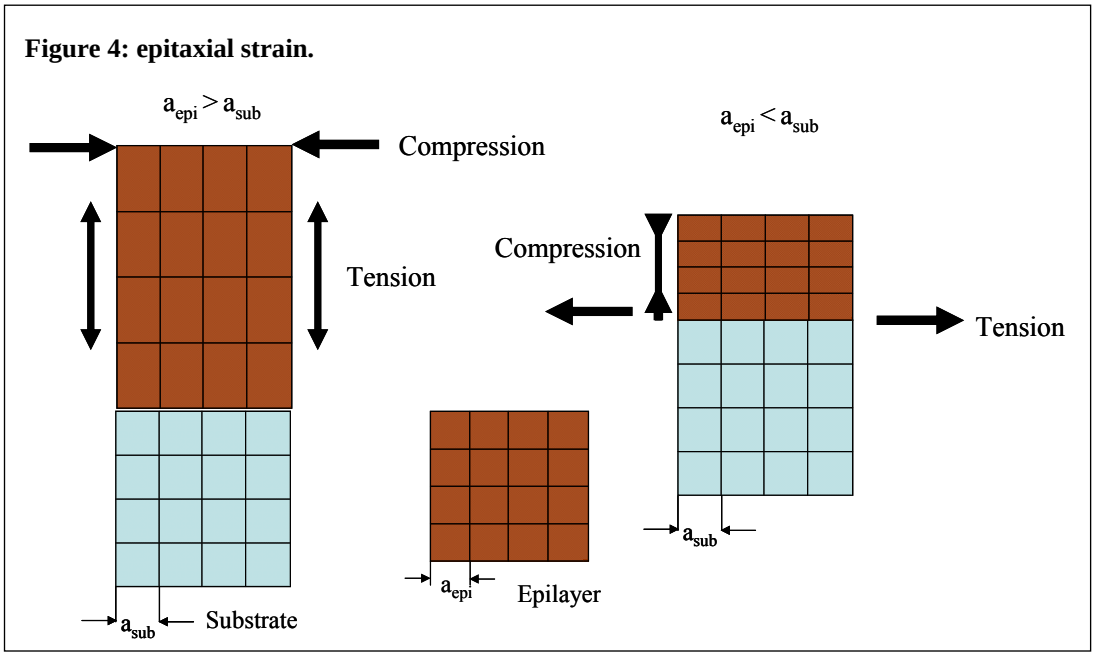

Figure 4 sketches a section of the epitaxial growth scheme to elucidate these concepts. Since the crystal structure of a material represents the minimum energy configuration, the epitaxy process induces an elastic energy accumulation in the film structure. This energy is additive, so for a certain (critical) thickness, this energy is released and the film material recovers its bulk structure. After this happens, the film continues to grow in a crystalline fashion, but the single crystalline quality is missed. The crystallites can keep their out-of-plane orientation, so there is still an orientation in the film. Differently the grain are individually crystalline, but with different orientations and the film is polycrystalline and gives the diffraction pattern of powder. It is remarkable that the epitaxial stress behavior depicted Figure 4 is related to the unit cell volume conservation, but it remains true also for systems, such as manganite, where the unit cell volume is not conserved[62].

The epitaxy is conceptually related to the single crystallinity of the film and is a macroscopic characteristic detectable by x-ray diffraction, and it is not related to the growth mode: both FM and VW growth mode can lead to epitaxial films, once the epitaxy requirements is satisfied. As a matter of fact when surface diffusion rates are significant, film thickening proceeds through local

[62] A.M. Haghiri-Gosnet, J.P. Renard, J. of Phys. D: Appl. Phys.2003, **36** R127.

epitaxy on individual grains[63]. Recrystallization through grain boundary (GB) migration, can occur both during and after islands coalescence. The results is a new single-crystal island as the system attempts to minimize the overall surface and interface energy. Thus, coarsening during coalescence is the first and most active phenomenon leading to selection of preferred orientation of epitaxial film.

Figure 5: grain coarsening during epitaxial thin film growth.

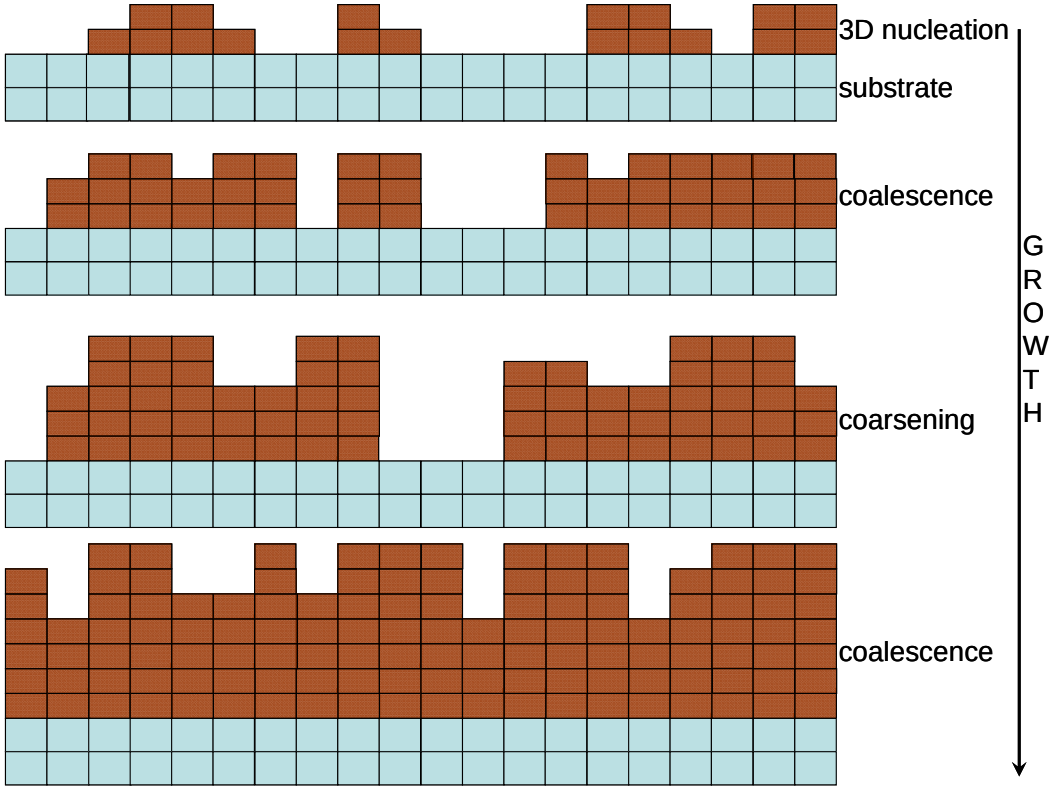

Figure 6: ES picture in epitaxial growth.

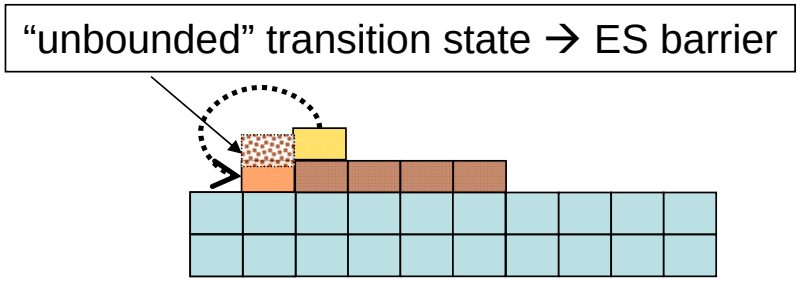

Ehrlich Schwoebel barrier E_{ES} acts also in epitaxial growth of course (Figure 6). Due to the ordered arrangement of the atoms, when an atom, or a unit cell in e.g. oxides epitaxy, is composed

[63] I. Petrov, P. B. Barna, L. hultman, J. E. Green, J. Vac. Sci. Tech. A 2003, **21**, S117.

on top of an island, binding symmetry could create a very high E_{ES} almost preventing the atoms interlayer diffusion.

Figure 7: sketch of epitaxial growth with prevented interlayer diffusion.

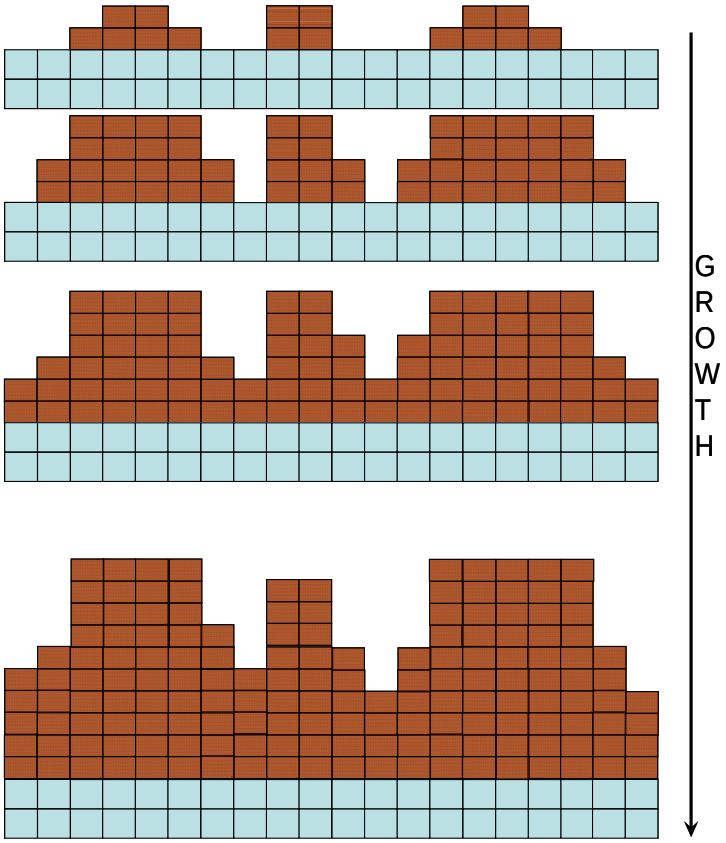

The consequence in the film growth is the persistence of the first layer pattern [64], since the step spacing on the sides of the islands decreases with increasing coverage (mound steepen) and the merging of the islands is suppressed by the fact that the following layer nucleation occurs only on the top of each mound. Figure 7 sketches the epitaxial patterning in this case; note that mounds size persists.

Morphology - stable islands density

The models typically used in nucleation theory are either completely stochastic or completely deterministic; some models exist which give a stochastic character to the deterministic picture of the rate equation framework, for instance by placing in random positions step edges and islands boundaries (level set method). Each stochastic modeling (Monte-Carlo, Car-Parrinello, Molecular Dynamics) focuses on a specific system, while rate equations try to find a general frame where one recognizes the experimental results.

[64] J. Krug, Physica A, 2002, **313**, 47.

In particular the island density appears as a relevant parameter having the dependence: $n = AF^p e^{E_N/kT}$, where p is related to i^* and E_N is the nucleation energy, F is the flux of incoming atoms or molecules and A is a constant which takes account of the capture numbers, the unit cell volume, the adsorption sites and the frequency attempt to the diffusion and desorption, while the activation barriers enter in the nucleation energy terms, according to the growth regime, as collected in the table below, elaborated from Venables *et al.*[65]. E_N stands for the global nucleation energy above defined, E_{i^*} is the binding energy of an island made by i^* molecules, which is a stable island since i^* represents the critical number of molecules, E_a is the energy barrier for the re-evaporation, E_d is the diffusion energy barrier.

Table 1

Regime	3D nuclei (VW and SK)	2D nuclei (FM and SK)
Extreme incomplete	$E_N = \left[E_{i^*} + (i^*+1)E_a - E_d\right]/i^*$	$E_N = \left[E_{i^*} + (i^*+1)E_a - E_d\right]/i^*$
	$p = 2i^*/3$	$p = i^*$
Initially incomplete	$E_N = (E_{i^*} + i^* E_a)/i^*$	$E_N = (E_i + i^* E_a)/i^*$
	$p = 2i^*/5$	$p = i^*/2$
Complete	$E_N = (E_{i^*} + i^* E_d)/i^*$	$E_N = (E_{i^*} + i^* E_d)/i^*$
	$p = i^*/(i^* + 2.5)$	$p = i^*/(i^* + 2)$

Extreme incomplete regime means that desorption is so important that the diffusion length $\chi_s = \sqrt{D\tau_a}$ (where D is the diffusion coefficient and τ_a is the residence time) is so short that islands grow by capturing only atoms landing directly on the islands because taking the diffusion. Since $D_s = a^2 \nu e^{(-E_d/kT)}$ (a is the interatom spacing and ν the jump frequency attempt) and τ_a varies as $e^{E_a/kT}$ the resulting E_N depends on all the energy barriers. Note the positive sign for the barrier to desorption E_a, which obstacles the growth, and the negative sign for the diffusion barrier E_d: a smaller barrier means an easier diffusion helping the growth of existing islands and making the nucleation of new islands slower.

Complete condensation takes place when the desorption time is negligible and the limiting process to clusters growth is the adatom diffusion and reaching an existing islands before to nucleate in a new stable cluster. Note the different sign of E_d, which is now the limiting process, and the absence of E_a, since desorption is negligible.

Often, the condensation starts out incomplete, and becomes complete by the end of deposition: this middle regime is called initially incomplete. The condensation is still incomplete,

[65] J. A. Venables, G. D. Spiller, M. Hanbücken, Rep. Progr. Phys. 1984, **47**, 399.

but islands capture atoms by surface diffusion. Thus the limiting process is now the desorption and the relevant barrier is E_a.

Morphology - scaling concepts

Now it is necessary to note that the growth modes described above are governed by thermodynamic argument, i.e. in equilibrium or quasi-equilibrium condition, and are referred to the early stages of growth. Alternative concepts exist, providing parameters able to give a quantitative characterization of the morphology, transcending the microscopic atomistic events, having connections with the temporal evolution of the surface, and capable to be applied for films far from the early stages of growth where the picture of "islands on substrate" is missed since the substrate is fully covered and bottom far from the surface.

Looking at the surface as statistical objects one key parameter is the root mean square (rms) width of the interface, which contain information about the rms oscillations around the mean value. It is defined as $\sigma = \frac{1}{N}\sqrt{\sum_i (z_i - \bar{z})^2}$, where z_i is the height of the i point, $\bar{z}$ is the mean height and N is the total number of point; σ is often named rms roughness and concerns with the vertical roughness. Another key is the height-height correlation function (HHCF). It describes the lateral roughness since it is calculated as square of the difference between the height of a point and that of the other. HHCF is a function (g) in the variable of the distance between the point and the other we use to compute the difference (t_x,t_y), for x and y respectively: $g_{(t_x,t_y)} = \frac{1}{N}\iint \left(z_{(x,y)} - z_{(x+t_x,y+t_y)}\right)^2 dxdy$. From scanning probe data (STM, SEM, AFM...) usually the integral is a sum on the fast scan direction x only (in order to limit the drift of the piezo-scanner), and then mediated for all the lines[66]. What is important is the dependence of this two rughnesses on deposition time and temperature.

A lot of literature exists on the analysis of the information which can be extracted from an analysis of self-affine surface, that is a surface whose properties do not change upon a rescaling of the x-y (in plane) dimensions (it is a sort of fractal self-similarity in 2D)[67]. Anyway, Evans and co-workers outlined[68] one has to be careful: the HHCF shape is an optimum criterion to discern between self-affine surface and mounds surface. While the former is a pure stochastic object, the

[66] Further computational details in the user manual of the software: www.gwyddion.net/documentation.
[67] J.D. Kiely and D.A. Bonnel, J. Vac. Sci. Technol. B 1997, **15**,1483.
[68] J. W. Evans, P. A. Thiel, M. C. Bartelt, Surf. Sci. Rep. 2006, **61**, 1 ; see in particular the paragraph 3.4, p. 15, and fig.8.

second is not, but it is closer to the real films growth not purely led by thermodynamics, e.g. multilayer stacks of bidimensional islands where the mass transport towards bottom layers is inhibited. From HHCF one obtains firstly the correlation length, i.e. the distance at which the heights of two points stop to be correlated, and it is the first maximum of the HHCF. The correlation length ξ is the mean lateral size of the mounds. Then for very short distance between two points ($t_x << \xi$) the HHCF shows a power law trend. The time and temperature dependence of these data often show the following power law behavior:

$$\sigma \approx t^{\beta}, \qquad L > \xi$$
$$\sigma \approx L^{\alpha}, \qquad L << \xi$$
$$g_{(t_x)} \approx {t_x}^{2\alpha}, \quad t_x << \xi$$
$$\xi \approx t^{z}$$

t is the deposition time, L is the size of the area used to compute σ. A length scale (correlation length ξ) exists beyond which the rms roughness doesn't change, while for smaller length scales σ changes with the image size used for calculations. The rms roughness scales with the deposition time, or with the thickness. The power law exponent is the growth exponent β, which describes how the interface width varies with the deposition time (at fix rate). From the HHCF, in the short translation length region, one obtain the roughness exponent α which is directly linked to the lateral roughness. Krim and Palasantzas[69] illustrate as a surface can have the same rms roughness but very different vertical features and roughness exponents α: a more ragged profile means a lower roughness exponent; the upper limit is α=1 and corresponds to a surface with very large scale fluctuations without self-affine character. For pure real self-affine surfaces α<1. $z=\beta/\alpha$ is the dynamic exponent.

The models just lead us into the question about the usefulness of these exponents. A standard approach wants us to compare the experimentally obtained values with those predicted by models[69]. Since each model focuses on a peculiar process, one should learn what are the dominant, or limiting, factors in the film evolution. It is noticeable that this happens by an analysis of the evolution of surface features, without considering the sub-monolayer regimes. The simplest model which is the case to describe is the random deposition model (RD), or "hit and stick": adatoms attach randomly on the surface, diffusion neither desorption are considered. Following this model $\sigma = \sqrt{dD}$, where d is the thickness of a single atomic layer and D is the thickness of the film. In

[69] J. Krim and G. Palasantzas, J. Mod. Phys. B 1995, **9**, 599.

the RD model $\beta = 1/2$ and should be the maximum limit[70]. In the same RD picture, adding the fact that one island can nucleate when the bottom island has reached a certain size, before it is completed, the expression $\sigma = \sqrt{(1-\theta_c)dD}$ is found, where θ_c is the coverage corresponding to the critical top terrace size. RD model does not consider desorption or intermixing, so its value for the growth exponent should be considered only as a reference value.

In order to obtain non trivial information, one has to take in account also of the prefactors of the power law fitting. In some organic semiconductor films people found $\beta > 1/2$, but a careful analysis looking also at the prefactor has shown that the absolute values for the roughness are bottom the RD line and the observed regime is a transient. The interesting, materials specific, information, according to J. Krug, is the temperature dependence of the prefactors of the log-log plot of the power laws above.

Power Spectral Density (PSD) is extended used in thin films surface. It is the Fourier decomposition of the image in the spatial frequencies. The angular average of all the PSD spectra (Radial PSD–RPSD) can be computed in order to rule out possible anisotropic effects.

Hybrid interfaces

Now the hybrid interface topic will be introduced, a central concept for the present thesis. A hybrid interface is the separation between two materials (interface) one of which is inorganic and another is organic (hybrid). We focus on the interfaces originated in vertical structures by the sequential deposition of several layers. It is a topic of great interest not only for hybrid spintronics, but also for the classic organic electronics. It is an experimental evidence that the *order* of the interface does matter: the deposition of organic semiconductor (OSC) molecules on a metallic layer or the deposition of metals onto an organic surface present important differences.

The conceptual physical difference between this two interfaces lies in the fact that the two interfacing materials are characterized by different bond strength[71] and thermodynamics. Organic materials are bound by weak van der Waals (vdW), while the metals atoms are bound by strong covalent type interactions with electrons sharing. The heat of condensation of molecules is much smaller than that of metals. In the organic-on-metal interface, the metal atoms are strongly bonded

[70] J. Krug, Physica A, 2002, **313**, 47.
[71] A. Kahn, N. Koch, W. Gao, J. Pol. Sci. B 2003, **41**, 2529.

and constitute a stable surface for the low-energy organic molecule and neither diffusion of metal atoms into the organic film nor organic molecule diffusion into metal is expected. In contrast, for the metal-on-organic case, the metal atoms impinging on the organic film release enough condensation energy to disrupt the weakly bonded vdW solid and diffuse below the surface.

Furthermore chemical concepts regarding the intramolecular strength shall be carefully considered: the metal deposited can react with the organic giving raise to metal-organic complexes. OSC which are metal-organic complexes by themselves will react more easily.

Organic on metal interfaces

Consider the deposition of OSC onto a metallic layer From the Schottky theory we know that when a conventional semiconductor and a metal are in close contact, it happens a migration of electrons from the semiconductor to the metal, whose driving force is the Fermi levels (FL) alignment, supposing the vacuum level (VL) for the electrons is constant. The extension of the depletion region is $X_D = \sqrt{\frac{2\varepsilon(\phi_M - \phi_S)}{en}}$ where ϕ_M and ϕ_S are the work functions of the metal and semiconductor respectively, ε and n are respectively the dielectric constant and the carrier density of the semiconductor. Since OSC have a very low carrier concentration (10^{10} –10^{12} cm^{-3}) the space charge region should extend for length of the order of magnitude of hundreds microns. Let us consider the Co/Alq_3 interface: ϕ_{Co} is 4,9 eV , the FL of Alq_3 can be considered in the middle of the gap (4,1 eV under the vacuum level VL) and the relative dielectric constant is 4[72]. It is found that the depletion region should extend in the Alq_3 film for 200 μm for the equilibrium to be reached. Since OSC thin film are much more thinner the equilibrium is not reached and the VL has to suffer a strong shift with the creation of an interface dipole[73]. Few other effects contribute also to the dipole formation in OSC: charge transfer from or to the metal, charge image forces, chemical interactions, surface states, as well as permanent molecular dipoles (some OSC, such as Alq_3, have a their own intrinsic dipole).

The interface states induced by the metal/molecule interaction are of special interest for any electronic application. For example, the very recent result found by Zhan and coworkers for the Alq_3/Fe system: at this interface charge redistribution and exchange coupling induce an antiparallel spin polarized (empty) state between the Iron FL and the Alq_3 LUMO[74]. Since the

[72] S.Berleb, W.Brütting, Phys.Rev.Lett. 2002, **89**, 286601.
[73] H.Ishii, K Sugiyama, E Ito, K Seki, Adv. Mat. 1999, **11**, 605.
[74] Y. Zhan, E. Holmström, R. Lizàrraga, O. Eriksson, X. Liu, F. Li, E. Carlegrim, S. Stafström, M. Fahlman, Adv. Mat. 2009, **21**,1.

injection is a tunneling process from the electrode FL into the closest permitted molecular level, this result suggest that the spin polarized injection from Fe into Alq_3 proceeds via minority spin states.

By Photoemission Sectroscopy FL and VL are measured at the surface of the metal. When OSC is deposited on top, both FL and VL shift. The FL shift gives the distance between the HOMO level of the OSC and the FL of the metal, while the VL shift is a measure of the interface dipole Δ. A VL shift toward lower value (i.e. $\Delta < 0$) means that OSC is electron-donor: the dipole points towards the metal side, which is usual for OSC.

Metal on organic interface

We stressed out the fundamental differences between this interface and the previous one. The metal penetrating in the OSC can in principle do both react or form clusters. But, for instance, in Mg/Alq_3 [72] and In/PTCDA [75] systems only reaction without clustering was observed.

An important indication of how the growth parameters influence the quality of the interface is given by the system Au/DIP[76]. For the gold deposition it was found that:

-low substrate temperatures and high deposition rate give a well defined interface and small metal penetration (analysis by Transmission Electron Microscopy and Rutherford Backscattering Spectroscopy);

-high substrate temperatures combined with low deposition rates give consistent Au penetration and interdiffusion.

These data are explained by considering that the low temperature and high rate increase the probability that adsorbed atoms form less mobile islands, limiting the diffusion in the OSC film.

Few more examples of metal-OSC interaction are the systems Mg/Alq_3[77], Au/Fe_2CuPc [78], Au/6P[79], Ca/Alq_3, Li/Alq_3, K/Alq_3, Al/Alq_3, LiF/Alq_3[80], while the system Sm/6P[81] does not show interaction induced modifications.

[75] Y. Hirose, A. Khan, V. Aristov, P. Soukiassian, Appl. Phys. Lett. 1996, **68**, 217.
[76] A.C. Dürr, F. Schreiber, M. Kelsh, h.D. Carstanjen, H. Dosch, Adv. Mat. 2002, **14**, 961.
[77] A. Rajagopal, A. Kahn, J. Appl. Phys. 1998, **84**, 355.
[78] C. Shen, A. Kahn, J. Appl. Phys. 2001, **90**, 4549.
[79] H. Oji, E. Ito, M. Furuta, K. Kajikawa, H. Ishii, Y. Ouchi, K. Seki, J. Electron Spectrosc. Relat. Phenom. 1999, **101**, 517; K. Seki, N. Hayashi, H. Oji, Y. Ouchi, H. Ishii, Thin Solid Films 2001, **393**, 298.
[80] M.G. Mason, C.W. Tang, L.-S. Hung, P. Raychaudhuri, J. Madathil, D.J. giesen, L. Yan, Q.T. Le, Y. Gao, S.-T. Lee, L.S. Liao, L.F. Cheng, W.R. Salaneck, D.A. dos Santos, J.L.Bredas, J. Appl. Phys. 2001, **89**, 2756.
[81] N. Koch, E. Zojer, A. Rajagopal, J. Ghjisen, R.L. Johnson, G. Leising, J.-J. Pireaux, Adv. Funct. Mat, 2001, **11**, 51.

Oxides on organic

Insulating oxide thin films have extensive application in many technological sectors, from MOSFET gates to circuits insulations or mechanical improvement of the hardness of turbines, rotors, and others. Obviously, oxide layer applications are also relevant for organic electronics, in particular they are used as tunnel barriers, capping layers[82] and as insulating gate layers in both bottom and top gated OFETs. Like for the metals, the deposition of OSC on oxide surfaces and that of oxides on organics present similar differences. Of course, if the oxide layer is produced by depositing the metal followed by its oxidation the situation is reduced exactly to the metal-on-organic case. On the other hand, when the oxide is directly deposited the process is completely different, first due to the presence of oxidant atmosphere (not UHV) and second due to much lower diffusivity of the larger oxide radicals and clusters. Despite this promises, the experimental studies of oxide thin film deposition on organic is very limited to a few examples, and also for top gate OFETs people usually use organic dielectric instead of oxides layers.

Oxides and halogenides are often inserted between the organic layer and the top contact on OLEDs, in order to improve device performances. However an accurate investigation of the growth of these buffer layers is essentially lacking.

Yttrium oxide[83], Cerium oxide and Silicon oxide[84] were depoited on Polyvinilpropilene (PVP) by e-beam evaporation in O_2 atmosphere. Tin[85] and Nickel[86] oxides evaporation on pentacene was also experienced. Al_2O_3 was efficiently used in OLEDs. The aluminum oxide was realized by oxidation of a layer of Al directly deposited on the Alq_3[87]. In this case a chemical interaction happens when Aluminum atoms get in contact with Alq_3; good injection properties are thought to be linked to Alq_3^- anions formed as a consequence of a charge transfer reaction[88]. In many case it is better to deposit directly the oxide film in oxygen atmosphere. A relevant improvement was obtained for top emitting Alq_3/α-NPD OLEDs by 1 nm thick sputtered MgO

[82] S.-H.K. Park, J. Oh, C.-S. Hwang, j.-I. Lee, Y.S. yang, h.Y. Chu, Electrochem. Solid-Sate Lett. 2005, **8**, H21; S. Ferrari, F. Perissinotti, E. Peron, L. Fumagalli, D. Natali, M. Sampietro, Org. Electr. 2007, **8**, 407.
[83] D.K. Hwang, J.-M. Choi, J.H. Park, J.H. Kim, E. Kim, S. Im, Electrochem. Solid-Sate Lett. 2007, **140**, H117.
[84] K. Lee, J.H. Kim, S. Im, C.S. Kim, H.K. Baik, Appl. Phys. Lett. 2006, **89**, 133507.
[85] W.J. Kim, W.H. Koo, S.J. Jo, C.S. Kim, H.K. Baik, D.K. Hwang, K. Lee, J.H. Kim, S. Im, Electrochem. Solid-State Lett. 2006, **9**, 251.
[86] J. Lee, D.K. Hwang, J.-M. Choi, K. Lee, J.H. Kim, S. Im, J.H. Park, E. Kim, Appl. Phys. Lett. 2005, **87**, 023504.
[87] F. Li, H. Tang, J. Anderegg, J. Shinar, Appl. Phys. Lett. 1997, **70**, 1233; S.T. Zhang, X.M. Ding, J.M. Zhao, H.Z. Shi, J. He, Z.H. Xiong, H.J. Ding, E.G. Obbard, Y.Q. Zhan, W. Huang, X.Y. Hou, Appl. Phys. Lett. 2004, **84**, 425; S.T. Zhang, Y.C. Zhou, J.M. Zhao, Y.Q. Zhan, Z.J. Wang, Y. Wu, X.M. Ding, X.Y. Hou, Appl. Phys. Lett. 2006, **89**, 043502.
[88] M.G. Mason, C.W. Tang, L.-S. Hung, P. Raychaudhuri, J. Madathil, D.J. giesen, L. Yan, Q.T. Le, Y. Gao, S.-T. Lee, L.S. Liao, L.F. Cheng, W.R. Salaneck, D.A. dos Santos, J.L.Bredas, J. Appl. Phys. 2001, **89**, 2756.

buffer layer insertion between the cathode and Alq_3[89]. Sputtered Indium Tin Oxide (ITO) deposition on organic polymer without damaging the molecular layer was reached by tuning and softening the deposition condition[90]. Plasma Enhanced Atomic layer Deposition (PE-ALD) of Al_2O_3 on PES[91] and Pulsed Laser Deposition (PLD) of ITO (O_2 chamber pressure: 52 mbar) on PET[92] were found to lead to a roughness smoothing. Recently, ALD grown 2 nm thick Al_2O_3 buffer layer, inserted between the organic surface and the top metal contact, was demonstrated to improve the device performances of organic devices[93].

From an overall consideration it comes out that very thin oxide buffer layer deposited on OSC surfaces is a promising way to tailor metal-on-OSC interface in order to improve the devices. Besides, it appears clearly that it is important to directly deposit oxide (and not to oxidize a previously deposited metal film) looking for soft deposition.

Basic concepts of injection and transport in organic semiconductors

Organic semiconductors (OSC) combine a strong intramolecular carbon—carbon bonding with a weak van der Waals interaction between molecules. This combination of different interactions generates unusual materials whose optical properties are very similar to those of their constituent molecules, whereas their transport properties are firmly instead governed by the intermolecular interactions.

As a general rule, there are two very different classes of OSC: small molecules and polymers. These two cases differ by their physical and chemical properties, but also by their technological processing. Small molecules organic semiconductors are rigid objects of about 1 nm size, with very different shapes and symmetries, but able to form highly ordered van der Waals layers and polycrystalline films. The small molecule film growth involves either high or ultra high vacuum molecular beam deposition. A few of the main representatives of this kind of materials are the classes of oligothiophenes (4T, 6T and others), metal chelates (Alq_3, Coq_3 and others), metal-

[89] H.W. Choi, S.Y. kim, W.-K. Kim, J.-L. Lee, Appl. Phys. Lett. 2005, **87**, 082102.
[90] D. Vaufrey, M.Ben Khalifa, J. Tardy, C. Ghica, M.G. Blanchin, C. Sandu, J.A. Roger, Semicond. Sci. Technol. 2003, **18**, 253; J.V. Anguita, M. Thwaites, B. Holton, P. Hockley, S. Rand, S. Haughton, Plasma Process. Polym. 2007, **4**, 48.
[91] S.-H.K. Park, J. Oh, C.-S. Hwang, j.-I. Lee, Y.S. yang, h.Y. Chu, Electrochem. Solid-Sate Lett. 2005, **8**, H21
[92] H. Kim, J.S. Horwitz, G.P. Kushto, Z.H. kafafi, D.B. Chrisey, Appl. Phys. Lett. 2001, **79**, 284.
[93] M.J. Preiner, N.A. Melosh, Appl. Phys. Lett. 2008, **92**, 213301.

phtalocyanines (CuPc, ZnPc and others), acenes (tetracene, pentacene and others), rubrene and many more. Polymers, on the other hand, are long chains formed from a given monomer, and usually feature connection of oligo-segments of various lengths leading to a random conjugation lengths distribution. Polymer films are strongly disordered and generally cannot be produced in UHV conditions; instead totally different processing technologies have to be applied, including ink-jet printing, spin coating, drop casting and other extremely cheap methods. This potentially inexpensive fabrication constitutes one the main technological advantages of the polymers. However, these growth approaches generally preclude a real interface control, as the electrode surface is not as clean as in UHV conditions and cannot be directly characterized by such important surface techniques as XPS, UPS, XMCD and others.

The objective of this paragraph is to show the relevant aspects and the main differences between OSC and traditional inorganic semiconductors and metals with respect to the charge transport. In most cases OSC do not have bands, but electronic levels descending from the molecular orbitals of separate molecules. When they are put together in a film, they do not form a continuous level (a band), but the levels are still located on the molecules with a little overlap. Since the energetic disorder is usually more than the width of the levels (~0,1 eV[94]), the levels are further localized (Anderson localization). Temperature induced disorder contributes to the localization[95], and the thermalization length (the length at which a carrier reach a thermodynamic equilibrium with its surroundings) is 0,1–1 nm. Furthermore, impurities do not induce additional carriers like in inorganic semiconductors but mainly generate trap states. As a consequence the mean free path of a charge carrier is of the magnitude order of the intermolecular distance: the transport of a charge carrier occurs by *hopping* between adjacent molecules – localized states. In conventional chemical terms it means a reduction of the molecule and a following oxidation, when the carrier leaves it.

The hopping mechanism is quite different from energy band transport, it is important all the band-like concepts and knowledge to be treated very carefully in OSC.

The conventional transport picture starts with the *free electron model* which provides the electronic states in the form of travelling waves $e^{i\mathbf{k}\cdot\mathbf{x}}$ having constant density in the **k** space: $\frac{dn}{d\mathbf{k}} = \frac{V}{4\pi^3}$, V is the macroscopic volume of the specimen. The energy scales as $\mathbf{k}^2$. Let us consider N free electrons occupying a sphere (*isotropic* volume) in the **k**-space with this density. The

[94] M. Pope.C.E. Swenberg, *"Electron Processes in Organic Crystals, Polymers"*, Oxford University Press, 2nd ed.
[95] J.C. Scott, J. Vac. Sci. Technol. A, 2003, **21**, 521.

density of states (DOS) is $\frac{3m}{\hbar^2(3\pi^2)^{3/2}}E^{1/2}$. For, and only for, charge carriers having *free* character and occupying an *isotropic* volume in the **k**-space, the density of states goes as $E^{1/2}$.

Shifting from *free* to *near free* electrons, constrained in a periodic potential due to the lattice, the electron wave function is a *Bloch state* . which differs from the plane wave only by a periodic modulation[96]: this is the *Bloch theorem* and is the conceptual starting point from the energy bands picture in solids[97]. In the plane wave frame, from the classical definition of the group velocity for a wave, the effective mass tensor is obtained: $\underline{\underline{m}}^{-1} = \frac{1}{\hbar^2}\frac{d^2E(\mathbf{k})}{d\mathbf{k}^2}$.

The traditional transport concept allows to understand few important issues: the exponential form of the wave function for the electron, the charge carrier velocity as the slope of the energy dispersion law (with the respective sign) and the effective mass as the second order derivative of the E(**k**) law, own a meaning only in the *free* or *near free* electron approximation of a material owing a periodical structure (lattice) and a conduction band, while a density of states (DOS) going as $E^{1/2}$ needs also of an *isotropic Fermi sphere*. In this latter case the effective mass is a scalar number. Indeed the described concepts are central for the transport treatment in inorganic semiconductors, while they mostly do not hold for OSC.

OSC do not have a proper energy bands and can hardly be described by the Fermi sphere. Thus most of the above mentioned concepts cannot be transferred to OSC. The charge carriers will have a velocity and a mass, of course, but they are not expressed by the conventional laws of inorganic semiconductors. From the other hand the carrier density in OSC can be expressed, like in conventional semiconductors, by $n_{(E,T)} = \int_0^\infty g_{(E)} f_{(E,T)} dE$, where *g* is the density of states function and *f* the Fermi-Dirac occupation probability function; in OSC the challenge is the definition of *g*. Since OSC have large band gap and small carrier concentration, they are far to be degenerate and the Boltzmann statistics can be applied. By considering OSC as intrinsic semiconductors, the carrier concentration is $n_{i(T)} = N_{eff} \exp\left(-E_g / 2k_B T\right)$, where an appropriate expression for the effective carrier densities shall be found, as the conventional description comes out from the free electron model and are not suitable. For N_{eff} we can consider the molecule density. If we consider two possible electrons in the LUMO, it shall be considered a new HOMO and the situation would be similar, but with double charged molecules. So it seems correct to assign only one electron per molecule: that level becomes the Single Occupied Molecular Orbitals

[96] F.Bloch, Physics Today, December 1976.
[97] C. Kittel, "Introduction to Solid State Physics", WILEY; 8th edition (November 11, 2004).

(SOMO) and the molecule has only one additional charge to accommodate by distortion (polaron). For instance, from Alq_3 data[98] one obtains a molecules density of $2{,}0 \cdot 10^{21}$ cm^{-3} and, since the gap is 2,8 eV wide, a thermally generated carrier density of $8 \cdot 10^{-3}$ cm^{-3} is obtained, which is absolutely negligible with respect to expected 10^{10} cm^{-3} and indicates the inappropriateness of the approach, possibly for a non trivial form of the DOS function. Further, the generalized Einstein relation can be used in principle whether the equilibrium condition is reached.

The electrical properties of OSC are usually depicted by two main components: charge injection and charge transport. The charge injection process from a metal into an OSC is conceptually different from the case of metals/inorganic semiconductors, mainly by the vanishingly low density of intrinsic carriers – about 10^{10} cm^{-3} in OSC[99]. The external electrodes provide the electrical carriers responsible for the transport as the OSC molecules can easily accommodate an extra charge, although this charge modifies considerably the molecular spatial conformation and creates strong polaronic effects (a distorsion of the molecular structure), which contributes to the localization of the levels. The carriers propagate via a random site-to-site hopping between pseudo-localized states distributed within approximately a 0,1 eV energy interval. This interval describes the spatial distribution of the localized levels and has not to be confused with the bandwidth. OSC are mainly families of π-conjugated molecules, which combine a considerable carrier delocalization inside the molecules with a weak van der Waals intermolecular interaction that limits considerably the carrier mobility. The electron mean free path is usually of about a molecule size, namely about 1 nm, while standard nobilities are well below 1 cm^2/Vs. Two conducting channels are usually considered active: LUMO (Lowest Unoccupied Molecular Level) for *n*-type and HOMO (Highest Occupied Molecular level) for *p*-type carriers. However, defects and interface states have to be considered depending on the material and its structural quality.

Considering dominant scattering mechanisms in disordered OSC, it was shown that in molecularly doped polymers or amorphous films of the small molecules the disorder contribution to the hopping activation energy is always dominant[100]. In ordered systems, like crystalline pentacene islands, the polaron dynamics is supposed to govern transport properties. The Boltzmann equation used in conventional semiconductors transport[101] becomes in OSC a master

[98] See page 74.
[99] W Brütting, S Berleb, AG Mückl, Org. El. 2001, **2**, 1.
[100] V.I. Arkhipov, I.I. fischuk, A. Kadashchuk, H. Bässler, in "Photophysics of Molecular Materials", WILEY, December 2005.
[101] C. Kittel, "Introduction to Solid State Physics", WILEY; 8th edition (November 11, 2004)..

equation $\frac{\partial f_i}{\partial t} = \sum_{i \neq j} w_{ji} f_j (1 - f_i) - \sum_{i \neq j} w_{ij} f_i (1 - f_j) - \lambda_i f_i$, where f_i is the occupation probability of the i–site, it is a time dependent quantity, but the time dependence is omitted to simplify the notation, w_{ij} is the hopping probability from site i to site j, λ_i is the decay rate for the carrier wave function in the i–site[102]. The extension of the sum over all the sites account for multiple jumps, as the electron will make the fastest possible, which does not necessary mean the first neighbor molecule as it depends also to the energy difference. The first term describes a hop in the site i, which increase the temporal derivative of f_i; the second a jump from the i–site. Many efforts on the transport studies in OSC focus on the definition of w, but a general accepted picture is not still reached. The most and generally accepted description of the hopping between localized states is the Variable Range Hopping (VHR)[103]. Its basic concept is that the electron in a site will select the most convenient between two possibilities: hopping in the spatially nearest site or hopping in the energetically closest site. So the hopping rate is expressed as $w_{ji} = \nu_0 \exp\left(-2\alpha \left| R_{ij} \right| - \frac{\varepsilon_j - \varepsilon_i}{k_B T} \right)$, where α is the inverse localization radius, that is the result of the overlap integral of the sites wave functions, R_{ij} is the distance between the sites, ε the energy and ν_0 is the attempt frequency typically of the order of phonon frequency. Let us suppose that the site energy distribution ρ is constant and isotropic (plausible in an amorphous material) so that the electron in the i-site sees the number of possible sites $N = \rho \left| \varepsilon_j - \varepsilon_i \right| \frac{4}{3} \pi \left| R_{ij} \right|^3$. By ensuring one hop ($N$=1) and by maximazing the exponential term, one finds the optimal sites distance (or the optimal site energy) $R_{opt} = \left(\frac{1}{8\pi \ \alpha \ \rho \ k_B T} \right)^{\frac{1}{4}}; \left| \varepsilon_j - \varepsilon_i \right|_{opt} = \frac{3}{4} \left(\frac{\left(8 \ \alpha \ k_B T \right)^3}{\pi \rho} \right)^{\frac{1}{4}}$. At room temperature, for a density of states of $2 \cdot 10^{21}$ cm^{-3} (the Alq_3 molecules density, which provides a reliable density of the possible target sites) and for α of nm^{-1}, the optimum distance is about 0,8 nm and the optimal energy interval 150 meV. By inserting the optimal values found in the hopping probability the VHR expression $w_{ji} \propto \exp\left[-\left(\frac{T_0}{T} \right)^{\frac{1}{4}} \right]$ is found, where the characteristic temperature T_0 contains information on the wave function overlap and the accessible density of states, which is often referred as the density of states at Fermi level. When the material is considered as a non

[102] N. Tessler, Y. Prezant, N. Rappaport, Y. Roichman, Adv. Mat. 2009, **21**, 2741.
[103] N.Mott, "Conduction in Non-Crystalline Materials", Clarendon Press-Oxford, 1987

degenerate semiconductor and the hopping rate could be averaged over all the sites, the effective transport energy (ε_T) can be considered, where all the hopping target are supposed to be at ε_T independently of the energy of the starting sites. The effective transport level plays formally the role of the mobility edge in impurity band conduction, but the conceptual background is different. In the effective transport energy, once the equilibrium is reached, the backward current is computed to cause a decrease of the current of about the 20%. Theoretical work on organic systems show that a charge transport across several microns is required in order to reach the steady state condition and charges moving across a thin sample, which is just the thickness condition of thin films used in organic electronics, can never be at equilibrium.

The primary event of the injection process is a tunneling from the extended state of the metal into a localized state of the OSC. Once a charge is injected, molecular deformation, nuclei relaxation and orbital polarization modify the energetic landscape. What one has to mind is that the LUMO position in respect to the vacuum level, the ionization energy, can be reduced, on a certain molecule, as a consequence of the polarization of the surrounding medium, by about 1eV. It consists in a reorientation of the molecular dipole, but it is a relatively slow process, which cannot be detected by UPS[104].

Thus a carrier at the metal-OSC interface sees an energy landscape very different from that measured by spectroscopic techniques. Experimental evidences in Alq_3 based devices reveal that they are interface injection limited (when the density of charge in the bulk is smaller than the interfacial one) and not transport limited[105]. Randomly placed dipoles cause a broadening of the LUMO and the creation of further interfacial levels whose broadening can be as high as half an electron volt. Local fluctuations in molecular energies can promote the efficient injection of charge carrier. Injection channels are composed of molecules with reduced energy, thanks to statistical fluctuations. This mechanism seems much more efficient than the injection through a barrier[106] but, because of statistical fluctuations, extrinsic states at the interface, randomness of the dipole orientation and sites energies, an *intrinsic quantitative irreproducibility* of the I-V curve[107] is expected.

A final remark on the presence of an *insulating layer* at the interface[108]. If this layer, e.g. a thin oxide layer, contains levels not accessible to the carrier, the injected electron will tunnel

[104] J.C. Scott, J. Vac. Sci. Technol. A, 2003, **21**, 521, section II.
[105] M.A. Baldo, S.R. Forrest, Phys. Rev. B 2001, **64**, 085201.
[106] A.L. Burin, M.A. Ratner, J. Pol. Sci. B 2003, **41**, 2601.
[107] M.A. Baldo, S.R. Forrest, Phys. Rev. B 2001, **64**, 085201; J.C. Scott, J. Vac. Sci. Technol. A, 2003, **21**, 521; A.L. Burin, M.A. Ratner, J. Pol. Sci. B 2003, **41**, 2601; N. Tessler, Y. Prezant, N. Rappaport, Y. Roichman, Adv. Mat. 2009, **21**, 2741.
[108] J.C. Scott, *Ibid.*, section VI.

through it towards the interfacial molecular levels. The injection rate will decrease for both forward and reverse currents, a back-diffusion can be prevented; but the injection is more difficult. The oxide layer changes the effective metal work function and the ions (oxides have a strong ionic character) lead to a net dipole moment which can raise or lower the LUMO and the interfacial states. From the other side an insulating layer at the interface could originate new interfacial state very close to the metal Fermi level which improve the injection. Finally if the oxide layer resistance is higher than the OSC film, it accommodates the voltage drop between the metal and the organic and pins the Fermi levels.

2. Experimental techniques

Thin film deposition by means of pulsed electron beams (channel spark ablation)

Channel Spark Ablation (CSA) is recently among most innovative and powerful growth techniques used for the oxide thin film deposition. A significant part of work during this thesis was dedicated to the optimization of the CSA parameters and protocols for oxide deposition.

Introduction

Channel Spark Ablation is a technique for the thin film deposition and it is particularly powerful in the case of composite materials. CSA main advantages are the simplicity and low cost, together with the preservation of the target stoichiometry. It has been successfully applied in the last years for the deposition of various complex oxides, like High T_C superconductors, ferromagnetic manganites and buffer layers for these materials. A general requirement for the deposition of complex oxide single phase films is the strong control of the composition during the deposition process, especially for multi-cation oxides with complex crystal structures. The formation of a specific oxide phase requires an optimization of both temperature and partial pressure of the chosen working gas. The growth conditions for epitaxial oxide films do not necessarily need to be consistent with the thermodynamic phase stability of the compound, as epitaxy can stabilize some phases outside of their thermodynamic stability range.

In the CSA process the deposition occurs by ablation of a target by means of pulsed, magnetically self-pinched, electron beams. Such pulsed beams are produced in a low pressure gas-filled channel spark device[109]. It consists of a pulsed electron beam generator and a target-sample system. The efficiency in converting the energy of the beam at the target is about 30% and the costs are typically 20 times lower than ones for a pulsed laser deposition (PLD) apparatus[110]. Other advantages of CSA, in comparison with PLD, are the possibility of ablation for transparent target

[109] G. Müller and C. Schultheiss, *10th Int. conf. on high power particle beams*, SanDiego, June 20-24 (1994).
[110] G. Müller G. *et al.* in *Science ant Technology of Thin Films*, edited by Matacotta F.C. and Ottaviani G. published by World Scientific Publishing Co. Pte. Ltd., 1995.

materials (because electrons are charged particles and interact with all type of materials), high gas ionization and easier scalability of the process.

The triggering system

The CSA, in its essentials, consists of a transient hollow cathode connected to a dielectric acceleration tube. The dielectric tube is connected through a narrow exit to the transient hollow cathode and picks up the electron flow for the final acceleration which form the electron beam. The inner wall of the deposition chamber is the actual anode.

Despite of its simplicity, it appears that only with a correct gun design one achieves beam values (electron energy spectrum, voltages, plasma density) so that the ablation is effective and the intrinsic versatility of the technique is really obtained[111]. The gun design includes the acceleration section and the trigger apparatus.

Figure 8: CSA system.

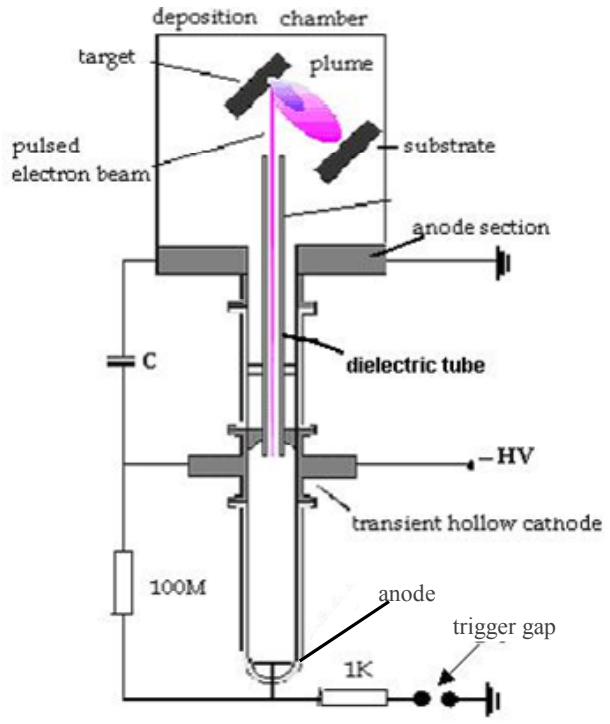

Figure 8 presents the triggering scheme used in the preset PhD thesis. Plasma originates in the discharge between the bottom electrode and the transient hollow cathode. The negative high voltage power supply is directly connected to the capacitor which is charged up and to the bottom circuit containing anode electrode, a charging resistor (100 MΩ in the figure) and a floating electrode of the spark gap. At a certain voltage a spark closes the air gap and it resistance becomes

[111] G.E. Ozur, S.A. Popov, V.F. Fedushchak, A.V. Saushkin, Tech. Phys. Lett. 2006, **32**, 928.

zero. As a consequence a rapid variation of the electric field occurs in the trigger bulb. The fast electric field variation ionizes the gas molecules (or atoms) and originates plasma, providing electrons in the hollow cathode cavity, where the discharge amplification happens, as explained in the next section. Because the charging resistor decouples the capacitors and the anode plate, the capacitors discharge on the cathode in the top part of the circuit (the hollow cathode, the grounded chamber, the capacitors) through the low impedance electron beam. The low impedance discharge cannot be sustained (since the power supply is limited in current) and it extinguishes. The current supplied to charge the capacitors defines the charging time and, hence, the operating frequency.

The voltage across the dielectric section accelerates the electrons escaped from the cathode and the so-called channel discharge occurs.

The pulsed electron beam generation

The beam originates by amplification of the plasma from the low pressure discharge produced in an electrical breakdown. The breakdown conditions states that the discharge takes the longest path, so in plane electrodes the discharge runs on the edges. A hole in the middle of the electrodes stabilizes this type discharge, and the gas discharge is concentrated in the region around the axis of the bore: it is called pseudospark discharge[112]. The beam formation occurs between the transient hollow cathode (which provides also the electrons for the beam) and one or more coaxial disk shaped metallic anodes with a hole in the middle. The beam propagates in a self focused way through the holes. By placing a dielectric tube between the cathode and the anode the discharge takes place in that tube: *channel spark discharge*. It presents several advantages: the absence of the voltage oscillations after the breakdown, because of the capacitive coupling between the beam and the anode via the dielectric tube; the beam pulse duration is higher providing higher energies per pulse[113]; channel spark gives more reproducible pulses[114].

The electron source for the beam is a transient hollow cathode. It is a hollow metallic structure, there is a cavity and a hole. The beam is generated by electron extraction in the cavity from the plasma created by a low pressure electrical breakdown. This can be a self breakdown process or it is triggered by an ignition discharge (the trigger discharge). The beam escapes through the hole toward the acceleration region: one or more hollow plates at anode potential (pseudospark system) or a glass tube between the hollow cathode and the anode which is the chamber itself (channel spark). The pseudospark device works fine at pressure higher than those in

[112] J. Christiansen and Ch. Schultheiss, Zeit. Phys. A 1979, **290**, 35.
[113] K. Frank, E. Dewald, C. Bickes, U. Ernst, M. Iberler, J. Meier, U. Prucker, A. Rainer, M. Schalug, J. Schwab, J. Urban, W. Weisser, D.H.H. Hoffmann, IEEE Trans. Plasma Sci. 1999, **27**, 1008.
[114] Q.D. Jiang, F.C. Matacotta, M.C. Konijnenberg, G. Müller, C. Schultheiss, Thin Solid Films 1994, **241**, 100.

the channel spark one, so in the latter a triggering predischarge is necessary. The electron beam parameters depend on the breakdown voltage, the pressure and the geometry, while a linear dependence of the maximum beam current on the external capacity is observed only in the channel spark device.

When the electron plasma reaches the cathode bore, the hollow cathode discharge starts. The plasma injection through the hole takes a few tens of second. The current rapidly increases and the voltage drops down. Electrons in the hollow cathode discharge have an energy comparable with the acceleration voltage. During the cathode discharge an avalanche process takes place increasing the density of the positive space charge and, as a consequence, the efficiency of the multiple ionization process; this means a strong enhancement of the current. After the hollow cathode discharge the conduction discharge occurs. It is characterized by a high current density of low energetic electrons[115]. When the duration of the breakdown voltage is smaller, the two discharges observed in the beam are partially or totally superimposed, and the total beam duration in the beam is shorter. It happens at higher gas pressure, small external capacitors, high breakdown voltages, and in the channel-spark systems, especially at high accelerating potentials[116].

Also, the filling gas plays a critical role not only for the deposition but also for the discharge. As a matter of fact M. Gastel and coworkers observed that by changing the hollow cathode dimensions, the discharge modifications with helium as filling gas followed the opposite trend in respect to the situation with neon as environment gas[117]. Moreover the applications of an external magnetic field along the axis obtains a best focused beam, since electrons follow the magnetic field lines. The external magnetic field influence is higher at low pressure and leads to a more dense plasma, a decrease of the discharge voltage and an enhancement of the current[118]. The spark in the dielectric tube and the beam propagation. Since several advantages exist for the channel-spark system, if compared with the pseudospark one[119], the channel spark device was used in the presented work and we are describing only the process of the spark formation and beam propagation in the dielectric tube, the “channel”, in this kind of system. Once the hollow cathode

[115] R. Stark, J. Christiansen, K. Frank, F. Mucke, M. Stetter, IEEE Trans. Plasma Sci. 1995, **23**, 258; R. stark, O. Almen, J. Christiansen, K. Frank, W. Hartmann, M. Stetter, IEEE Trans. Plasma Sci. 1995, **23**, 294; E. Dewald, K. Frank, D.H.H. Hoffmann, R. Stark, M. Ganciu, B.N. Mandavhe, M.G. Nistor, A.-M. Pointu, I.I. Popescu, IEEE Trans. Plasma Sci. 1997, **25**, 272.

[116] E. Dewald, K. Frank, D.H.H. Hoffmann, R. Stark, M. Ganciu, B.N. Mandavhe, M.G. Nistor, A.-M. Pointu, I.I. Popescu, IEEE Trans. Plasma Sci. 1997, **25**, 272; K. Frank, E. Dewald, C. Bickes, U. Ernst, M. Iberler, J. Meier, U. Prucker, A. Rainer, M. Schalug, J. Schwab, J. Urban, W. Weisser, D.H.H. Hoffmann, IEEE Trans. Plasma Sci. 1999, **27**, 1008; E. Dewald, K. Frank, D.H.H. Hoffmann, A. Tauschwitz, IEEE Trans. Plasma Sci. 2002, **30**, 1820.

[117] M. Gastel, H. Hillmann, F. Muller, J. Westheide, IEEE Trans. Plasma Sci. 1995, **23**, 248.

[118] V. Burdovitsin, E. Oks and A. Serov, High Power Particles Beams, 1998, BEAMS ’98. Proceeding of the 12th International conference on, 1998, **1**, 412.

[119] Q.D. Jiang, F.C. Matacotta, M.C. Konijnenberg, G. Müller, C. Schultheiss, Thin Solid Films 1994, **241**, 100.

has produced the plasma, the beam moves in the background gas along the dielectric channel. In order to obtain high current density, space charge must be compensated. This would require that the tube is filled with ionized gas…but charged particles are well accelerated in vacuum. A fast-spreading plasma channel is generated and the electron beam moves nearly space-charge neutralized through this channel. The most feasible correct scheme, from the standpoint of beam focusing, is as follows. The magnetic contraction of the beam should be equilibrated by Coulomb repulsion. Estimates show that, at a high current buildup rate and small density of plasma electrons inside the beam (i.e., at a relatively low gas pressure), the beam features a strong radial electric field that pulls ions to the axis. This field is enhanced at a definite beam contraction by the intrinsic magnetic field, since a certain fraction of ions will occur (because of their inertia) outside the beam. Then, the ions will move (driven by the radial electric field) toward the axis so as to restore the neutrality, but the injection of a new portion of electrons and the magnetic contraction will again violate it, and so on. With this dynamics, the longitudinal velocity of electrons will not drop as significantly as in the case of pinching, and the current density will gradually increase during the pulse as ions are accumulated in the paraxial region[120].

The glass or ceramic tube is a very important part of the channel spark system. As a matter of fact the charge carrier multiplication takes place not only in the cathode, but over the whole path of the beam in the capillary. The secondary emission from the tube walls is probably more important than the gas ionization adds to the bulk ionization, i.e. the release of electron from gas atoms by collision, Finally materials from the cathode and the capillary can be sputtered and ionized. These are the most relevant processes. Strong ionization processes happen in the tube leading to a positively charging of the inner wall. As a matter of fact the increase of the tube length leads to an increase in the current thanks to secondary emission electrons. At pressure of the order of 10^{-3} mbar or less, the beam is "effectively transported along the distance of ~ 15 cm inside the glass tube"[121].

As observed by Dediu and coworkers[122], by varying the geometry of the dielectric section, the voltage and pressure conditions are dramatically changed, in order to perform an optimal deposition. This is due to the peculiar beam interaction with the channel walls. For each singular geometry one finds that a pressure exists so that above this value the discharge is "regular" and

[120] G.E. Ozur, S.A. Popov, V.F. Fedushchak, A.V. Saushkin, Tech. Phys. Lett. 2006, **32**, 928.
[121] Y.E. Krasik, S. Gleizer, K. Chirko, J.Z. Gleizer, J. Felsteiner, V. Bernshtam, F.C. Matacotta J. Appl. Phys. 2006, **99**, 063303.
[122] V.I. Dediu, Q.D. Jiang, F.C. Matacotta, P. Scardi, M. Lazzarino, G Nieva, L. Civale, Supercond. Sci. Technol. 1995, **8**, 160.

below it the discharge is “high resistive” [123]. The “high resistive” mode is observed at lower gas pressure and is interesting for applications such as material processing and thin film depositions. In the ”high resistive” mode a uniform plasma develops in the entire volume of the capillary. Here the dominant charge carrier multiplication is the bulk one. In the “regular” mode operation (above a certain limit pressure, which changes according to the geometry) the trigger discharge ignites only the breakdown which occur considerably earlier than the decay of the trigger current.

Because of the capacitive coupling between the anode and the discharge plasma, a combination of a high energy beam electron and discharge plasma electrons are emitted in the drift space through the exit of the dielectric tube[124]. At low gas pressure both beam and discharge plasma electrons have relatively high energies, which explains the heigher efficiency in material processing[125]. Electron beam can be transported for a length of several centimeters without significant energy loss at low pressure[126].

A pressure dependence like this is found also elsewhere in literature[127]. In particular Jiang and coworkers[128] solved the problem of how to obtain a good oxygenation of the ablated species while keeping the background pressure at low values, by introducing the gas directly into the plume.

About the cathode hole, increasing the diameter up to a certain value determines the current increase; a further increase does not lead to a significant change in the current. The same is about the voltage: if it raises up the ablation efficiency and the film deposition rate increase but above a certain value this trend stops[129].

Aga and coworkers[130] analyzed the ablation efficiency by varying pressure and voltage. They found that the beam current dependence on the voltage *I(U)* changes tremendously at a certain value of pressure, indicated as the optimum one. In particular it is recommended to operate above this pressure in order to obtain reproducible pulses. For their apparatus the critical pressure

---

[123] E. Dewald, K. Frank, D.H.H. Hoffmann, A. Tauschwitz, IEEE Trans. Plasma Sci. 2002, **30**, 363;
Y.E. Krasik, S. Gleizer, K. Chirko, J.Z. Gleizer, J. Felsteiner, V. Bernshtam, F.C. Matacotta J. Appl. Phys. 2006, **99**, 063303.
[124] K. Frank, E. Dewald, C. Bickes, U. Ernst, M. Iberler, J. Meier, U. Prucker, A. Rainer, M. Schalug, J. Schwab, J. Urban, W. Weisser, D.H.H. Hoffmann, IEEE Trans. Plasma Sci. 1999, **27**, 1008.
[125] E. Dewald, K. Frank, D.H.H. Hoffmann, A. Tauschwitz, IEEE Trans. Plasma Sci. 2002, **30**, 363.
[126] Y.E. Krasik, S. Gleizer, K. Chirko, J.Z. Gleizer, J. Felsteiner, V. Bernshtam, F.C. Matacotta J. Appl. Phys. 2006, **99**, 063303.
[127] Q.D. Jiang, F.C. Matacotta, G. Masciarelli, F. Fuso, E. Arimondo, M.C. Konijnenberg, G. Müller, C. Schultheiss, G. Sandrin, Supercond. Sci. Technol. 1993, **6**, 567;
Q.D. Jiang, F.C. Matacotta, M.C. Konijnenberg, G. Müller, C. Schultheiss, Thin Solid Films 1994, **241**, 100;
Y.E. Krasik, S. Gleizer, K. Chirko, J.Z. Gleizer, J. Felsteiner, V. Bernshtam, F.C. Matacotta J. Appl. Phys. 2006, **99**, 063303.
[128] Q.D. Jiang 1993, cited.
[129] Q.D. Jiang 1994, cited.
[130] R.S. Aga Jr., C. Cox, A. Ueda, E. Jackson, W.E. Collins, R. Mu, J. Va. Sci. Technol. A 2006, **24**, L11.

was 13 mbar. As *I(U)* is strongly design dependent, also this pressure reference value depends on the geometry characteristics.

Thus the voltage determines: the accumulated charge Q=C·V, the total stored energy E=1/2 C·V^2, the threshold for the spark ignition and the strength of the plasma amplification in the hollow cathode, the energy distribution of the electrons in the beam and the length of the pulse; the pressure determines: the density of the plasma, the length of the pulse, the energy distribution of the electrons in the beam; the current from the power supply determines the capacitors charging time, i.e. the frequency of the pulses. The charge carrier multiplication process which occur inside the quartz tube play a very important role in the operation of the channel spark system, so one has to be careful in the design, of both the dielectric and the triggering sections.

Beam-target interaction and plume expansion

Ablation or ("sublimation by explosion") is a process where a high energy is transferred instantaneously to a small part of the target and brings it to temperatures above sublimation limit. Ablation depth is determined by the energy absorption depth of the material and the heat of vaporization of the work material. The depth is also a function of the beam energy density and of the pulse duration. Depending on the physical properties of the target materials, thermal conductivity leads to a more or less strong heat flow into the bulk material.

The ablation efficiency, in competition with the simple heating, is related to the rapidity of the energy transfer from the beam to by the target. This is expressed by[131] $\frac{dT}{dt} = \frac{IU}{\rho SC(D + D_T)}$, where the temporal derivative of the temperature of the target is function of the electron beam current I and the acceleration voltage U, the target density ρ, the beam cross section S, the target specific heat C, the electron adsorption length D and the thermal diffusion length D_T. Less dT/dt, more the ablation efficiency. Higher voltage and beam current, higher target density and specific heat and beam cross section, favor the ablation. Most of the ablated material escapes in the form of atomic flow, while clusters formation depends strongly on the target density and thermal conductivity, beam energy and energy density, and it is in principle different for every deposited material.

[131] M. Strikovski, K.S. Harshavardhan, Appl. Phys. Lett. 2003, **82**, 853.

Figure 9: Scheme for ablation process.

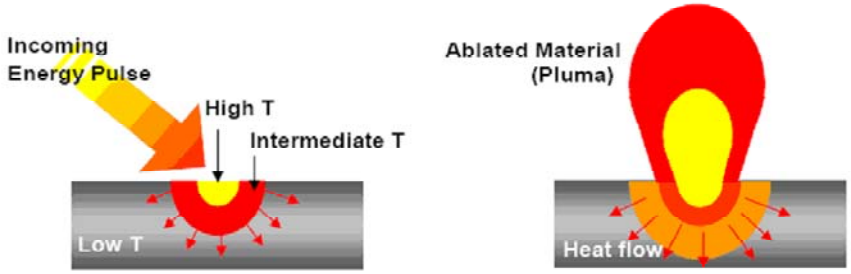

One has to consider also that a harder material does not necessarily need a stronger pulse. It is true for metals, in order to compensate the heat dissipation. As for oxides, which have low thermal conductivity, a higher voltage means a deeper penetration. It follows a greater heated volume, and it could determine a higher heat dissipation. There exist a fundamental difference in the heat flow in the target between oxides (or nitrides) and metals. The latter require high voltage in order to compensate heat dissipation, (metallic targets don't present significant heating signs[132]) whereas the former require a high enough voltage to reach the ablation threshold. Nevertheless too high voltage can produce excessively large heated volumes. This is why people observe that increasing the voltage above a certain value the ablation efficiency for a ceramic target does not increase, if not decreases[133]. Conducting oxides behave like insulating oxides: what does make matter is the thermal conductivity.

Figure 10: In thermally insulating target the surface of penetration increases by increasing voltage, and the dissipative effects do the same, so the ablation is not more efficient at higher again voltage.

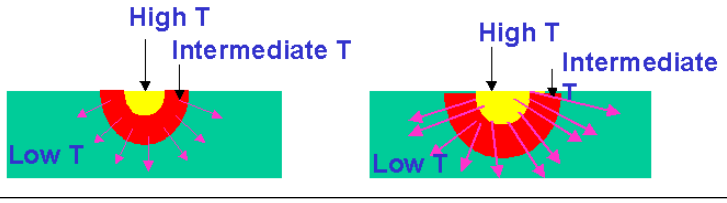

As a matter of fact the energetic composition of the beam is determinant for the film quality, specially for the stoichiometry preservation. The rapidity of the process let the target stoichiometry preserved in the film. A variation of the energy density at the target does not affect the film stoichiometry, once it is enough to the eruptive removal of the material from the target [134]. If the

[132] W. Bunker, J. Christiansen, K. Frank, H. Gundel, W. Hartmann, T. Redel, M. Stetter, IEEE Trans. Plasma Sci. 1989, **17**, 754; J. Christiansen and Ch. Schultheiss, Zeit. Phys. A 1979, **290**, 35.
[133] Q. D. Jiang, F.C. Matacotta, M.C. Konijnenberg, G. Müller, C. Schultheiss, Thin Solid Films 1994, **241**, 100.
[134] M. Höbel, J. Geerk, G. Linker, C. Schultheiss, Appl. Phys. Lett. 1990, **56**, 973.

energy density is not so high to let the simultaneous eruption of all the chemical elements, the Joule heating will cause only a "simple heating", without sublimation by explosion. Thus the film will be enriched of the species with the lowest vaporization temperature (weakest bond), while it will be poor of the element with the strongest bonds. The film composition will not reflect the target one and the main advantage of this technique is lost.

The atoms leave the target surface in a plume which follows the direction normal to the target surface. The plume mainly consists of single and double ionized species, in contrast with laser plume which contains mainly neutral atoms[135]. Moreover the channel-spark plasma maintains the high electron energy during the plume expansion at times well after the pulse[136]. These highly energetic ions promote the film growth thanks to their intrinsic kinetic energy and to the heating of the substrate surface (also if it is kept at room temperature). Investigations show that the plume does not expand in a compact way. The double ionized species moves faster than the single charged ones, which are quicker than the neutral atoms[137].

Plume expansion is also related to the gas species and pressure. As example, increasing pressure from 15 to 30 mTorr (but we stress this is strictly related to the geometry of the gun and to where the pressure measurement devices is placed), neutral silicon plume becomes wide and flat and remains near the target surface, leading to low quality films[138]. On the contrary the ionized atoms plume expands with higher velocity at higher pressure[139]. This is thought to be due to the better space charge neutralization by the background gas.

Also, we must underline how the gas species influence the plume. A clear difference is observed when Si is ablated in argon or in nitrogen environment. Ablation in Ar gives rise to a very quicker plume. This is due to more effective ablation, as a consequence of differences in the channel formation.

When the electron beam stops also the ablation finishes and the plume formation is stopped. The process continues by the compensation of pressure and temperature between the plasma (the plume) and its surrounding gas. Since the plasma lifetime is long, the plasma gets positively charged. Also the target is positively charged, so unipolar arc discharge are formed between the plasma, the target, the target holder (possibly), the anode (the deposition chamber)[140]. Because of

[135] S.D. Kovaleski, R.M. Gilgenbach, L.K. Ang, Y.Y. Lau, J.S. Lash, Appl. Surf. Sci. 1998, **127**, 947.
[136] S.D. Kovaleski, R.M. Gilgenbach, L.K. Ang, Y.Y. Lau, J. Appl. Phys. 1999, **86**, 7129.
[137] Th. Witke, A. Lenk, B. Schultrich, C. Schultheiss, Surf. Coat. Tech. 1995, **74**, 580; T. Witke, A. Lenk, B. Schultrich, IEEE Trans. Plasma Sci. 1996, **24**, 61.
[138] S.D. Kovaleski, R.M. Gilgenbach, L.K. Ang, Y.Y. Lau, Appl. Phys. Lett. 1998, **73**, 2576.
[139] S.D. Kovaleski, R.M. Gilgenbach, L.K. Ang, Y.Y. Lau, J. Appl. Phys. 1999, **86**, 7129.
[140] T. Witke, A. Lenk and P. Siemroth, IEEE Trans. Plasma Sci. 1997, **25**, 758; T. Witke, A. Lenk, B. Schultrich, C. Schultheiss, Surf. Coat. Tech. 1995, **74**, 580; T. Witke, A. Lenk, B. Schultrich, IEEE Trans. Plasma Sci. 1996, **24**, 61; S.D. Kovaleski, R.M. Gilgenbach, L.K. Ang, Y.Y. Lau, Appl. Phys. Lett. 1998, **73**, 2576.

the unipolar arcs the plasma begins to be unstable, target material is emitted from the erosion areas of the arcs on the target surface for a time which is much longer than the pulse duration[141]. So clusters and particulate leave the target and deposit on the film. Particulate percentage and size slightly decrease by decreasing the voltage, possibly because the softener ablation[142]. Also the target to substrate distance play a determinant role: larger distances cause lower deposition rates and a loss of stoichiometry, while at a shorter distance a back sputtering can happen.

Figure 11: LSMO ablation photo.

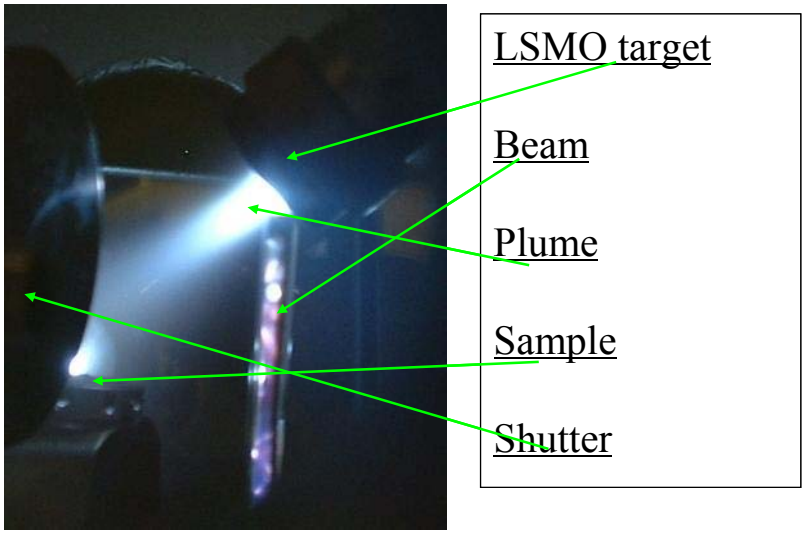

Atomic Force Microscopy

Atomic Force Microscopy is a surface imaging technique. It is based on the scan of the sample surface by a tip placed on a cantilever. A laser is reflected on the cantilever surface and measures the mechanical behavior of the cantilever and, as a consequence, of the tip. Two basically AFM concepts exist: static AFM, where the tip scans the surface touching it, and dynamic AFM, where the cantilever vibrates and the oscillation parameters are detected. Only the second was used for this thesis, so it will be the only one described.

The cantilever oscillates and the amplitude, the frequency, the phase of the oscillation link the cantilever vibration dynamic to the tip-surface interaction. According to the parameter used as feed-back different techniques and different operation conditions are tuned. In Amplitude Mode

[141] T. Witke 1995, cited.
[142] S.D. Kovaleski, R.M. Gilgenbach, L.K. Ang, Y.Y. Lau, J. Appl. Phys. 1999, **86**, 7129.

AFM (AM-AFM or tapping mode AFM), the cantilever oscillates at fixed frequency, near the resonance, the tip "taps" at the surface touching it and leading to a relevant interaction which alters the oscillation amplitude, which is the detected parameter. A change in the tip-surface distance affects the amplitude oscillation. The piezoelectric actuator moves to restore the previous amplitude: a three-dimensional map of the surface is realized, where the x and y are the scan direction and z is the piezotube elongation, which reflects the topographical features. AM-AFM is the most used configuration, but it does not permit atomic resolution and its implementation in UHV is not possible: too long time needed for a reliable amplitude measurements due to the very high quality factor in vacuum[143]. In UHV the Frequency Modulated AFM (FM-AFM or non contact, NC-AFM) is used. At constant amplitude, the change in frequency is detected. While in the AM-AFM there is a contact between the tip and the surface, in the FM-AFM there is not any contact. This technique gives atomic resolution.

When the feedback loop keeps constant the amplitude and the frequency, the phase lag relative to the excitation signal is monitored. Since the phase shift is linked to the surface stiffness, its detection provides high material sensitivity. The phase detection during the AM-AFM, without the constant amplitude requirement, gives a clear imaging of the morphological features without the height information: we can perceive the phase as the spatial derivative of the oscillation amplitude.

In the following a brief description of the AM-AFM technique will be done, since it is the mode used in the presented thesis. In the tapping mode AFM the dominant tip surface interaction is of the long range van der Waals type. It is due to the macroscopic sizes of the two elements, tip and surface, and not to the direct interaction between the tip atoms closer to the surface, described by Lennard-Jones potential, which "works" in the FM-AFM. In standard atmosphere conditions, as used during the presented activity, a thin film of water is absorbed on the surface. The meniscus bridges tip and sample and implies an additional attractive force. Both the last capillar force and the vdW interaction depend monotonically from the tip-surface distance and should not invalidate the measurement results.

A bistability of the oscillation state has been found, with two different amplitude (low and high), to which a different tip-surface interaction strength corresponds. What state is chosen by the system depends on the initial conditions. For example, initially the tip oscillates in the low amplitude state, but reducing the tip surface distance a transition to the high mode occurs, since with the distance the tip-surface interaction changes. If the shift happens during an experiment,

[143] R. Garcìa, R. Pérez, Surf. Sci. Rep. 2002, **47**, 197.

one can try to change the driving force or set point parameters. If it is not enough, the tip must be raised and approached again. Fringes in the image around the objects contour or surrounding the topographical features are the signature of jumps between amplitude modes[144] and a bad tip interaction during the imaging.

Finally we mention the question about the resolution. The main source of noise affecting the vertical resolution is the thermal noise of the cantilever which can be expressed by: $\sqrt{\frac{4k_BT}{3k}} = \frac{0{,}074nm}{\sqrt{k}}$ [145] , at room temperature, for k expressed in N/m. So for a force constant of 35N/m the thermal noise fluctuations is only about 0,01nm, and for a constant of 3N/m it becomes 0,04nm. Thermal noise fluctuations are very small in respect to the vertical scales analyzed in the presented work. The more relevant source of uncertainty in the vertical resolution comes from the physical interaction between the tip and the surface in the two amplitude mode, which can provide irreversible changes in the measured height, even on metal nanoparticles. This effect is more relevant for relatively soft object on hard surfaces[146]. From the other hand the finite tip size is responsible for the broadening effects of the boundaries of the objects. Small tip-surface interaction (low mode amplitude branch) increase the lateral resolution.

During the AFM measurement the scanning tip induces a convolution and a deformation. Convolution is mainly a geometrical effect depending on the shape of the surface features and of the tip, while deformation depends on the strength of the interaction forces and surface hardness. While the vertical resolution is not affected by convolution, the lateral resolution is afflicted by both of them. Operating in low amplitude mode gives better results in respect of either convolution and deformation. As the operating state depends on the initial approaching conditions and statistical fluctuations, a perfect formula granting the success is not achievable.

About the cantilever choice, a general consideration is that more the force constant more the force exercised on the surface (and the possible damages) and the resolution, less the noise and the lateral force effects and distortions.

[144] See fig.ure 11, page 216, of the reference in Garcìa and Pérez, *cited*.
[145] H.J. Butt, M. Jashke, Nanotechnology 1995, **6**, 1.
[146] P. Nemes-Incze, Z. Osvàth, K. Kamaràs, L.P. Birò, Carbon 2007, **45**, 3022.

Scanning Tunneling Microscopy

In the Scanning Tunneling Microscopy (STM) a nano-sharp metallic tip scans the sample surface; STM measurements are usually carried on in UHV. A tunneling current is established between the sample and the surface by bringing the tip close to the surface (a few angstroms) and applying a potential difference between the tip the sample, which is grounded. The system surface/vacuum/tip is a tunnel junction, where the established tunneling current is $I_{(z,V)} \sim C\, e^{-k\, z}$ where z is the tip surface distance and k and C are constants.

Let us suppose the tip scan on the sample surface, keeping the bias V constant. The tip moves on the surface while the distance z is varied in order to keep the current constant at a given value, set by the operator. During the scanning, the current is monitored by a feedback loop, which generates an electrical signal which drives the vertical movement of the tip by a piezoelectric element. The voltage signal due to the feedback loop is registered and its profile correspond to the height of the tip during the scanning line; in this manner by scanning a whole area line by line, it is possible to obtain a topographic image of the surface. This is called constant current mode.

The constant C of the tunneling current expression contains information on the convolution of the density of states (DOS) of the tip and surface. So, provided the DOS of the tip, a spectroscopy of the sample surface DOS can be performed. But this also means that the DOS of the sample and the tip enter in the topographical data. Thus STM measurements require an extreme care, but provide much more reliable information with respect to the tapping mode AFM. In the presented work STM is applied to LSMO surface[147].

[147] Two reviews on the topic of STM investigations of oxide surfaces are: N. Nilius, Surf. Sci. Rep. 2009, **64**, 595; and D.A. Bonnel, Progr. Surf. Sci. 1998, **57**, 187.

Other experimental techniques

This paragraph presents techniques not directly used by the author but operated in collaboration with other groups. Several characterization tools have been used in addition to AFM, albeit not performed by the author, and the results have been widely considered. A brief, conceptual, explanation of them seems necessary.

Impedance spectroscopy

Impedance is a measure of opposition to time-varying electric current in an electric circuit. The impedance **Z** is defined as the ratio between the applied voltage and the measured current. Unless the system is purely resistive, the current will have a different phase from the applied voltage: $\mathbf{Z} = \frac{\mathbf{V}_0}{\mathbf{I}_0} \frac{\cos(\omega\, t)}{\cos(\omega\, t - \varphi)}$; using the complex notation: $\mathbf{Z} = \mathbf{Z_0}\,(\cos\phi + i\,\mathrm{sen}\phi) = \mathbf{R} + i\chi$.

Usually one measures real and imaginary parts of the complex impedance by varying the excitation frequency ω. The plot of –Im[**Z**] versus Re[**Z**] at fixed frequency is called Nyquist plot.

The essence of the impedance measurement is the fitting with electric elements (resistors, capacitors, inductor) combined in series or in parallel, which of them owns a physical meaning, in order to know device materials properties. Typically in organic devices a parallel RC circuit is used to simulate the organic semiconductor (OS) film and fit the impedance data. The resistance accounts for the low conductance of the OS while the capacitance for its charging and polarization effects.

X-ray reflectivity

This techniques relies on two wave concepts: reflection and interference. The refractive index is a complex quantity whose values depend on the radiation wave length. For X-ray it is $n=1-\delta-i\beta$ and depends on the radiation wave length, the electron density of the material and its atomic weight. Since the Re[n] < 1 the total reflection of grazing radiation under a certain critical angle is possible. At higher angles some X-photons are reflected, others penetrate in the material and can be reflected from the bottom interface and then coming out from the surface, as sketched in Figure 12. When the photons reflected from the bottom interface exit from the surface (*refracted photons*), they interact with those photons which were reflected directly from the surface (*reflected photons*): interference occurs. The interaction leads to a stronger radiation, or to its annihilation, according to the difference in the optical paths: if the reflected and refracted

photons electric fields oscillate in phase, the radiation intensity will increase, differently it will decrease. Since the optical path difference depends on the angle, interference fringes are recorded, according to the incidence angle. The formula in Figure 12 describes the fringes spacing. When we have a multilayer, this effect repeats for every interface (Figure 12, right).

Figure 12: X-ray reflectivity scheme for single and multilayered film.

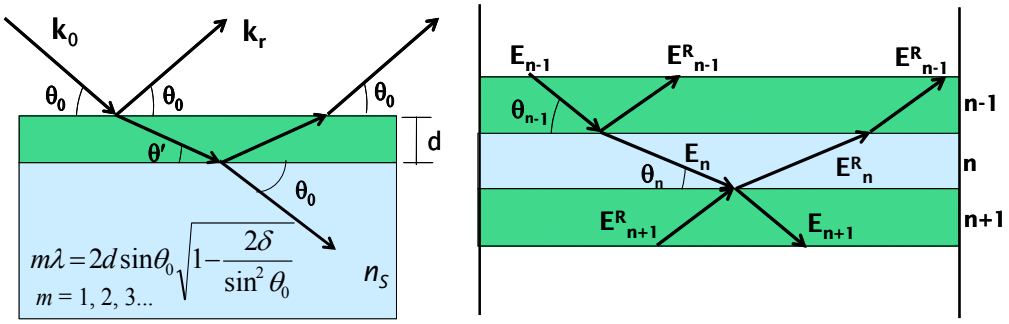

Once the reflectivity spectra is recorded, the iterative fitting procedure shall be applied[148]. The boundary condition states that the reflectivity at the bottom interface (the bottom side of the substrate) is zero, the continuity of the tangent components of the electric and magnetic field is imposed at each interface, and for each layer the absorption is considered, where the only free parameter is the layer thickness. By computing the reflectivity for each interface, from bottom to top, one arrives to the surface and obtains the simulated spectrum which is compared with the experimental one and the thickness data are varied up to the accepted agreement.

These concepts allow to study also buried interfaces. Each interface is approximated by several layers with an intermediate refractive index which shifts gradually from one material to the other. It is a sort of electron density profile. From the fitting procedure it is possible to extract the thickness of each layer and the width of each interface, expressed as the total amount of intermediate refractive index between the two layers: The broadened region defines the interface width or intermixing. The method provides an averaged characterization and not a local probe like AFM or TEM.

TEM

Transmission Electron Microscopy (TEM) is a widely and powerful technique for the structural analysis of a sample and of an interface. In principle TEM exploits the contrast raising from the different behavior of samples region in respect to the incoming electrons. These are generated by thermionic emission of a filament, accelerated by an electric field and focused by

[148] L.G. Parratt, Phys. Rev. B, 1954, **95**, 359.

magnetic lenses. Then they hit the sample, which has to be carefully prepared. The sample thickness should be comparable to the mean free path of the electrons travelling through it. Such thin layers can be produced by Focused Ion Beam (FIB). Electrons interact according to the atomic number, so heavy elements will give more scattering, and hence higher contrast. Thicker region, or region with higher atomic number, cause more absorption and appear dark, while thinner zones or light elements are bright. Since the brightness is due to electron travelling without being absorbed, this contrast is called *bright field*. TEM also exploits the electron diffraction by the crystalline lattices. It is used to observe the atomic structure of the material and to observe defects like stacking faults or dislocations.

An accurate operation mode is the measurement of the phase contrast of the diffracted electron waves. The highest resolution is achieved, and the Fourier transform of the image provides a direct view of the atoms with a resolution less than one angstrom. It is named *High Resolution Transmission Electron Microscopy*, HRTEM.

It appears that TEM is a powerful technique for the local imaging of the interfaces. Moreover a chemical tool can be added for the interface analysis: the *Electron Energy Loss Spectrometry* (EELS). The inelastic scattering encountered by the electron is measured. Because it depends on the elemental properties, when EELS is performed along a line across the interface, it provides a measurement of the elemental distributions.

XPS and UPS

Photoemission techniques rely on the optical properties of a material. When the material is irradiated by an electromagnetic wave, it can absorb it and the system will be excited. If the radiation energy is high enough, the electron leaves the surface and is detected. By varying the energy range of the photons, the binding energy of the electronic levels involved in the bonds (Ultraviolet Photoemission Spectroscopy-UPS) or those of the core levels (X-ray Photoemission Spectroscopy-XPS) are measured. The energy of the detected electron (E_k) is the difference between the incident photon ($h\nu$) and the binding (E_B) energies.

UPS is used to investigate the band structure of a material, the electronic levels involved in the chemical bonds. The incident photon are monochromatized and are spanned over a certain energy range. So one measures the valence band of the metal. The maximum E_k corresponds to the minimum E_B, which is the Fermi level (FL), and provides a measure of the work function $\phi_M = h\nu - E_k^{\max}$. In contrast, the minimum E_k is related to the maximum E_B and gives the position of the vacuum level (VL).

When something, e.g. an organic molecule layer, is deposited on top of the metal, both the previously defined quantities shift. The highest energetic electron shifts to lower value: this is perceived as the onset of the HOMO level of the organic material and provides the difference between the FL of the metal and the HOMO level of the organics. Also the minimum E_k decreases, as a consequence of a shift in the vacuum level due to the formation of an interface dipole[149].

Figure 13: Photoemission spectroscopy principles for bare metal and organic on metal systems; from 149.

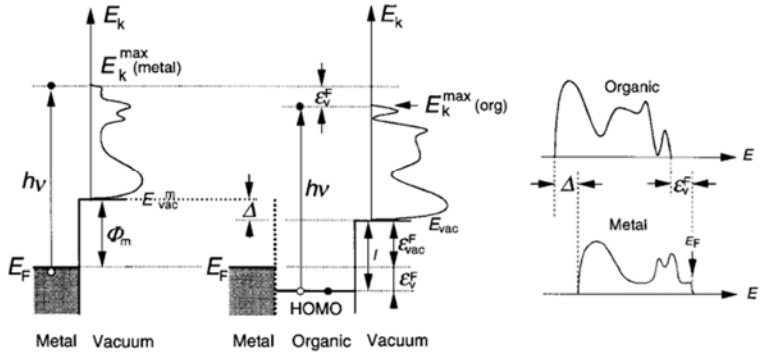

XPS works in the same manner, but usually involves transitions from the core levels. So selected atomic core level, not involved in the bond formation, are explored. The binding energy for the electrons in these levels is measured. A change in it, or the formation of additional peaks (shoulders in a real slightly broadened spectrum, where closed peaks are convoluted) is thought to be due to a change in the element chemistry: a difference coordination number or the rupture of a bond and the formation of a new one.

Magnetometry

Four techniques have been used during the presented PhD thesis to probe the magnetic properties of the films: X-ray Magnetic Circular Dichroism (XMCD), Magneto-Optic Kerr Rotation (MOKE), Superconducting Quantum Interference Device (SQUID) and Nuclear Magnetic Resonance.

XMCD is the differential absorption spectra of x-ray left and right circularly polarized light in the presence of a magnetic field. Ferromagnetic materials have an imbalance in the populations of spin up and spin down electrons, and so an imbalance in the empty states of the two spin orientations; spin moment is magnetic in nature. From the other side the magnetic field of circularly polarized light oscillates along a precise direction. Thus when the electrons of a

[149] H.Ishii, K. Sugiyama, E. Ito, K. Seki, Adv. Mat. 1999, **11**, 605.

ferromagnetic material interact with polarized light, the interaction will depend on the light polarization and the difference between the absorption spectra (the XMCD spectrum) contains information on the spin population imbalance.

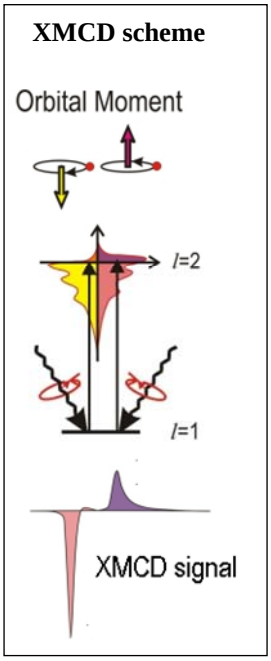

MOKE effects is based on the rotation of the polarization plane of light after the reflection from the surface of a ferromagnetic material. It is related to the change of the refractive indices for the two polarization components, a consequence of the modification of the electron wave function due to the spin-orbit interaction[150]. If the material is not ferromagnetic, a light purely polarized in the plane of incidence (the one formed between the light incidence direction and the normal to surface) would keep its polarization, but in a ferromagnetic materials the reflected beam will have a component perpendicular to the incidence plane. In the figure the set up of the laboratory in Bologna is sketched. A laser is used as source of polarized light, but a polarizer is added to ensure the polarization.

Figure 14: MOKE set-up at the ISMN-CNR-Bologna.

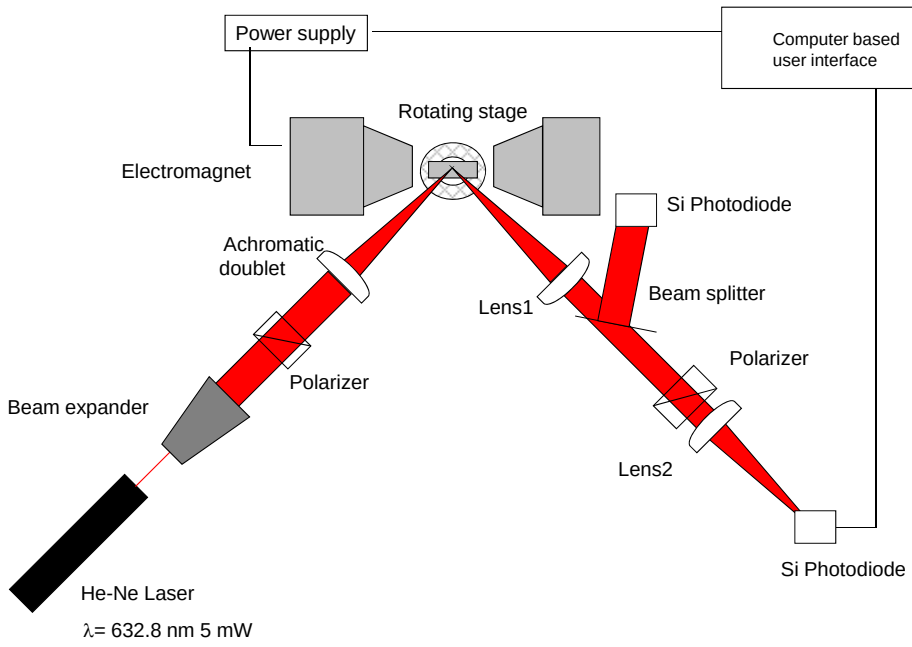

The Kerr rotation is the real part of the ratio $E_{\perp}/E_{//}=\phi'+i\phi''$, where $E_{//}$, and $E_{\perp}$ are the parallel and perpendicular polarized components of the electric field polarized in respect of the incidence plane. The analyzer is placed at a small, known, angle in respect to the parallel polarization and ϕ' is detected. Alternatively, for samples with very weak Kerr rotation, the Kerr

[150] Z.Q. Qui, S.D. Bader, Rev. Sci. Instrum. 2000, **71**, 1243.

ellipticity ϕ'' can be measured by inserting, before the analyzer, a quarter-wave filter which produce a $\pi/2$ phase difference so that $E_{\perp} / E_{//} = -\phi'' + i\phi'$. Since ϕ' and ϕ'' are linearly proportional to the magnetization, the Kerr rotation or ellipticity measured as a function of the magnetic field yields the hysteresis loop.

NMR exploits the behavior of atomic nuclear owning non-zero overall spin moment *I*, in respect to a magnetic field. A nucleus of spin *I* in a magnetic field has $2I+1$ possible orientations. To each orientation corresponds an energy level; without an external magnetic field, the orientations have equal energy.

By applying a magnetic field, the energy levels split. It is possible to excite these nuclei into the higher level state with electromagnetic radiation. The frequency of electromagnetic radiation needed is determined by the difference in energy between the levels.

Magnetoresistance

The magnetoresistance of devices is measured in the cross bar, four point, configuration, depicted in Figure 15a. The effect of the extended resistive electrodes, in particular LSMO, is supposed to be ruled out. The resistance R is assumed to be the ratio between the applied voltage and the measured current and is plotted versus the magnetic field providing the R(**H**) (magnetoresistance) curve.

The overall device resistance depends on the relative orientation of the magnetization of the electrodes. The spin polarized current is injected from one electrode into the OS, in which transport occurs, until carriers reach the other electrode. The magnetization of the electrodes is manipulated by the application of an in plane external magnetic field, which normally is parallel to either electrode. The resistance between the electrodes changes depending on the relative orientation of their magnetizations. Figure 15b shows the resistance starting from a high positive field, which is swept past 0 to reach a high negative field. The arrows at the bottom of the figure show the orientation of the magnetization of the electrodes. Figure 15c shows the MR when the field is swept starting from a high negative magnetic field, and Figure 15d shows the complete measurement.

Figure 15: four points scheme for spin valve measurements

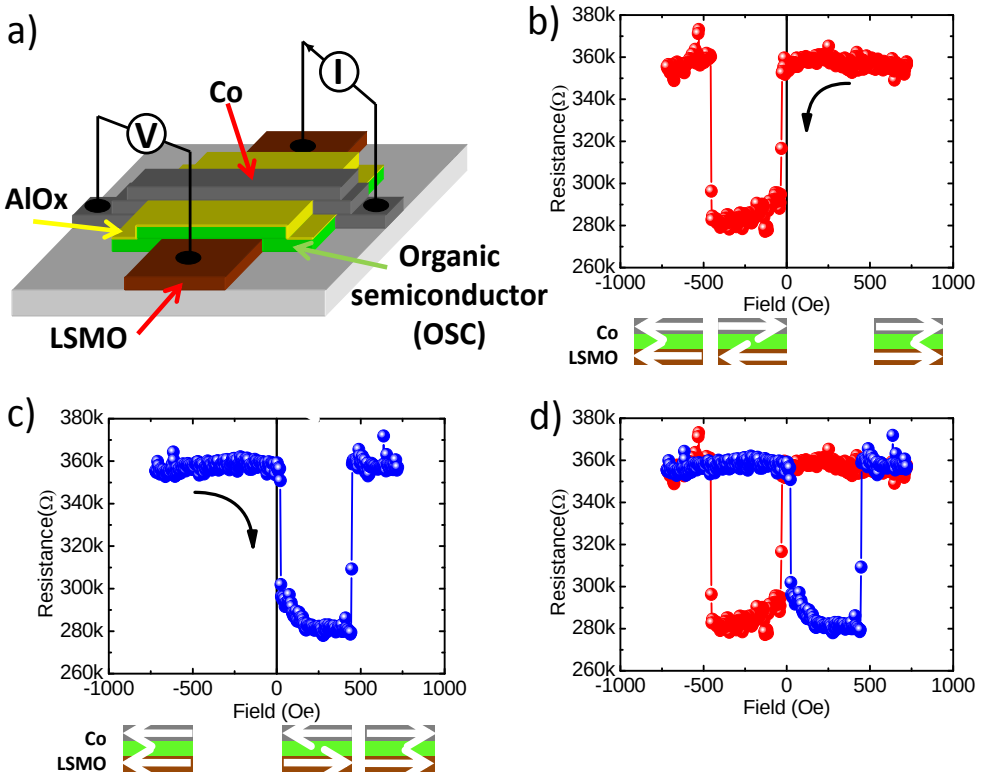

3. Experimental results

The bottom electrode: LSMO thin films

$La_{0,7}Sr_{0,3}MnO_3$

Rare-earth manganese perovskites feature Colossal Magnetoresistance (CMR), a peculiar magneto-electronic behavior due to the interplay between magnetic ordering and transport properties. CMR materials are promising for spin based devices such as magnetic field-sensors, reading-heads, magnetic field driven switches, et cetera. For most applications manganites should be prepared in the form of thin films[151]. The perovskite unit cell formula is ABO_3, where A is a large radius cation, B is small radius cation, O is oxygen. The mean cation size is often crucial for the magnetic and electric behavior [152]. Perovskite materials can be imagined as alternated parallel layers of AO and BO_2 planes where the crystal ***c*** axis is perpendicular to the layers. So an intrinsic structural anisotropy is present also in cubic perovskites.

$La_{1-x}Sr_xMnO_3$ (LSMO) is a ferromagnetic material for $0,2 < x < 0,5$ with 100% spin polarized carriers at $T << T_C$[153] (*half-metal*). The highest Curie temperature in the CMR manganites class is obtained for x=0,3 [154]. The crystalline structure is rombohedral[155], with the lattice parameter of 5,48 Å and the angle between the ***ab*** plane and the ***c*** axis (labeled α) of 60,35 °, but the pseudo-cubic conventional cell is often used, with the lattice parameter of 3,87 Å, in order to better visualize the symmetry properties of the lattice (specially in the epitaxial mismatch estimation) and the La(Sr)O and MnO_2 planes stacks. The Curie temperature is around 370 K in bulk samples, while thin films have Tc about 330-350 K, varying with thickness and deposition method. The carrier hopping between Mn^{3+} and Mn^{4+} ions is governed by a strong on site Hund interaction (nearly 1eV), which makes LSMO an unusual metal, characterized by a narrow band (~1-2 eV) and small (if compared with metals) carrier density (10^{21}-10^{22} cm^{-3}), similar to high temperature cuprate superconductors and some organic metals. Above T_C it is a paramagnetic

[151] A.-M. Haghiri-Gosnet, J.-P. Renard, J. Phys. D: Appl, Phys. 2003, **36**, R127; M. Bowen, J.-L. Maurice, A. Bartheélémy, M. Bibes, D. Imhoff, V. Bellini, R. Bertacco, D. Wortmann, P. Seneor, E. Jacquet, A. Vaurès, J. Humbert, J.-P. Conotur, C. Colliex, S. Blugel, P.H. Dederichs, J. Phys.: Cond. Matt. 2007, **19**, 315208.
[152] A.M. Haghiri-Gosnet, J.P. Renard, J. of Phys. D: Appl. Phys.2003, **36** R127.
[153] J.H. Park,E. Vescovo,H.J. Kim, C. Kwon, R. Ramesh, T.Venkatesan, Nature 1998, **392,** 794.
[154] W. Prellier, Ph. Lecoeur, B. Mercey, J. Phys. Cond. Matt. 2001, **13**, R915.
[155] A. Urushibara, Y. Moritomo, T. Arima, A. Asamitsu, G. Kido, Y. Tokura, Phys. Rev. B 1995, **51**, 14103.

metal or insulator according to the composition. The compound with x=0,3 is insulator.

Magnetoresistance (MR) is defined as $MR = \frac{R_B - R_0}{R_0}$, where R_B is the resistance at the applied magnetic field and R_0 is the resistance without the applied magnetic field. MR has a maximum near-below T_C, we refer to this temperature as T*. The metal-insulator transition temperature (T_{MI}) is approximately given by the maximum in the R(T) curve: increasing temperature in the ferromagnetic metallic region the resistance increases (it is a metal), then it decreases (it is a semiconductor). At this point the distinction between spin up and spin down band is lost and the material becomes insulating-like. Figure 16 sketches the half metallic manganite bands as derived from the manganese and oxygen orbitals. The spin up and spin down bands are represented at left and right side respectively. The Fermi level position is so that only one spin population contributes to the conduction.

Figure 16: LSMO band structure

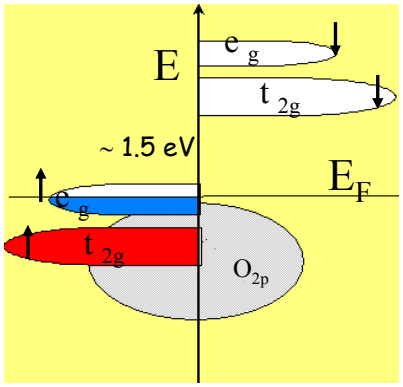

Spin polarized injection in organic semiconductor sexithiophene by means of LSMO electrodes[156] was achieved in 2002 and giant magnetoresistance values were found in Alq_3 based devices with an LSMO electrode[157]. So LSMO applications extended towards the organic spintronics field. Since most of these devices feature vertical structure, the LSMO layer surface is thought to play a decisive role. The integration of manganite thin films in heterostructures requires good control of interfaces and surface properties in order to properly tune the device performances.

[156] V. Dediu, M. Murgia, F.C. Matacotta, C. Taliani, S. Barbanera. Solid State Commu. 2002,. **122**, 181.
[157] Z.H. Xiong, D. Wu, Z.V. Vardeny, J. Shi, Nature 2004, **427**, 821.

LSMO thin films optimization

Channel Spark Ablation (CSA), an elegant alternative to the more complicated and costly laser ablation technique[158] seems to be an interesting technique for complex oxides thin films deposition[159]. One of the drawbacks of CSA (similarly, in principle, to PLD) is the formation of outgrowths[160], and their presence as well as the presence of droplet-like defects is clearly related to the strength of the ablation[161]. The optimization of the deposition of LSMO on STO (100) and NGO (110) substrates by CSA led so far to optimal magnetic and transport properties[162] while the morphology featured a exceedingly high roughness which could be estimated approximately as 10-20% of the film thickness. These parameters, while in principle acceptable for vertical devices with thick enough organic layers, prevented considerably the fabrication of high quality devices and especially the understanding of thickness dependence of organic based spintronic devices.

During the present PhD thesis the author has succeeded in the deposition of smooth (root mean square roughness lower than an unit cell) LSMO thin films with excellent magnetotransport properties and surface ferromagnetism above room temperature. The author succeeded to identify the working gas pressure during CSA process as a key factor in order to reduce the roughness, the granularity of the films and the outgrowths formation.

Moreover the growth mode is recognized to be characterized by a transition from flat towards three-dimensional structures and the relevant mechanism appears to be the Ehrlich-Schwoebel barrier which confine the atomic units in the terrace.

LSMO films in the thickness range of 8-40 nm were deposited on matching insulating substrates ($NdGaO_3$, $SrTiO_3$) at a substrate temperature about 890 °C. Films morphology was analyzed by means of atomic force microscopy (AFM), the magnetotransport behavior was characterized by measuring the films resistance and magnetoresistance. Finally XMCD measurements were performed at 90 K and at room temperature (RT) in order to provide evidence of the surface magnetism, which is of special interest in devices.

---

[158] G. Muller and others, in *Science and Technology of Thin Films*, edited by C. Matacotta and G. Ottaviani, published by Scientific Singapore Publishing Co. Pte. Ltd. 1995.
[159] Dediu_PSSB, A. Kursumovic, P. Berghuis, V. Dediu, J. E. Evetts, F. C. Matacotta, G. A. Wagner, Physica C 2000, **331,** 185;
[160] F. Biscarini, V.I. Dediu, O. Greco, F.C. Matacotta A. Migliori, Nuovo Cimento 1997, **19D**, 1003; R. Bertacco, A. Tagliaferri, M. Riva, L. Signorini, M. Cantoni, F. Ciccacci, B.A. Davidson, F. Maccherozzi, I. Vobornik, G. Panaccione, Phys. Rev. B 2008, **78**, 035448-
[161] J.E. Mathis, H.M. Christen, Physica C 2007 , **459**, 47 .
[162] I**.** Bergenti, A. Riminucci, E. Arisi, L.E. Hueso, M. Cavallini, M. Solzi , V. Dediu, J. Magn. Magn. Mater. 2007, **310**, e780.

Figure 17: LSMO bulk pseudo cubic structure (top) and STO and NGO substrates structures with the used orientation, substrate plane termination and lattice mismatches. In LMSO Sr substitutes La, in STO and NGO sketches the oxygen atoms are not shown.

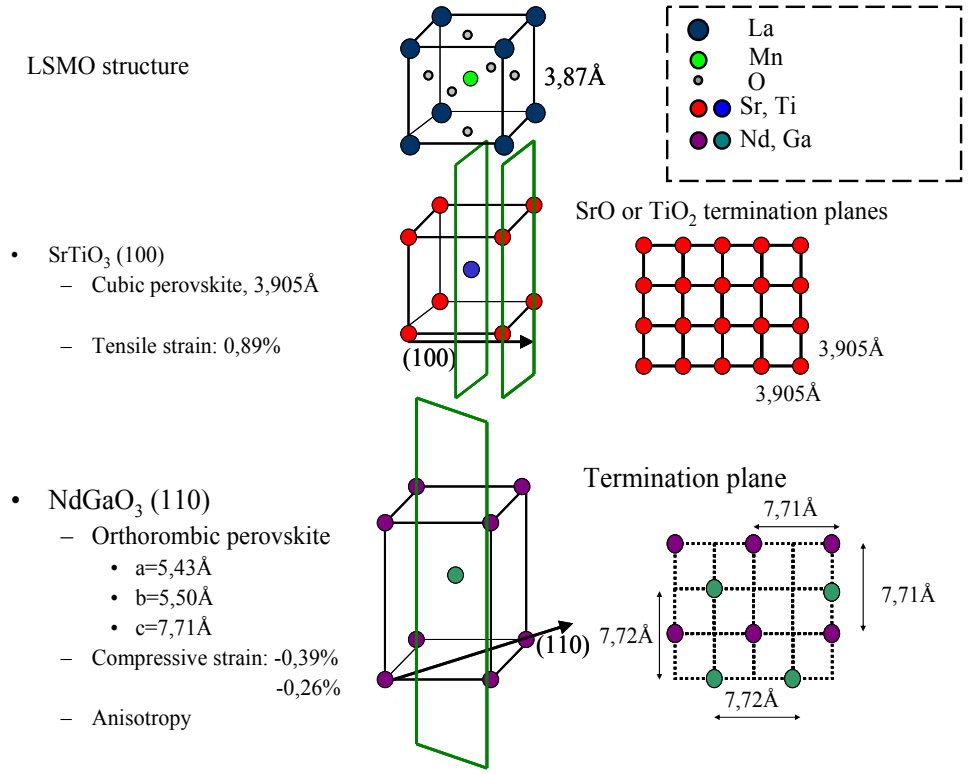

Figure 18: LSMO thin film deposited following the protocol at the ISMN-CNR in Bologna at the beginning of the present PhD thesis.

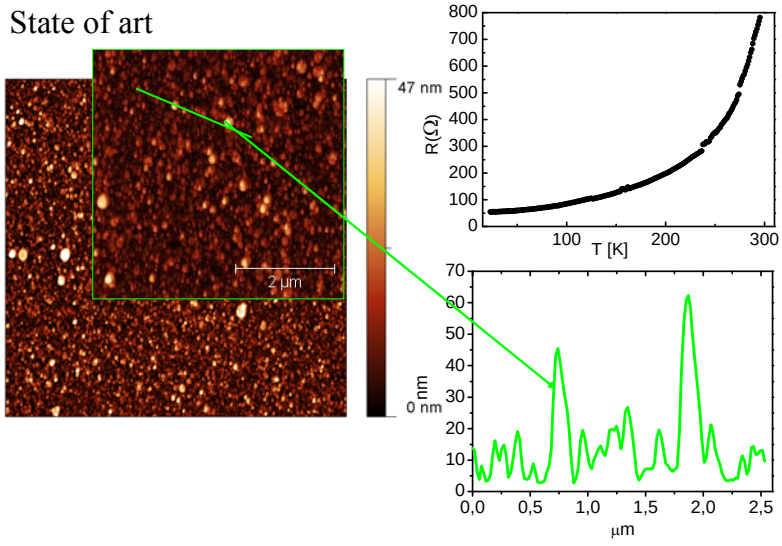

The LMSO structure is depicted in Figure 17. In the same figure also the used substrate crystal structure and the cut direction are shown. The $SrTiO_3$ (STO is a cubic perovskite, and the

termination plane perpendicular to the <100> direction (the (100) planes family) is a layer of SrO or TiO_2 with a square cell. Differently, $NdGaO_3$ (NGO) cut perpendicular to the <110> direction has termination planes with anisotropy along two perpendicular direction. It comes out that epitaxial LSMO films will show in-plane anisotropy when deposited on NGO, while they are isotropic when deposited onto STO.

Figure 18 summarizes the LSMO thin film deposition state of art of the laboratory where the thesis has been performed, for a 40 nm thick film. The deposition pressure was $2{,}0 \cdot 10^{-2}$ mbar and the voltage 8,5 KV. The very good magnetotransport and magnetic (not reported) properties are "afflicted" by a quite rough surface with 20-30 nm high structures plus 70-100 nm high outgrowths.

From the analysis of the channel spark process described in the section on the experimental techniques, it was decided to try improving the film morphology via increasing the pressure while keeping the voltage constant. Figure 19 presents the first results on 10 nm thick films deposited on STO and on NGO. One can observe immediately the very low roughness which confirms that the pressure is a relevant parameter. Moreover the X-ray circular Magnetic Dichroism (XMCD) performed at the Linköping University by YiQiang Zhan and Fenghong Li shows that the films surfaces are ferromagnetic up to room temperature. The morphology of the film grown on STO and on NGO appears very different. In particular the larger structure on NGO could be due to the better lattice matching and minor interfacial strain.

Figure 19: 10nm thick LMSO film deposited on STO and on NGO, XMCD reveals RT surface magnetism.

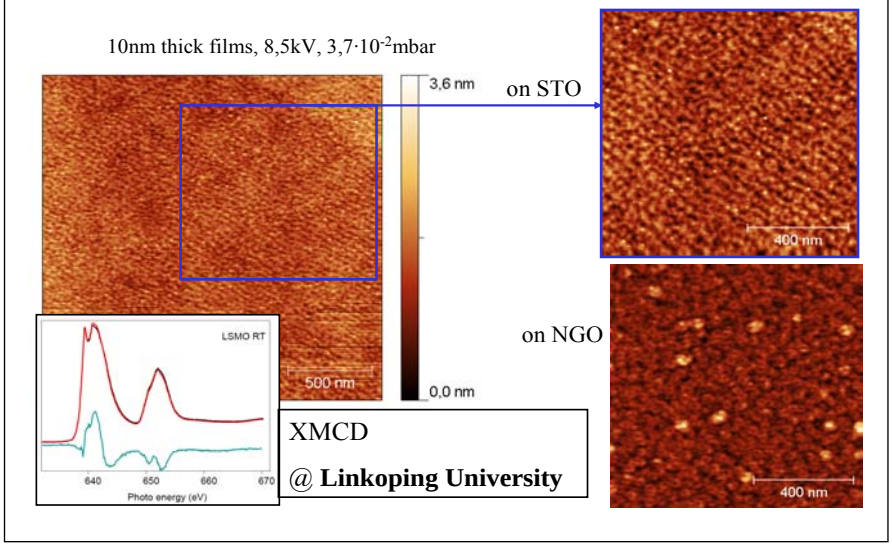

Figure 20: topography, resistance without magnetic field R(0) and magnetoresistance (MR), for 10 nm thick films; the colour of the AFM boundaries identify the magnetotransport curves. The green curve refers to a 40 nm thick film grown at 2,2·10^{-2}mbar (AFM in Figure 19).

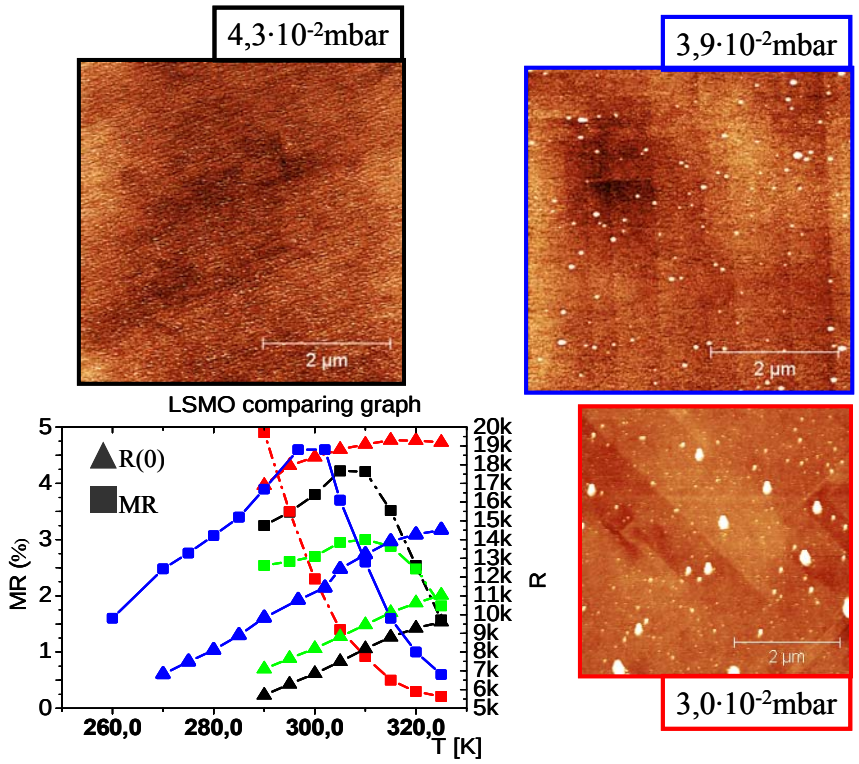

This important result led to experiments dedicated to gain more insight into the epitaxial growth of the LSMO. First, the pressure role was studied, the accelerating voltage was kept at 8,5 KV and the chosen substrate was STO. Figure 20 reports AFM and magnetotransport measurements (performed by Dr. Mirko Prezioso) for 10 nm thick films, in the temperature range around 300 K. In the same graph it is also reported the measure of a sample grown at 2,2·10^{-2} mbar (green) whose surface has been reported in Figure 18. The MR was detected by measuring the resistance as a function of the magnetic field in the range ±2880 Oe (±361mT). Two R(H) curves measured for the film deposited in 3,9·10^{-2} mbar, at 270 K (ferromagnetic and metallic region) and at 320 K (between T* and T_{MI}) are shown in Figure 21. The magnetic field decreases the resistance by aligning the magnetic domains also above T* (T* < T_C); 320 K is under T_{MI}. The amount of MR at T<T* in LSMO thin films is due also to structural imperfections such as magnetic inhomogeneities and grain boundaries. In the ferromagnetic region, far below T_C, the spins should be all aligned and the magnetic field influence should be very low: applying the field the change is very little. The shape of R(H) gives information on these defects[163]. From the linear shape of the R(H) measurements in the ferromagnetic region (Figure 21, left) we know that our

[163] K. Dörr, J. Phys. D.: Appl. Phys. 2006, **39**, R125, especially the paragraph 6.

films are not affected by grain boundaries transport. The broadening of the R(H) at T > T* (Figure 21, right) is due to the lost of a proper ferromagnetism and to the presence of paramagnetic regions whose shape and size change with the application of the field in a not regular way: $T^* < 320\ K < T_{MI}$.

Figure 21: R(H) for the film grown at $3{,}9 \cdot 10^{-2}$ mbar below and above T* (left and right rispectively).

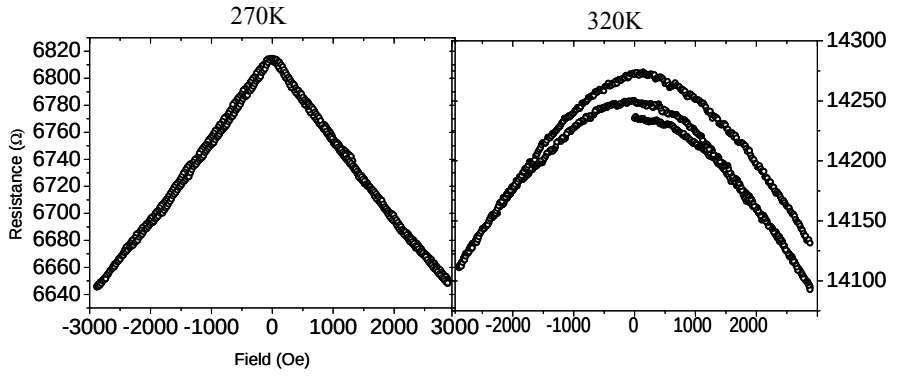

The pressure acts mainly in the reduction of the outgrowths, while the flat regions between the outgrowths have a mean peak to valley roughness of about 1nm achieving a maximum roughness of a few nanometers. Note that the film grown at $4{,}3 \cdot 10^{-2}$mbar presents completely clean 5 μm x 5 μm areas. Furthermore the T* seems to increase (the peak in the MR(T)) up to 315 K for this film while the T_{MI} is above 330 K. The film deposited at the old conditions features comparable properties against a higher thickness (40 nm) and very rough surface (Figure 18).

Then the substrate effect was explored, firstly by AFM (these images were taken by Dr. Catherine Kitts), and then by transport measurements. The aim of these measurements was not only to observe the change of substrate but also to explore the voltage dependence of the morphology. Figure 22 presents the data. In the samples deposited at lower voltage (6,7 and 7,5 KV) outgrowths are not present, but some lower mounds are observed, whose density decreases with the voltage. Increasing the voltage and the pressure (which is lower than the optimal one), the mounds density is decreased but a few outgrowth are still present. Moreover the surface is rougher. Thus the speculation that an increasing in pressure leads to a decreased outgrowths and mounds density is true. A higher voltage leads to rougher surface, but comparing the mounds density of the films at 6,7 and 7,5 KV an optimal voltage seems also to exist, possibly due to ablation efficiency constrain. Transport measurements are necessary to clarify deeper these aspects and are reported below, on films deposited at the pressure of $4{,}1 \cdot 10^{-2}$ mbar, by varying the voltage.

Figure 22: AFM of three LSMO on NGO films deposited at the conditions reported on each images couple.

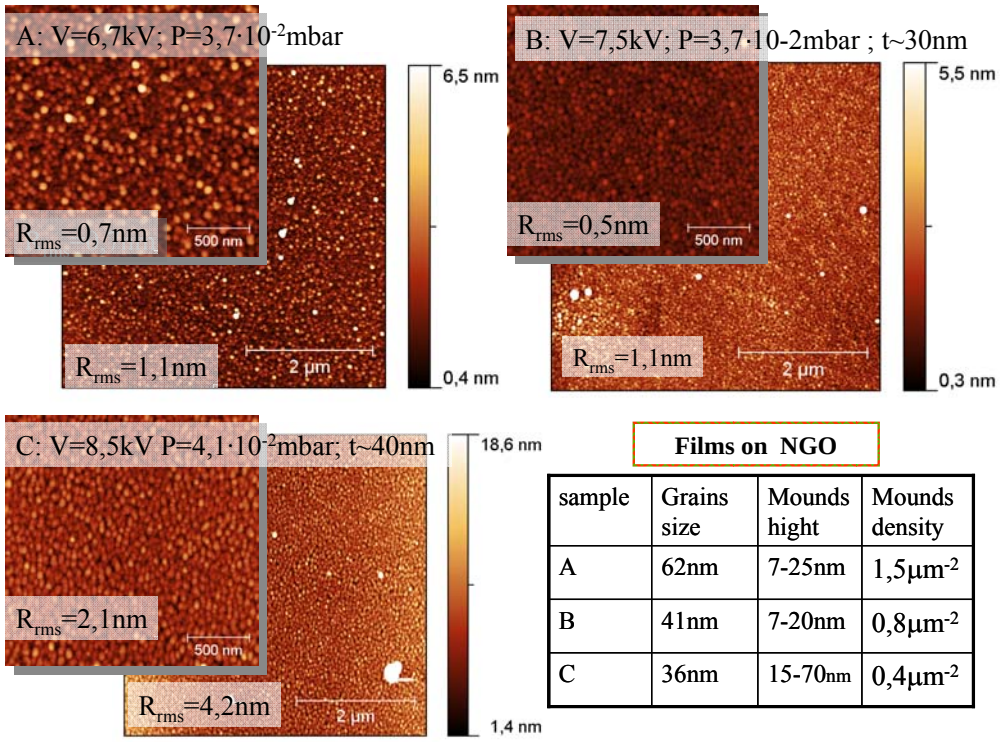

Films on NGO

sample	Grains size	Mounds hight	Mounds density
A	62nm	7-25nm	1,5µm^{-2}
B	41nm	7-20nm	0,8µm^{-2}
C	36nm	15-70nm	0,4µm^{-2}

Figure 23a presents a comparison between films deposited on different substrates and at different thicknesses. It is noticeable that 15nm thick LSMO film on NGO features a T* higher than the 40 nm film on STO, while the resistance is higher since the it is less thick (i.e. thinner section, thinking to Ohm's law). It comes out that NGO is a more suitable substrate for LSMO thin film deposition; one should be careful about the anisotropy which the film develops on this substrate.

Figure 23b presents the data for films grown at accelerating voltages of 7 KV, 7,5 KV, 8,5 KV, 9,5 KV. One notes that films grown at 7 KV, 8,5 KV and 9,5 KV have similar behavior, which betters for the lowest voltage, with the lowest resistance and MR ratio and the highest T*. All these films are 10 nm thick as measured by profilometer. The surface of the film deposited at 7 KV is presented in Figure 24 . A significant improvement is observed for 7,5 KV as accelerating potentials, but the profilometer revealed that these thickness of this film is twice the other. This is a relevant result and a closer look at the morphology of these films is proposed below.

Figure 23: Magnetotransport measurements of LSMO films on different substrates (a) and several voltages (b).

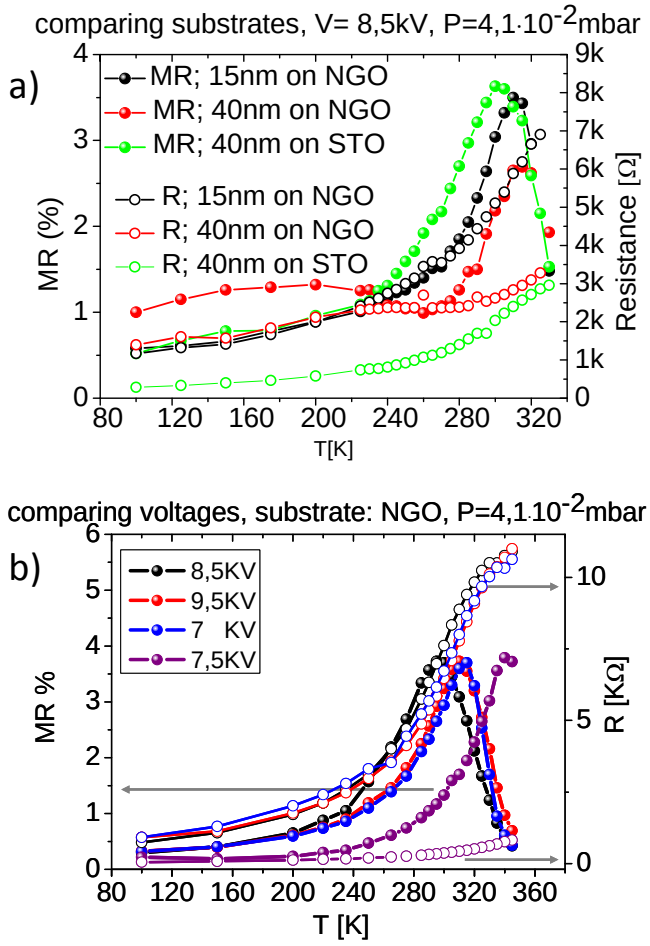

Figure 24: morpholgy of LSMO on NGO at 7,0KV and 4,1·10^{-2} mbar.

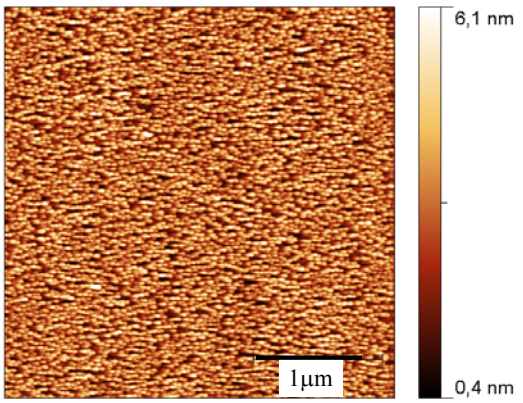

Understanding the effect of Pressure

In order to try to understand the described results we should perceive the effective role of the pressure in the LSMO growth by CSA. The oxygen pressure in the chamber during the growth modifies the film formation, of course. Nevertheless it is not satisfactory in the explanation of the improved morphology. In fact, we have to consider two aspects. First, the pressure role on the impinging atoms during the film formation was investigated by Thornton[164] and Haghiri-Gosnet and coworkers found LSMO follows the zone model[165], but they operated at a pressure one order of magnitude higher, and found a trend opposite to what we observe (in that model increasing pressure the roughness increases and the films properties defeat). Second, the pressure window we explored is extremely narrow. Thus the modification of atom kinetics during growth cannot provide such a significant morphology modification: we expect the main effect to result from the modification of the ablation process. In the following an explanation based on the plasma formation and propagation and on the ablation mechanism is proposed.

Increasing the pressure in a channel spark device the total pulse duration gets shorter. Its propagation is better neutralized, so that the beam is much more focalized, and the energy distribution of the electrons is more homogeneous[166]. A weaker ablation takes place, but thanks to the shortness of the beam the power effectively transferred to the target is still high enough to keep the stoichiometry preservation, which is the main advantage of the pulsed techniques. The lower rate and the absence of outgrowths confirm this guess.

The CSA plume mainly consists of single and double ionized species[167]. Thus the plume is better neutralized at higher pressure, it expands quickly and plasma maintains its energy during the plume expansion at times well after the pulse[168]. We can also think to a better thermalization, so these highly energetic, well thermalized, ions promote the film growth thanks.

A careful optimization of the deposition parameters for the bottom electrode of the spin valve device has been performed; a protocol has been elaborated which grants outgrowths-free surfaces and surface magnetic and electric properties. The conceptual core of the protocol is the

---

[164] J.A. Thornton, J. Vac. Sci. Tech. 1986, **4**, 3059.
[165] A.M. Haghiri-Gosnet, J. Wolfman, B. Mercey, Ch. Simon, P. Lecoeur, M. Korzenski, M. Hervieu, R. Desfeux, G. Baldinozzi, J. Appl. Phys. 2000, **88**, 4257; M. Kubaa, A.M. Haghiri-Gosnet, R. Desfeux, Ph. Lecoeur, W. Prellier, B. Mercey, J. Appl. Phys. 2003, **93**, 5227.
[166] E. Dewald, K. Frank, D.H.H. Hoffmann, R. Stark, M. Ganciu, B.N. Mandavhe, M.G. Nistor, A.-M. Pointu, I.I. Popescu, IEEE Trans. Plasma Sci. 1997, **25**, 272;
K. Frank, E. Dewald, C. Bickes, U. Ernst, M. Iberler, J. Meier, U. Prucker, A. Rainer, M. Schalug, J. Schwab, J. Urban, W. Weisser, D.H.H. Hoffmann, IEEE Trans. Plasma Sci. 1999, **27**, 1008;
E. Dewald, K. Frank, D.H.H. Hoffmann, A. Tauschwitz, IEEE Trans. Plasma Sci. 2002, **30**, 1820.
[167] S.D. Kovaleski, R.M. Gilgenbach, L.K. Ang, Y.Y. Lau, J.S. Lash, Appl. Surf. Sci. 1998, **127**, 947.
[168] S.D. Kovaleski, R.M. Gilgenbach, L.K. Ang, Y.Y. Lau, J. Appl. Phys. 1999, **86**, 7129.

increased pressure and decreased voltage, but not too much, in order to preserve the ablation process against a simple heating of the target surface.

LSMO growth mode

A possible Stranski-Krastanov (SK) transition is detected in LSMO thin films at a film thickness of 20 nm. At the best of our knowledge, this is the first time the SK is observed in LSMO compound.

Figure 25 compares the morphology of the LSMO film (on NGO substrate) having T* > 340K, which is 20 nm thick, with 5 nm thick film grown at the same conditions. A comparison of the profiles is also shown. While the 5nm thick film presents a complete absence of outgrowths and mounds, the 20 nm thick film presents a lot of mounds 20 nm high. The thickness of the former film was measured at a Alpha-step profilometer by TENCOR which gave the value of 40 nm. Since the structures on the surface are 20 nm high we deduce that the film is 20 nm thick plus these 3D structures. If these structures were structurally relaxed, but still metallic, we could explain the absence of anisotropy. The latter was verified by MOKE and by magnetotransport measurements with the magnetic field aligned along two perpendicular directions in the plane of the film. We think we have detected the onset of a Stranski-Krastanov (SK) transition where the epitaxial strain is released by the formation of these three-dimensional structures.

Figure 25: LSMO at 7,5KV—onset of SK transition.

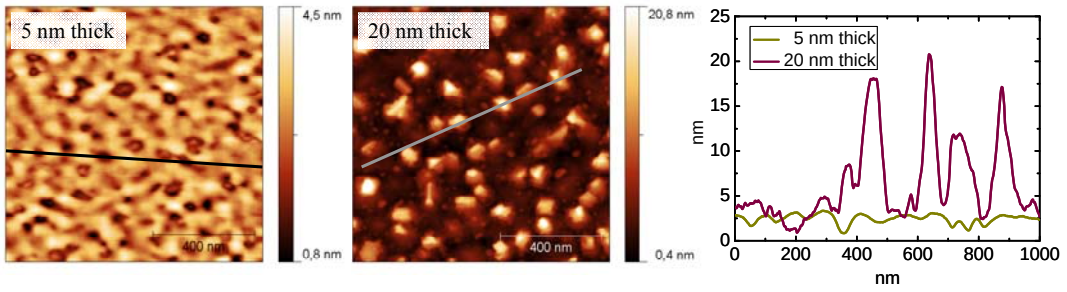

Figure 26 shows that for some of the 20 nm high mounds it is clearly visible an orientation. Two couples of orientations forming 90°-100° angles are distinguishable, these two groups are tilted of about 40° between them. Further investigate is needed to ensure the SK nature of this transition. this transition.

Figure 26: a deeper insight to the SK transition.

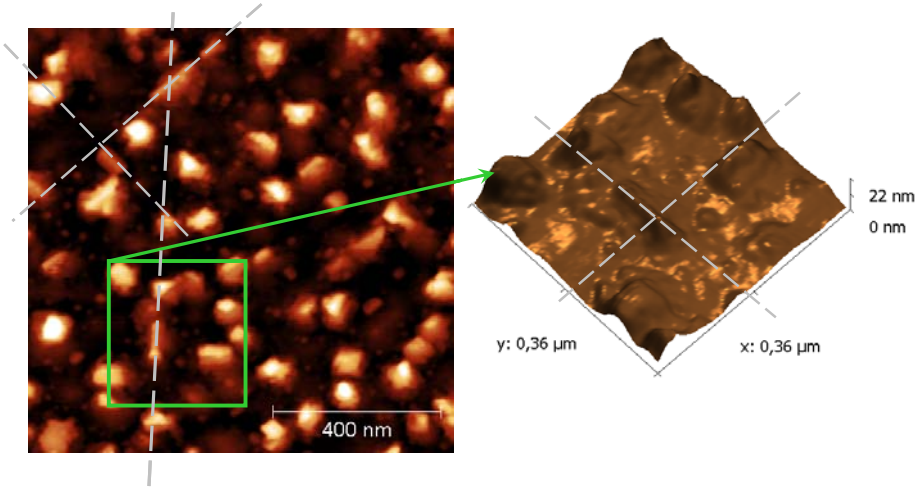

Figure 27: STM images of LSMO surface, recorded at 2V and 20pA. An AFM image of the same surface is reporte as comparison while an AFM micrograph of a film twice thinner is presented, featuring similar structures size.

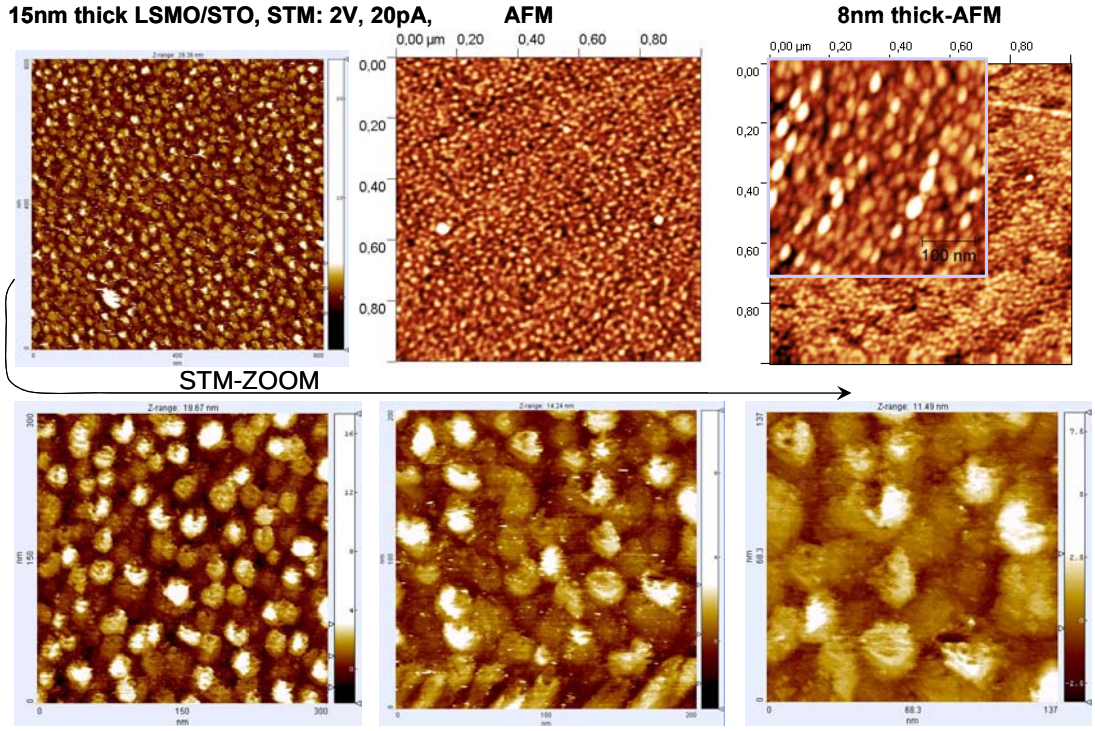

A Scanning Tunneling Microscopy (STM) study of the LSMO surface has been started during the presented PhD thesis, by Alessandro Gambardella and Andreas Straub. Here a brief preliminary investigation is reported in Figure 27. It is carried on a LSMO film deposited at 8,75 kV and $4{,}0 \cdot 10^{-2}$ mbar. Flat mounds are clearly observed, having an average size of 25nm. An AFM (tapping mode) of the same surface is presented. The features is quite similar, but it is a matter of fact that STM let a much more resolved images, since it is based on short range interactions.

In Figure 27 is reported also a topography of a film having double reduced thickness. We note that there is a correspondence between the topographies and the lateral features size is almost the same: by HHCF we estimated the mean mounds size in the 8nm thick film: it is 21±2 nm, very similar to the 25 nm detected by STM for the 15 nm thick film. Thus, combining these preliminary results with the concepts on thin film growth, the epitaxial growth of LSMO thin films seems to be limited by the step ES barrier which confines the ad-atoms on the terrace where they arrived. In High-T_C superconductor the films growth is known to occur via unit cell migration[169]. We can suppose that also LSMO thin films grow by diffusion of pluriatomic units having the symmetry of the LSMO crystal. Thus binding symmetry, in particular the known oriented c-axis growth, could create a very high E_{ES} almost preventing the atoms jumps from the terrace: a picture similar to Figure 7. Since we do not treat the STO substrate in order to select the TiO_2 termination we do not have a dominant step flow growth[170], rather a nucleation on the terraces.

[169] V.S. Achutharaman, N. Chandrasekhar, O.T. Valls, A.M. Goldman, Phys. Rev. B 1994, **50**, 8122.
[170] M. Kawasaki, M. Izumi, Y. Konishi, T. Manako, Y. Tokura, Mat. Sci. Eng. B 1999, **63**, 49.

Interface between amorphous organic semiconductor and ferromagnetic oxide or ferromagnetic metals.

LSMO/Alq_3 interface

Two organic semiconductors were considered in this work: Alq_3, because of its knowledge in organic light emitting devices (OLED) community[171], and pentacene (Pn), for its high mobility values[172] and because it is most frequently employed in organic electronic devices (extensive literature exists for Pn based devices).

In the case of Alq_3 deposited on LSMO the injection process is defined by the energy landscape at the interface and by the growth mode of the film. Alq_3 films deposited in our apparatus are known to be amorphous and the interfacial electronic structure was already studied by means of soft-XPS (60-600eV range)[173]. In this PhD work the interface was studied by means of Atomic Force microscopy (AFM) and Impedance Spectroscopy (IS)[174].

The optimization of the growth condition has been already performed, choosing the room temperature deposited amorphous film with a root mean square roughness of a few nanometers. The state of art for this interface at the beginning of the doctoral was the knowledge of the interfacial energetics and it is presented in Figure 28. The values evidenced by red circles are experimentally measured while the optical gap is considered in order to obtain the position of the LUMO level. A 0,9 eV dipole is established at the interface and the barrier for the electron injection is 1,1 eV versus the 1,7 eV one for hole injection, suggesting the Alq_3 is an electron transporter material. A so high dipole can be due to the intrinsic dipole moment of the Alq_3 molecule, ranging from 3.6D to 7,1D according to the computation method and to the state of charge[175].

The concentration of electrons thermally generated from the metal into the LUMO level can be estimated: $n = N_C \exp(-\varepsilon_F^{LUMO}/k_B T)$[176] where ε_F^{LUMO} is the energy distance between

[171] E. Arisi, I. Bergenti, V. Dediu, M.A. Loi, M. Muccini, M. Murgia, G. Ruani, C. Taliani, R. Zamboni, J. Appl. Phys. 2003, **93**, 768.
[172] T.W. Kelley, L. D. Boardman, T. D. Dunbar, D. V. Muyres, M. J. Pellerite and T. P. Smith, J. Phys. Chem. B 2003 **107**, 5877.
[173] Y.Q. Zhan, I. Bergenti, L, Hueso, V. Dediu, M.P. de Jong, Z.S. Li, Phys. Rev. B 2007, **76**, 045406.
[174] The experiment is published in: M. Barra, A. Cassinese, P. D'Angelo, L.E. Hueso, **P. Graziosi**, V. Dediu, Org. Electr. 2008, **9**, 911.
[175] A. Curioni, M. Boero, W. Andreoni, Chem. Phys. Lett. 1998, **294**, 263.
[176] H. Ishii, N. Hayashi, E. Ito, Y. Washizu, K. Sugi, Y. Kimura, M. Niwano, Y. Ouchi, K. Seki, Phys. Stat. Sol. (a) 2004, **201**, 1075.

the electrode Fermi level and the OSC LUMO level. Like for conventional semiconductor, the pre-exponential factor is the effective density of states, but the traditional estimation of the effective density of states (N_C relies on the free electron approximation (the factor two multiplying the parenthesis accounts for spin degeneration), which does not apply to OSC. Ishii and coauthors used the density of molecules doubled due to spin degeneration[176], but it is quite difficult to think that a molecule accommodates two electrons as it would be double ionized. Thus we consider as effective density of states equal to the molecule density. Alq_3 has a density of 1,51 g/cm^3 for amorphous films[177] and a molar weight of 459 g, the molecules density is $2{,}0\cdot10^{21}$ cm^{-3}, so n=$8{,}5\cdot10^{2}$ cm^{-3} at room temperature. To estimate how low is this value, let us consider a film having an area of 0,5cm^2 (e.g. a sample size of 10mm by 5mm). The density of transferred to Alq_3 charge carriers is about $4{,}25\cdot10^{2}$ cm^{-1} - so a 23 μm thick film with such area would have only one charge. This estimation means that there is not net charge in the film, as a consequence of the dipole, the band bending is not possible and the Fermi levels alignment is not achieved. Alq_3 behaves as intrinsic semiconductor and its Fermi level can be put in the middle of the gap. The picture is suggested also by I.-S. Park and co-workers, who suggest that in OSC the Fermi level should be considered in the middle of the gap and the equilibrium is reached by a change in the work function[178]. Indeed the interfacial dipole is measured by UPS as a shift of the electrode work function. The intrinsic dipole moment can account for the high value of the interface dipole without net charge in the film, whose situation is similar to that of a capacitor, like already found for Alq_3 films.

Figure 28: UPS results for the electronic structure of Alq_3 on LSMO.

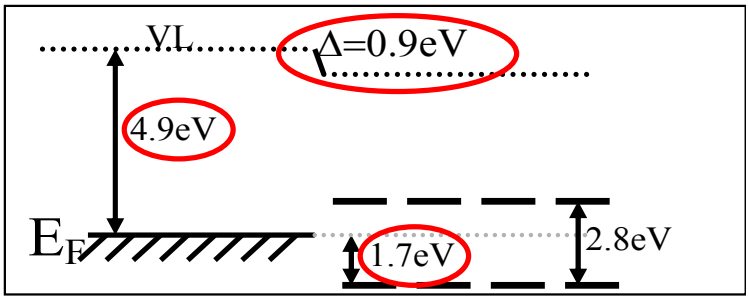

In addition to UPS/XPS approach, the interface was investigated by means of the impedance spectroscopy technique[179]. The measurements were performed by few of the co-

[177] C.H. Marée, R.A. Weller, L.C. Feldman, K. Pakbaz, H.W. Lee, J. Appl. Phys. 1998, **84**, 4013.
[178] I-S. Park, S. Park, J. Oh, J. Lee, Org. Elect. 2007, **8**, 382.
[179] M. Barra, A. Cassinese, P. D'Angelo, L.E. Hueso, **P. Graziosi**, V. Dediu, Org. Electr. 2008, **9**, 911.

authors, while the thesis author contribution is limited to the sample preparation and the overall discussion.

Figure 29: Impedance spectroscopy results for Alq_3/LSMO interface.

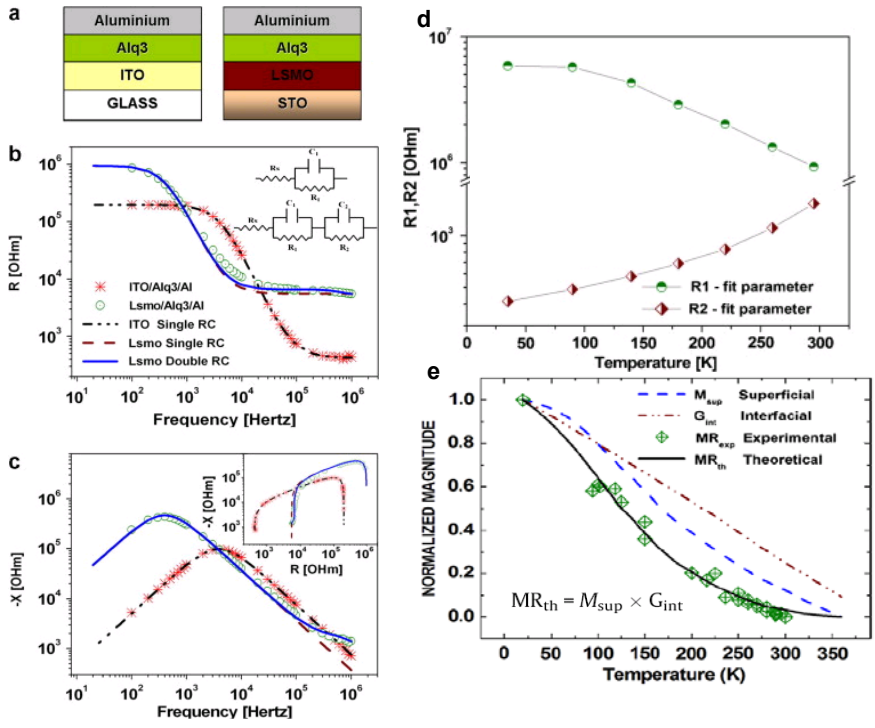

The experiment is carried on by comparison of Alq_3 devices with and without LSMO, in the latter the LSMO was substituted by ITO (Indium Tin Oxide). Figure 29a reports the typical devices structure. Figure 29b and c present the real and imaginary part of the impedance, measured at room temperature. The data were fitting by simulating the device as a resistance and a capacitor in parallel configurations: the former takes account of the current flowing while the latter of charging effect. The fitting with experimental data is obtained when the ITO/Alq_3/Al device is fitted by means of just one RC circuit while two RC in series are needed for the LSMO/Alq_3/Al case (R_1C_1 and R_2C_2). R_1 and C_1 are compared with the values extracted for ITO systems (since they are of the same order of magnitude, this will be supported by the temperature dependence analysis) and feature higher fitting values for both R and C.

For LSMO/Alq_3 system the impedance was also measure at several temperatures and the data fitted. The agreement is obtained for the same circuits. The temperature dependence of fitting parameter was further analyzed (Figure 29d). The circuit R_1C_1 shows a semiconducting behavior and is ascribed to Alq_3, which is a semiconductor. On the contrary the R_2C_2 circuit appears to be metallic, and is ascribed to the interface. Moreover the data

from spin valves devices were fitted by using a theoretical magnetoresistance obtained by multiplying the interface conductivity, taken as R_2^{-1}, with the surface magnetization of LSMO taken from literature[180]. The excellent agreement (Figure 30e) indicates that:

(I) the Alq_3 based spin valves are LSMO interface limited;

(II) the spin flip scattering events occurring in Alq_3 are not the limiting factor for device operation this range of temperatures (100-300 K). 124

Co/Alq_3 - the Tunnel Barrier is decisive

Co/Alq_3 - The bare interface

In spin devices it is relevant not only the efficient injection of the polarized current, but also its detection. In the first chapter we addressed the interface issues: it is not sufficient to optimize the component materials, the quality of the interfaces between them is crucial.

It was demonstrated that sputtered cobalt grows conformal to the organic under-layer, which morphology contributes in determining the magnetic anisotropy of the cobalt, and that relatively thick Co films (35nm) show excellent magnetic properties[181]. It has to be kept in mind that for spin device the interface magnetism completely dominates over the bulk one. Moodera and co-workers succeeded in the thermally evaporated deposition of ferromagnetic metals on top of very thin amorphous organic tunnel barrier (permalloy on Alq_3[182] and iron on rubrene[183]). Szulczewski and collaborators deposited by e-beam evaporation Co directly on top of thin Alq_3 (8nm at maximum) creating tunneling devices[184]. Nevertheless quite often cobalt penetration into the organic is detected[185]. Vardeny and co-workers evidenced about a 100nm thick *ill-defined* layer for the top cobalt penetration into Alq_3 (for Alq3 thinner than 100nm devices showed short circuits[186]). Vinzelberg and co-workers found that the irreproducibility of their devices can be ascribed to a tunneling regime due to Co filaments extended into the Alq_3 film for at least 50nm, as detected by

[180] H. Park, E. Vescovo, H.J. Kim, C. Kwon, R. Ramesh, T. Venkatesan, *Phys. Rev. Lett.* 1998, **81**,1953.
[181] I. Bergenti, A. Riminucci, E. Arisi, M. Murgia, M. Cavallini, M. Solzi, F. Casoli, V. Dediu, J. Magn. Magn. Mat. 2007, **316**, e987.
[182] T.S. Santos, J.S. Lee, P. Migdal, I.C. Lekshmi, B. Satpati, J.S. Moodera, Phys. Rev. Lett. 2007, **98**, 016601.
[183] J.H. Shim, K.V. Raman, Y.J. Park, T.S. Santos, G.X. Miao, B. Satpati, J.S. Moodera Phys. Rev. Lett. 2008, **100,** 226603.
[184] G. Szulczewski, H. Tokuc, K. Oguz, J.M.D. coey, Appl. Phys. Lett. 2009, **95**, 202506.
[185] V. Dediu, L.E. Hueso, I. Bergenti, C. Taliani, Nat. Mat. 2009, **8**, 707.
[186] Z.H. Xiong, D. Wu, Z.V. Vardeny, J. Shi, Nature 2004, **427**, 821.

Transmission Electron Microscope (TEM)[187]. The first cobalt atoms deposited on Alq_3 are known to form complexes[188,189]. These complexes can constitute obstacles for the injection *into* the organic film.

The optimization of the 3d-metal on top of the organic semiconductors constitutes a key research topic in the hybrid spintronics field.

Al_2O_3 as tunnel barrier

In this paragraph an innovative and advanced engineering of the interfaces is presented. It consists in the insertion of a thin tunneling layer of aluminum oxide between the organic semiconductor and the top metallic electrode. An extensive effort has been done in order to understand the role of this barrier. The reason for the introduction of such a tunneling barrier at the interface relies in the change of the electrons kinetics. It prevents possible back diffusion exploiting the possibilities developed by A. Fert and coworkers[190].

Thin Al_2O_3 tunneling layer insertion between the organic layer and the top Al cathode is well studied in Alq_3 based OLEDs as an alternative to LiF, because the latter reacts chemically[191]. The aluminum oxide buffer layer increases the electron efficiency from the cathode since hole accumulation at the organic side of the Al_2O_3 raises the Fermi level in respect to the LUMO. This effect increases with the barrier thickness, but also the interfacial resistance increases: a compromise has to be found. Since the magnitude of the E_F shift is determined by the voltage drop across the whole layer between anode and cathode, the optimal Al_2O_3 thickness is related not only to the thickness of the buffer layer, but also to that of the organic layer, ranging from 0,8nm in 60nm thick Alq_3 films to 2,6 nm for 200 nm thick Alq_3 layers[192]. This model, which considers also the bulk effect of the film, gives experimentally agreement for single layer Alq_3 devices and Alq_3 based OLEDs. The insertion of an insulating buffer layer of the proper thickness increases the efficiency of OLEDs.

The experimental work performed during the present thesis explains how and why a tunnel barrier between the organic film and the top cobalt electrode improves the spin transfer at the interface. The choice of Al_2O_3 as tunnel barrier material relies on several considerations. First it is successfully used in MTJs. Next it is a simple and very stable oxide: no stoichiometry problems

[187] H. Vinzelberg, J. Schumann, D. Elefant, R.B. Gangineni, J. Thomas, B. Büchner, J. Appl. Phys. 2008, **103**, 093720.
[188] W. Xu, J. Brauer, G. Szulczewski, M. Sky Driver, A.N. Caruso, Appl. Phys. Lett. 2009, **94**, 233302.
[189] Y.Q. Zhan, M.P. de Jong, F.H. Li, V. Dediu, M. Fahlman, W.R. Salaneck, Phys. Rev. B 2008, **78**, 045208.
[190] A. Fert, J. George, H. Jaffres, and R. Mattana, IEEE Trans. Electron Dev. 2007, **54**, 921.
[191] L.S. Hung, R.Q. Zhang, P. He, G. Mason, J. Phys. D 2002, **35**, 103.
[192] S.T. Zhang, X.M. Ding, J.M. Zhao, H.Z. Shi, J. He, Z.H. Xiong, H.J. Ding, E.G. Obbard, Y.Q. Zhan, W. Huang, X.Y. Hou, Appl. Phys. Lett. 2004, **84**, 425.

exist and the right oxygen content is guaranteed by the thermodynamic stability of the compound (one of the most stable oxide[193]). The 3+ and 2- are the only valences allowed for aluminum and oxygen respectively (apart from valence 0, of course). Furthermore, the Gibbs free energy of formation for Al_2O_3 is -1582,3 KJ/mol while only -241,2 KJ/mol for CoO. Thus the thermodynamics favors the bond Al—O instead of the Co—O. Finally Al has a low *Z* (atomic number) which means low spin-orbit interaction, although the Al nuclear magnetic moment is quite high (μ_I=3,639μ_N[194]), which means possible hyperfine interaction induced scattering.

The buried interface was studied by means of spectroscopic techniques such as UPS and XPS, x-ray reflectometry and XMCD. The structure was analyzed also by means of TEM. Magnetomertric measurements (NMR, SQUID, MOKE) has been performed on the top deposited cobalt. The author worked on tunnel barrier deposition and morphological characterizations and was actively involved in discussions of spectroscopic characterizations.

Let's now discuss the deposition condition. Since it is known that Al deposited on top of Alq_3 gives rise to extensive chemical interaction[195] the aluminum oxide has been deposited directly, ruling out the idea of the metal deposition and following oxidation. The Al_2O_3 films deposition was performed by channel spark ablation of an alumina ceramic target. Due to the strength of the Al—O chemical bond in Al_2O_3 a voltage of 14 kV is used (the effective ablation has not been observed for voltages lower than 12,25 kV) at an oxygen pressure of $2{,}8\cdot10^{-2}$ mbar in order to obtain a weaker ablation.

First of all we mention that the MR intensity of the spin valve strongly depend on the thickness of the barrier and is completely suppressed for 5nm thick aluminum oxide layer. According to Helander and co-workers[196], who studied the alkali-fluoride thin film deposition on top of Alq_3, this is an indirect proof of the uniform coverage achieved by the oxide layer: if Al_2O_3 grew in islands a less strong dependence on the thickness would be recorded, due to thinner regions in the interface.

[193] Handbook of Chemistry and Physics, 85th edition, David Lide ed., 2005, CRC Press, Boca Raton.
[194] C. Kittel, "Introduction to Solid State Physics", WILEY; 8th edition (November 11, 2004).
[195] C. Shen, A. Kahn, J. Schwartz: J. Appl. Phys. 2001, **89**, 449.
[196] M.G. Helander, Z.B. Wang, L. Mordukhovski, Z.H. Lu, J. Appl. Phys. 2008, **104**, 094510.

Figure 30: Resonant polarized x-ray reflectometry.

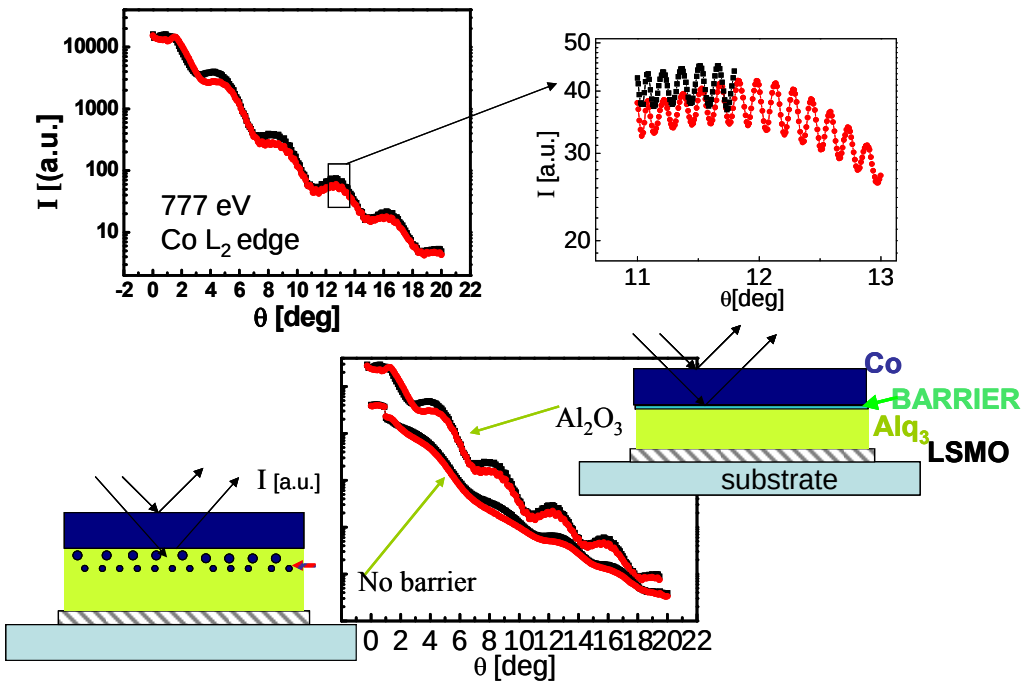

The first structural characterization of the thin tunnel barrier is performed by analyzing the whole interface (i.e. $Co/Al_2O_3/Alq_3$) by means of x-ray reflectometry, using *resonant* x-ray magnetic scattering (polarized synchrotron light) tuned on the Co L_2 adsorption edge. This tuning lets us to have a high cross section and high penetration in the Co films, gaining the best sensitivity of the cobalt element. The layers are $Au_{(1nm)}/Co_{(5nm)}/Alq_{3(100nm)}$ and $Au_{(1nm)}/Co_{(5nm)}/Al_2O_{3(1nm)}/Alq_{3(100nm)}$ (from the top to the bottom). Cobalt films were deposited by sputtering at the IMEM-CNR institute in Parma. The measured structures were deposited on both silicon and LSMO/STO and gave the same results, reported in Figure 30. The black and red lines refer to different applied magnetic field directions: since, for a given magnetization of the film, the cross section changes for clockwise or counterclockwise polarizations, the in-plane magnetization of the film has been switched instead of changing the light polarization. The photons interact by interference and the resulting spectrum is modulated according to the difference of optical path, which decreases increasing the thickness and which is proportional to the detection angle.

The measurements were performed at the synchrotron ELETTRA by Ilaria Bergenti and Francesco Borgatti.

From the spectra one can see that the samples with and without tunnel barrier have different critical angle: 0,898 ° for Co without Al_2O_3 and 1,498 ° with it. Since the critical angle is related to the electron density and to the scattering factor, one could conclude that when Co is deposited on top of the barrier the metallic properties are better. Furthermore two modulations exist. One, very short, is presented in the inset and corresponds to the whole thickness of the sample. Another oscillation, longer, is superimposed to the shorter and modulates it - this refers to Co. The first qualitative result is that the interference fringes are much more pronounced for the samples with the tunnel barrier inserted. This is the sign of sharper interfaces giving a more clear photon reflection.

In the fitting procedure only the two layers were considered while the interface is simulated by inserting layer of electronic density comprise between the Co and the Alq_3 ones. Thus the width of the interface region is obtained. The alumina barrier is perceived as a part of the Co/Alq_3 interface. Fitting procedures show that the interface width is 4nm for the Co/Alq_3 interface and 2,5 nm for the Co/Al_2O_3(1nm)/Alq_3 one. The natural conclusion is that Co penetrates in the Alq_3 for about 4nm. Considering that the Alq_3 molecular size is about 1,5 nm[197], for a 1 nm thick Al_2O_3, the interface width of 2,5 nm indicates that the buffer layer stop almost completely the Co penetration.

Further investigation has been made by means of Transmission Electron Microscopy (TEM) and Electron Energy Loss Spectroscopy (EELS). The samples analyzed are Co(5nm)/tb/Alq_3(50nm) on silicon, were tb corresponds to 0 nm, 2 nm, 5 nm of Al_2O_3. The TEM and EELS measurements were performed at the department of Physics and Astronomy at the university of Glasgow by John Chapman and Donald MacLaren. Possible native silica, Alq_3 and the Al_2O_3 are not distinguished since their low atomic number and amorphous character. Platinum is capping layer.

Figure 31 reports a few images concerning the three different oxide thicknesses. Co appears polycrystalline and cobalt lattice fringes extended in the “white” layer for a few nanometers. In order to measure accurately the extension of these interfaces, spectroscopic measurements with elemental resolution were performed. From EELS the interface width is about 5 nm in absence of the barrier and with a 2 nm thick barrier while it is about 3,5 nm with 5 nm thick Al_2O_3. So there is evidence for the cobalt penetration into the barrier, but the aluminum oxide layer stops cobalt diffusion.

[197] M. Brinkmann, G. Gadret, M. Muccini, C. Taliani, N. Masciocchi, A. Sironi, J. Am. Chem. Soc. 2000, **122**, 5147.

Figure 31: a few TEM images measured at the University of Glasgow.

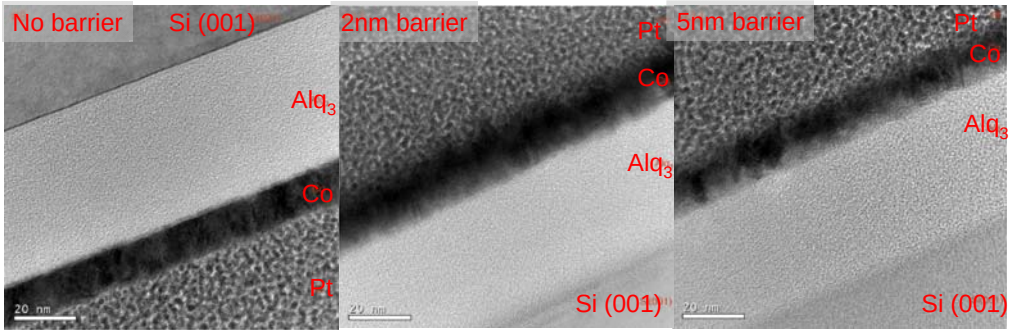

A chemical characterization is required in order to check if the barrier really prevents the Co penetration into the following organic layer. The investigation was performed by HArd X-ray Photoelectron Spectroscopy (HAXPES) at the ESRF-Grenoble by Francesco Borgatti, Ilaria Bergenti, Federico Bona[198]. About the Co reactivity, the result is the same of the previous experiment: a chemical reaction with complex formation occurs between cobalt and Alq_3 when the deposition happens without a buffer layer, whose presence prevents the reaction. From the Alq_3 side, the core level of all the characteristics atoms are investigated. The use of such high energetic photons let to explore buried interfaces. Now a brief data presentation follows.

Figure 32: HAXPES result summary for the element container in Alq_3; the arrows indicate charge addiction.

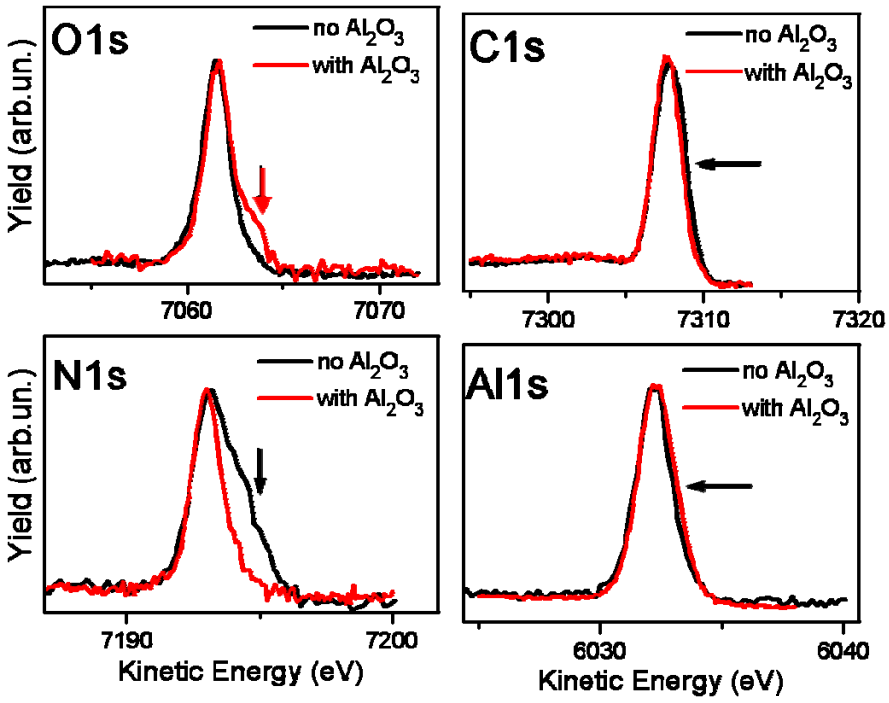

[198] HAXPES and TEM data will be published in Appl. Phys. Lett., F. Borgatti *et al.* .

Figure 32 presents the data regarding the Alq_3 elements: carbon, oxygen, nitrogen, aluminum; on the abscissa the kinetic energy of the detected emitted photon is reported. Since the incoming photon energy is 7,6 keV the difference between the two values gives the binding energy. At first we note that charge addition is observed in the O(1*s*) orbital when barrier is deposited: this is ascribed to the signal from the oxygen in the barrier. Also the different shape of the peak of the aluminum 1*s* level is linked to the signal from the buffer layer. The 1*s* atomic orbital of the carbon appear to be not influenced from the barrier.

Significant charge addition is detected in the N(1*s*) level indicating that complex formation, a well known process in top metal deposited hybrid interfaces, occurs as a consequence of the Co penetration and reaction.

Data on O(1*s*) and N(1*s*) demonstrate that when cobalt is deposited on Alq_3 without buffer layer a chemical reaction and the formation of a complex occur which involve Co, O and N atoms. Figure 33 presents a simple bi-dimensional sketch of such a complex. The complex formation involves one of the two doublet located on oxygen atom and not involved in the bond, and a dative bond with nitrogen atom and the consequently rupture of the aromaticity of the quinolate ring, which lose part of the charge delocalization, with relevant damages for the electrical properties.

Figure 33: a simple sketch of Co complex formation involving (as stressed by the celeste color) the free doublets and a dative bond (traditionally indicated by an arrow, in chemistry) with the rupture of the aromaticity.

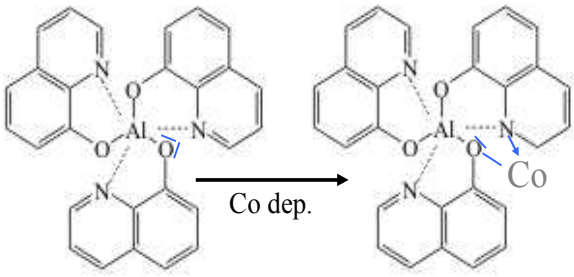

In addition XMCD, XPS and UPS measurements were performed at the beam line at Linköping University by YiQiang Zhan and co-workers in a top inverted geometry: the sample geometry was inverted by a carbon tape[200]. UPS measurements indicates the formation of 1,3eV dipole at the interface, similar to that of 1,4eV measured for the bare Co/Alq_3 interface[199]. By the same way of the $LSMO/Alq_3$ interface, we estimate a thermally activate carrier concentration in the Alq_3 film coming from the Co electrode of $8{,}7\cdot10^{7}cm^{-3}$ for the $Co/Al_2O_3/Alq_3$ interface. This value implies that in a device made of 100nm thick Alq_3 with an active area of $1mm^2$ there should

[199]Y. Q. Zhan, Phys. Rev. B 2008, cited[190].

be only one charged molecule. Anyway we can't exclude the presence of some carriers in interfacial levels near the Fermi level of the cobalt.

Now we try to put all these data together achieving a picture of the device energetics. We consider the electrodes, LSMO and Co, at the same potential, i.e. their Fermi levels are aligned, while we ignore the Alq_3 Fermi level and put it in the middle of the gap. The bands position is derived from the UPS data. Figure 34 sketches the device bands. The black values are derived from the measurements while the gray ones are estimated by considering a gap value of 2,8 eV. The green levels represent interfacial levels and gap localized levels, whose presence relies on the reasoning performed in the section on the transport in OSC. We stress out that these levels cannot be detected by UPS[200] since their dynamic is too slow. The energetic picture in which electrons move during the device performance is different from that coming from spectroscopy and include mainly the interface levels, which are always aligned at the Fermi level of the electrode, most of all if an insulating layer exist at the interface[200]. At each interface a dipole exists. Which is higher at the interface with cobalt. So a net dipole moment exists across the whole film, whose energy can be thought to be 0,4eV when the two electrodes are at the same potentials. This net dipole moment is due to a partial ordering of the Alq_3 molecules: the molecular dipole orientation is mostly random, but a finite polarization still remains in average. A similar result was already found in Alq_3 films[201]. The Alq_3 molecule dipoles can reorient under an applied electric field and the energetics could be again different during the transport.

Figure 34: Energy bands scheme of the device.

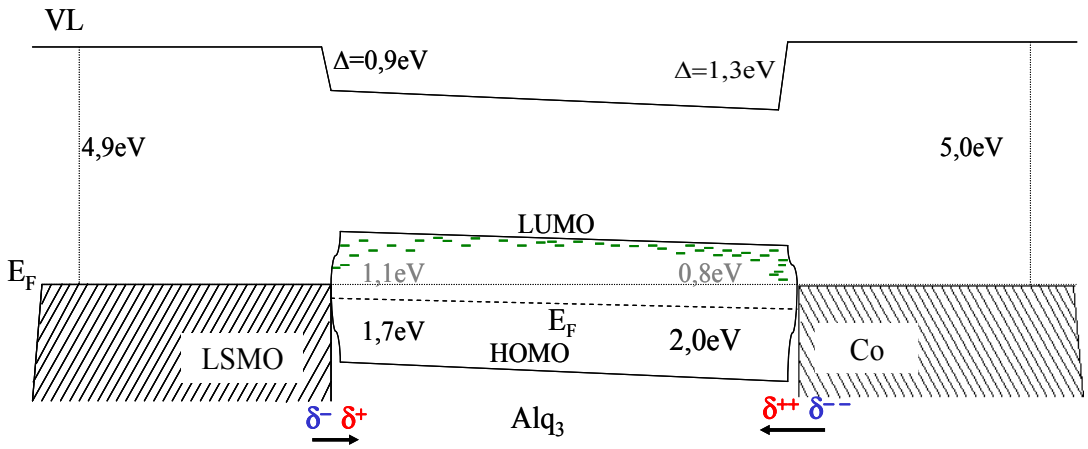

[200] J.C. Scott, J. Vac. Sci. Technol. A, 2003, **21**, 521.
[201] H. Ishii, N. Hayashi, E. Ito, Y. Washizu, K. Sugi, Y. Kimura, M. Niwano, Y. Ouchi, K. Seki, Phys. Stat. Sol. (a) 2004, **201**, 1075.

Figure 35 summarizes the XPS and XNCD data. The data were collected for the atomic core orbitals 1*s* of the oxygen and $2p_{3/2}$ of the cobalt.

The appearance of an additional peak at 529,6 eV in the O(1*s*) spectrum (marked by the azure arrow in Figure 35a) in the system without the barrier has been ascribed to a strong interaction between Co and Alq_3. This additional peak disappears when the Al_2O_3 buffer layer is inserted between Alq_3 and Co. There is only one peak in the spectrum of O(1*s*), which matches very well the peak of the pure Alq_3. In Figure 4(a) of a previous work from the same group on the Co/Alq_3 interface we note that the additional peak in O(1*s*) spectrum is observed only in the inverted geometry and not when the spectrum is collected in the normal top geometry: that peak is referred to the interface, as was proved also by further control experiment[200]. The angle dependent Co$2p_{3/2}$ spectra of both the interfaces (with and without the buffer layer) are shown in Figure 35b. This spectra was measured with different angles in respect to the surface and are denoted as the values of the angles in the figure. In absence of the tunnel barrier, a clear new peak appeared at the position of 781 eV. When decreasing the take-off angle, the ratio between this peak and the main peak (778 eV) increased, which indicates that an interaction between Alq_3 and Co occurred at the interface. However, in the Alq_3/Al_2O_3/Co system, all the spectra have the same feature independent upon the takeoff angles. There is no additional peak presented in the Co$2p_{3/2}$ spectra, even at low takeoff angles. The absence of the new peak indicates the inserted buffer layer separates the organic film and the top ferromagnetic film and prevents chemical interaction between them.

During the same experiment also the magnetic properties of the ferromagnetic electrodes have been checked. The objective is to observe the Co layer closest to the interface, since they are involved in injection and detection phenomena. X-Ray magnetic Circular Dichroism is the used technique to determine the minimum Co thickness that starts to be FM in each case: bare Alq_3 and Al_2O_3 buffered Alq_3. Co was e-beam evaporated *in situ* (in the beam line chamber) on the bare Alq_3 and Al_2O_3/Alq_3 surface prepared in Bologna. The measurements show that the minimum amount of Co necessary to detect a ferromagnetic signal is 4nm for “naked” surface and 2nm for the oxide covered ones. In the case of the buffer layer the magnetically dead layer is the half of that in absence of the barrier. Moreover the chemical reaction with Alq_3 are prevented: Figure 35c,d.

Figure 35: XPS measurements on orbital 1s of oxygen (a) and properties of Co with and without tunnel barrier: XPS (b) and XMCD (c,d).

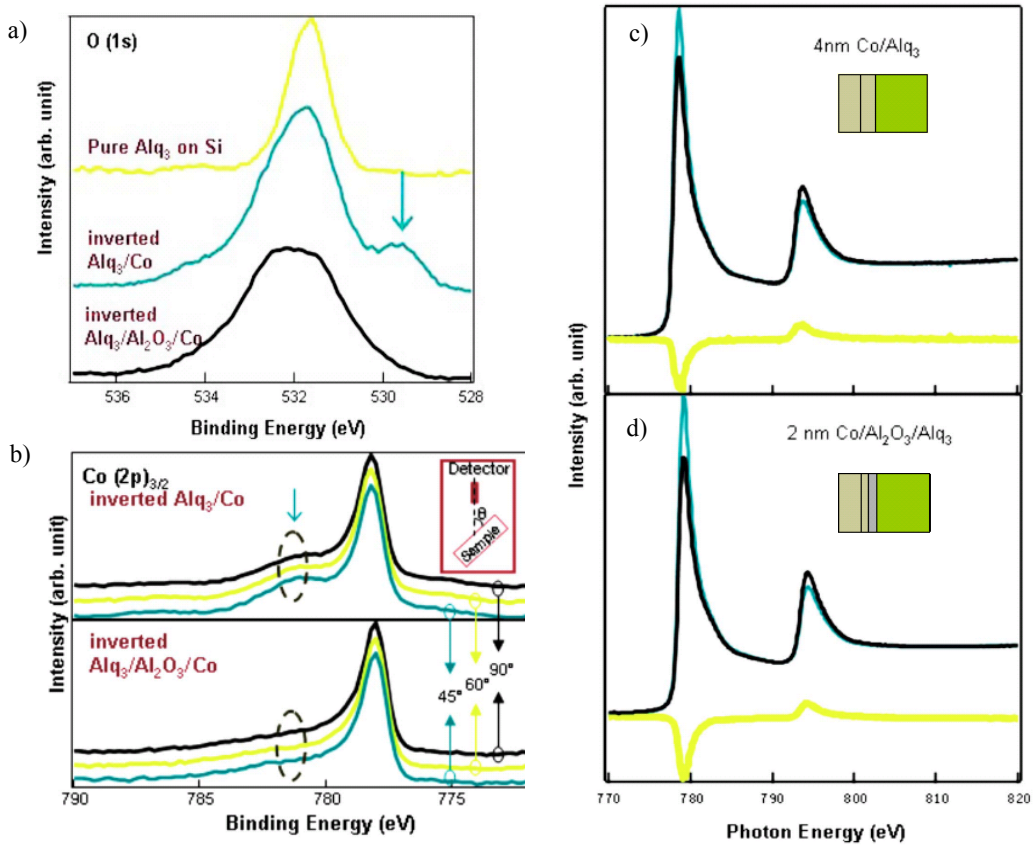

Now a deeper insight in the magnetic properties of the cobalt will be done. SQUID magnetometry let us to know that the oxide layer improves also the average magnetization of the Co film, recovering the best value obtained for direct deposition of Co on Si, but with a reduction of about the 14%, for barrier of 3nm or more. We consider as reference the value for Co film instead of that of the bulk one (which is about 1440 emu/cm^3) since polycrystalline films usually show lower M_S values. Table 2 reports the saturation magnetization M_S as measured by SQUID magnetometry. TEM data let suppose that for thinner barrier the Co partially penetrate into the barrier vanishing the effect. SQUID magnetometry was performed by Chiara Pernechele and Massimo Solzi at the University of Parma[202].

MOKE measurements reveal that Co deposited on Alq_3 presents an in-plane anisotropy with easy and hard perpendicular axis. In-plane anisotropy is characteristic for cobalt thin films, it depends on its crystalline structure. It is kept when the barrier is inserted and when the trilayer is grown on LSMO instead of Si. In facts it will be shown below that the aluminum oxide buffer layer does not change the overall organic morphology.

[202] Data will be published on J. Magn. Magn. Mat., C. Pernechele *et al.* .

Table 2: Saturation magnetization measured by SQUID at room temperature for Co films.

Co (15nm)	M_S (emu/cm^3)
Direct deposition on silicon	1130
Deposited on Alq_3 (50nm)	890
1nm Al_2O_3/Alq_3	946
3nm Al_2O_3/Alq_3	1106

Figure 36: Polar diagram of the coercive field of the Co film accordino to the angle of the laser polarization.

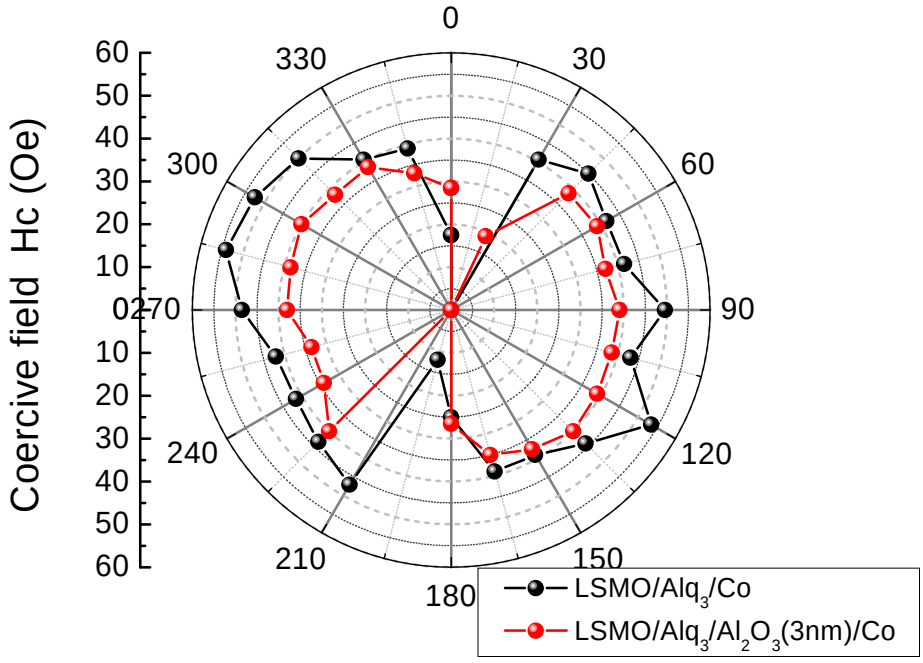

The bottom interface was analyzed also by NMR. Samples for NMR are deposited on silicon substrates and consist in Ta(2nm)/Co(15nm)/tb/Alq_3(50nm). tb stands for tunnel barrier and samples with 0, 1, 2, 3, 4nm thick Al_2O_3 were measured. The Alq_3 and the aluminum oxide layer were prepared in Bologna, the Co and the tantalum capping layer were sputtered by Luis Eduardo Hueso in Leeds. NMR measurements were performed by Andrey Sidorenko and Roberto De Renzi, at the Parma University . The NMR spectra will not be shown. They feature a distinct peak at 220MHz which is the convolution of two peaks, one coming from the face centered cube (fcc) structure and the other from hexagonal closed packaged (hcp) order. An additional peak is observed at lower frequency for Al_2O_3 barrier thickness $\geq$ 2nm; it is attributed to the fact that cobalt interacts with aluminum. For this peak to be detected, the Co atoms have to be in a

consistent Al neighboring environment. Because the Al density is very low in Alq_3, this peak appear only when the cobalt atoms impact on the continuous buffer layer. This is an indirect proof for the continuous nature of the 2nm thick aluminum oxide buffer and for the blocking role which the Al_2O_3 plays versus the incoming Co flux during the deposition.

Oxide buffer layer prevents ageing effects and damages.

Figure 37: 10nm Alq_3 thin film deposited at room temperature; the inset is the same image to which the mask used for the grain analysis is superimposed.

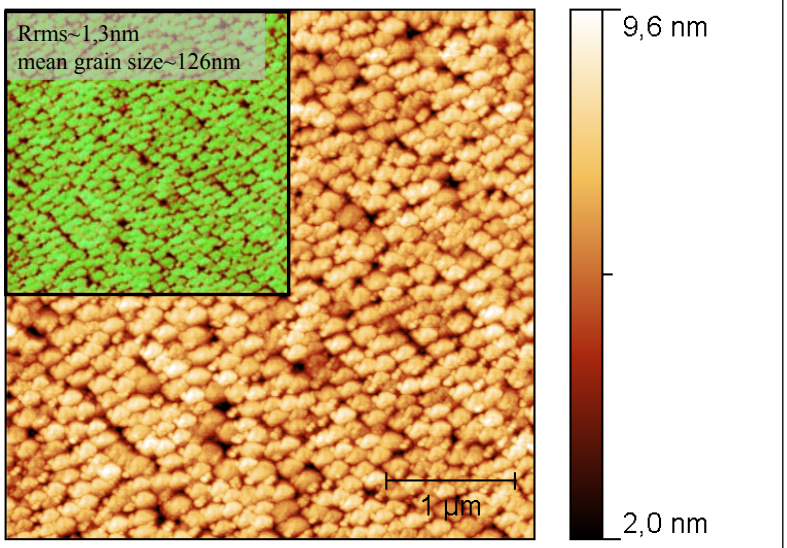

The effect of the barrier was studied also by a careful analysis of the surface of Alq_3 films[203] after the deposition of the Al_2O_3 and of the Co surface deposited on top of the organic layer without and with the aluminum oxide buffer layer. First of all we present the surface of nominal 10 nm thick Alq_3 deposited on the LSMO surface and imaged by AFM one day after the deposition (Figure 37). The film consists of quite smooth grains. The grains are analyzed by the watershed algorithm[204] implemented on the Gwyddion software. Their mean size (the diameter of the circle having the mean grain area) is 126nm: as they are asymmetric the maximum and minimum bounding size are extracted from the software. Obviously there are distributions of minimum and maximum sizes, which are peaked at 169 and 121 nm. The in-plane anisotropy of the Co deposited on top is possibly due to the anisotropy of the grains. rms roughness is 1,29 nm. From the grain analysis a real thickness could be estimated, assuming that the substrate is at the

[203] The Alq_3 films used for the AFM imaging were deposited by David Brunel while the author deposited the Al_2O_3 film and performed AFM studies.
[204] P. Klapetek, I. Ohlídal, D. Franta, A.. Montaigne-Ramil, A. Bonanni, D. Stifter, H. Sitter, Acta Physica Slovacca 2003, **53**, 223.

bottom of the grain. From the total grain volume, referred to the minimum of each grain, the thickness obtained is about 1,25nm, so we state that the coverage is complete.

Then we deposit 1, 2, 4 nm of Al_2O_3 on 50 nm thick Alq_3 films deposited on top of LSMO surfaces. They are imaged by AFM the day after the oxide deposition (i.e. two or three days after the Alq_3 deposition), one week later and eleven months later. Figure 38 reports some AFM measurements performed one day and one week after the deposition of the barrier, for the structure $Al_2O_{3(x)}/Alq_{3(50nm)}$/LSMO, where x is 1, 2, 4 nm as signed in figure.

The morphology appears to be quite different (from Figure 37) showing "spanish bean-like" features. On top of the large islands smaller grains are clearly observed, the smallest grain become more pronounced increasing alumina thickness. The different morphology could be due to the increased thickness, the barrier deposition, the few days ageing. The morphology is further analyzed by grain analysis (size and distribution) and Height-Height Correlation Function (HHCF). From grain analysis we aim to extract the size of the smallest grains while from HHCF the larger grain size and the roughness exponent are extracted[205]. HHCF is computed from the translation range 0- 4 0nm in order to satisfy the condition $t << \xi$.

After one week a slight increase of rms roughness is detected, but it can be ascribed as well to a different tip used. Also, the mound size is not significatively changed and the smaller grains are still more pronounced in the 4 nm barrier film. Only the roughness exponent α is increased (HHCF is computed from highest resolved images and α is calculated by a fitting in the made from 0 to 40 nm region).

After eleven months, during which the sample were in a dry box in air, the situation is exactly the same: Figure 39. For the samples with 1 nm and 4 nm thick Al_2O_3 layers the rms roughness are 1,2 nm and 1,4 nm, the roughness exponent 0,81 and 0,82, respectively; the correlation length is about 90 nm for both the images. The only parameter which really seems to be affected by the time is the roughness exponent α, which contains information on the local roughness, or surface slope. It increases from the day after the deposition to eleven months later: from 0,56 to 0,81 for the sample with 1 nm thick barrier and form 0,57 to 0,82 for that with the 4 nm thick oxide-

[205] J.W. Evans, P.A. Thiel, M. C. Bartelt, Surf. Sci. Rep. 2006, **61**, 1 ; see in particular the paragraph 3.4, p. 15, and fig.8.

Figure 38: AFM images of Al_2O_3 on Alq_3 on LSMO after one day (top) and one week (bottom) te barrier deposition.

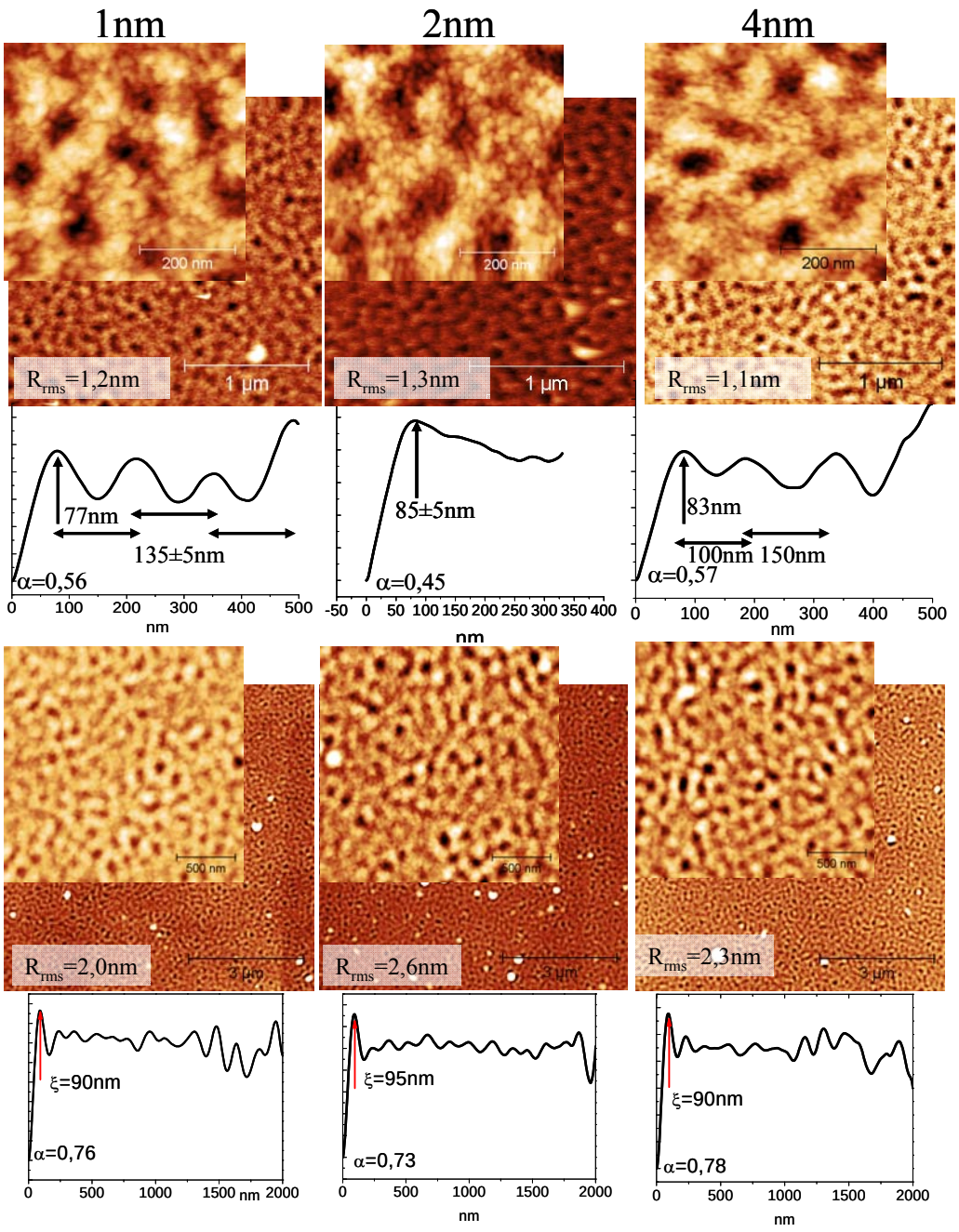

Figure 39: 50nm Alq_3 on LSMO with 1nm and 4nm thick alumina layer, measured 11 months after the deposition.

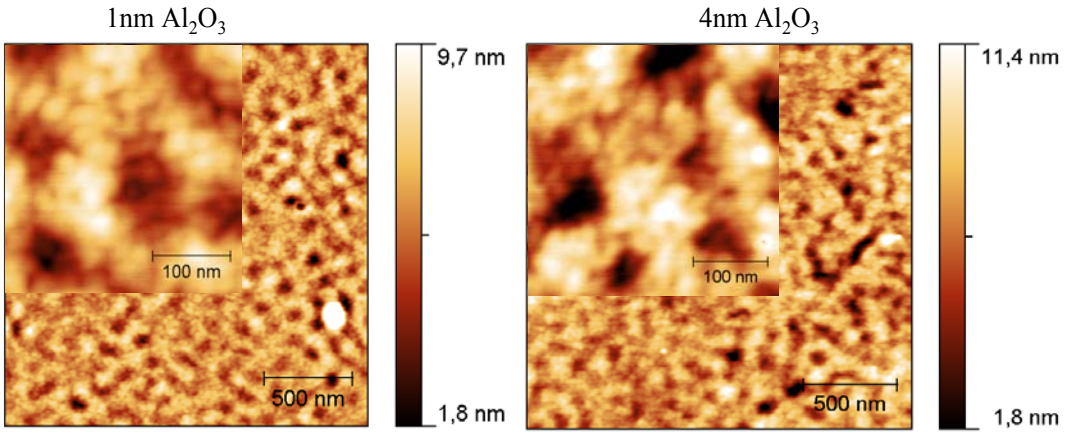

Thus the surface features and width, roughness, mound size, are preserved with the tunnel barrier, while when it is not deposited, *after five months the situation is worsen*. On top of the Alq_3 surface the early stages of Co growth were investigated by AFM. 2 nm of Co were thermally evaporated by e-gun on top of bare Alq_3 films and 2 nm alumina covered Alq_3 films, deposited on silicon substrates. Since the XMCD (Figure 35c,d) shows these film own ferromagnetic behavior only with the barrier insertion, the aim of this experiment is only to investigated a possible Co morphology modification induced by the alumina barrier. The analysis is carried on in the same way as that just above described.

Figure 40: AFM topography of 2nm thick Co film on Alq_3 without (left) and with (right) the Al_2O_3 buffer layer.

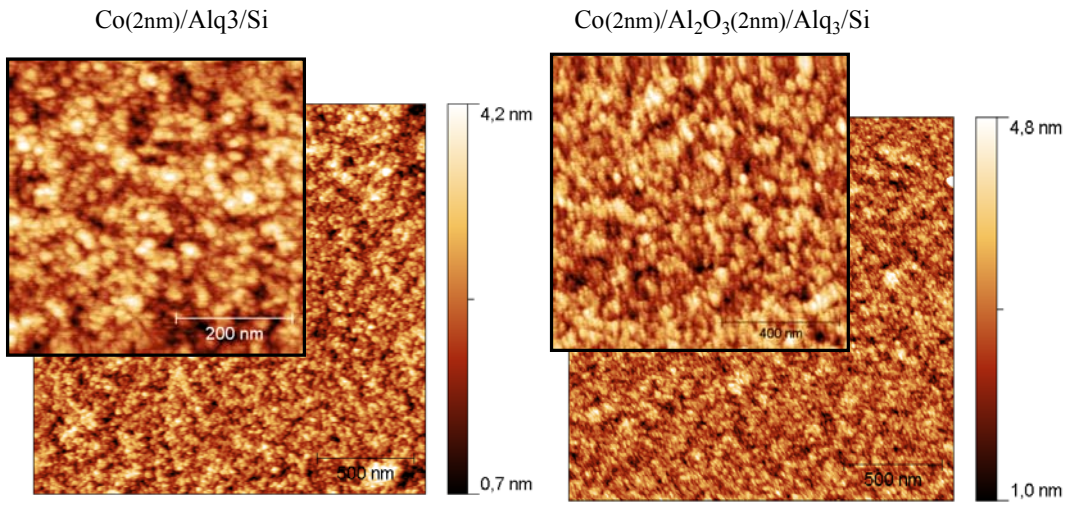

Figure 40 presents AFM images of the surface of 2 nm thick Co films on top of Alq_3 layer,. with and without the barrier. The rms roughness does not change with the alumina barrier insertion, and is 0,5 nm. Differently, the mean peak-valley roughness (R_{tm}) increases from 1,9 nm

to 2,2 nm when the alumina barrier is inserted. From HHCF calculation we obtain a grain size of 55 ± 3 nm with a larger modulation of about 120nm for the sample without barrier and a grain size of 100 ± 5 nm when the 2 nm oxide film is inserted. The roughness exponent could not be computed since the $t << \xi$ region is between 0 and 15nm (before the flexus of the HHCF curve), which is a range scale too near the lateral AFM resolution and it makes no sense. Surface damages are observed, like round holes of a diameter around 150 - 180 nm and 5 nm depth. Inserting the oxide buffer layer the damage density is drastically decreased (we detect just one of such a damage).

Figure 41 shows a damaged surface of Co(2nm)/Alq_3 with a line profile from which we know the hole is 5 nm deep, much more the Co nominal thickness. The Co film is not uniform, which can explain also the non magnetic behavior of the 2 nm Co film at XMCD.

Figure 41: 2nm Co onAlq_3 without barrier: damages are observed.

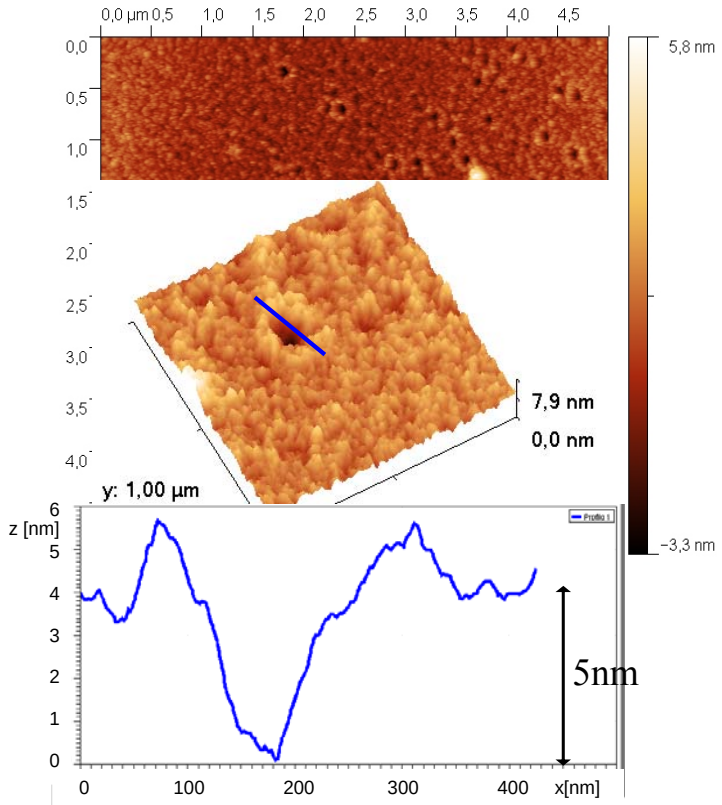

The evidence of the oxide tunnel barrier insertion in between the Co and the Alq_3 is a slightly increased peak to valley roughness and the drastic decrease of the damages density. The former is due to the fact that inserting the tunnel barrier there is an additional layer to the structure: 4 nm of material are nominally deposited on to the organic instead of the 2 nm in absence of the alumina layer. The holes formation is possibly due to the heat of evaporation of the Co, i.e. the

heat which has to be given to let the Co to evaporate and the heat which is emitted during the inverse process, which occurs e.g. during thin film formation.

Spin valves and the decisive role of the tunnel barrier

All the experiments reported show how the insertion of the Al_2O_3 preserves both the Alq_3 and the cobalt. When the tunnel oxide is inserted between the Co and the Alq_3, the organic semiconductor properties are better and the same appears for cobalt. This is ascribed to the fact that Al_2O_3 separates physically the two materials preventing chemical reaction. At the same time the barrier itself deposition do not alter the organic component since the impinging atoms are supposed to thermalize before reaching the sample. In facts a significant deposition is observed also in off-axis position, which indicates a significant scattering between the oxygen molecules in the chamber deposition and the atoms of the plume: more the atom lightness more the scattering, more the thermalization (the O_2 molecular weight is 32 and the Al one is 27).

At the same time the high chemical stability of the aluminum oxide in respect to the cobalt oxide prevents also reaction from the barrier-Co side. Furthermore the oxide buffer layer blocks the Co penetration and improves the formation of a continuum cobalt layer which shows ferromagnetic properties since 2 nm thickness. The optimal thickness for the Al_2O_3 layer is from 2 and 3 nm.

Once the critical interfacial quality has been assured, we can now turn to the electrical properties of the devices, having structure, from the bottom: LSMO/Alq_3/Al_2O_3 (2nm)/Co: Figure 42.

Figure 42: LSMO/Alq_3 (100nm) /Al_2O_3 /Co spin valve magnetoresistance (MR) from 20 K to 315 K; the inset reports the MR at 20 K by varying the Alq_3 thickness.

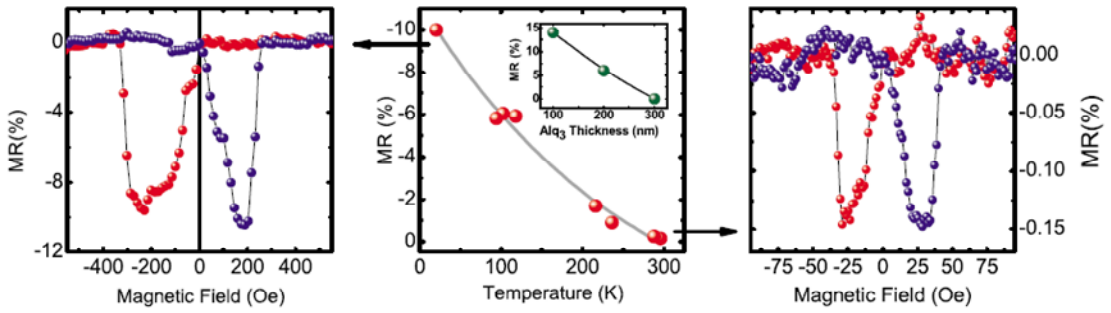

We believe that the structural improvements explained above are crucial to the enhanced device performance. Electrical measurements of the devices (area of 1 mm^2) have been prepared in the cross-bar structure and four points configuration. Samples are inserted in a helium exchange

gas cryostat placed between the poles of a magnetic field for the temperature-dependent electrical measurements.

I-V characterizations of the devices are strongly nonlinear, indicating tunneling injection into organic electronic states. Low-voltage resistances in the range of 1 to 10 kΩ are measured, in agreement with sample geometry and organic layer thicknesses.

Under the application of a magnetic field, the spin-valve effect was detected routinely in the devices. In all cases the low-resistance state corresponds to antiparallel configuration of the two electrodes. The effect is already detected at a voltage bias of 1 mV and persists for applied voltages up to 1 V. The voltage dependence of the MR effect for this kind of devices is slightly asymmetric. The fact that MR is detected already at a voltage bias of 1 mV means that the injection happens in interfacial states without involving a movement of the electrodes Fermi levels, which are pinned due to the high interfacial dipole; the transport occurs in diffusive regime.

While a more detailed investigation of the thickness dependence has yet to be performed, the MR is found to decrease with increasing organic thickness as it is expected for spin/charge injection into the localized interfacial states of the organic semiconductor and subsequent hopping toward the opposite electrode. The further reduction in the thickness of the organic layer must be accompanied by a corresponding reduction in the lateral size of the devices. With the current size, the contribution of the electrodes to the total resistance of the device is high, and therefore a thinner device would have a resistance too low to be measured reliably.

Low-temperature MR values in excess of 10% is routinely obtained on numerous devices with a 100-nm-thick Alq3 layer. Higher MR values detected in other experiments[206] are probably caused by a lower effective thickness of the organic layer compared to the nominal one due to the so-called ill-defined layer. In addition to a much better definition of the geometry, we remarkably achieved operation up to 315 K of Alq_3-based devices.

The Al_2O_3 tunnel barrier is responsible for the extended operation of Alq_3-based spin valves up to 315 K, the improved MR signal and reproducibility and for the well definition of the electrodes coercive fields which leads to a well defined two resistance states even at room temperature[207].

[206] Z. H. Xiong, D. Wu, Z. V. Vardeny, J. Shi, Nature 2004, **427**, 821; S. Majumdar, H. S. Majumdar, R. Laiho, R. Osterbacka, J.Alloys Compd. 2006, **423**, 169.
[207] V. Dediu, L.E. Hueso, I. Bergenti, A. Riminucci, F. Borgatti, **P. Graziosi**, C. Newby, F. Casoli, M.P. de Jong, C. Taliani, Y. Zhan, Phys. Rev. B 2008, **78**, 115203.

Figure 43: MR of the spin valves with oxide tunnel barrier versus temperature – see text or details.

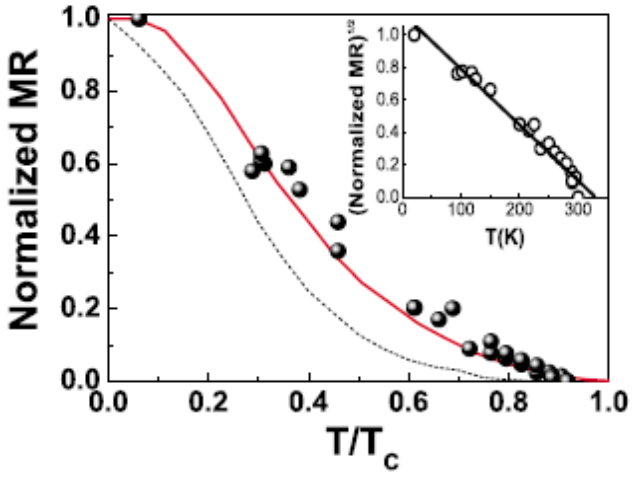

Figure 43 indicates the measured data on our devices containing Al_2O_3 tunnel barrier and fitted by well known temperature dependence of the spin polarization in manganites[208]. It is important to notice that our data lie well above the previously reported data [209] approximately indicated by dashed line (the line represents also the normalized to the density of states spin polarization values[208]).

Thus a significant development of the organic spintronic vertical Alq_3 based nanostructures and devices was achieved by engineering of the top interface via the insertion of an additional insulating tunneling layer between the Alq_3 interlayer and the top ferromagnetic metal electrode. A very similar result was also found for the Atomic Layer Deposition of 2 nm thick Al_2O_3 film on a variety of Self Assembled Monolayers (SAM), where the barrier blocks the top metal electrode penetration leading to tunneling SAM devices on 9 mm^2 areas[210].

[208] J.-H. Park, E. Vescovo, H.-J. Kim, C. Kwon, R. Ramesh, T. Venkatesan, Phys. Rev. Lett. 1998, **81**, 195.
[209] F. J. Wang, C. G. Yang, Z. V. Vardeny, and X. G. Li, Phys. Rev. B 2007, **75**, 245324.
[210] M.J. Preiner, N.A. Melosh, Appl. Phys. Lett. 2008, **92**, 213301.

Interface between ordered organic semiconductor and ferromagnetic oxide.

Pentacene on LSMO – the morphology

The study of the interface between pentacene (Pn) and LSMO is now described, where Pn molecules appear to be ordered and with a defined orientation and a correlation extended up to 300 nm. Despite the wide use of Pn in organic electronics, the study of Pn deposition on ferromagnetic electrode is limited to the case of Pn on cobalt[211] and its utilization in spintronics field is limited to very few reports[212]. Spintronic effects with a spin diffusion length exceeding 200 nm have been reported so far only for devices with LSMO electrodes[213], while no magnetoresistance effects have been detected with cobalt electrodes[214]. Thus available data, although very limited, point out on the relevant role of the ferromagnetic oxide $La_{0,7}Sr_{0,3}MnO_3$ (LSMO), which is by far the most used spin polarized electrode in combination with organic materials[215]. The investigation of pentacene growth on top of LSMO thin films is stimulated by both the importance of LSMO as spin polarized electrode and the significant interest towards utilization of such a high mobility molecular semiconductor as pentacene.

The study of Pn growth on top of LSMO thin films is of interested for both vertical spin valves and planar devices. As a matter of fact the lithography process, necessary in planar technology, can ruin the sides of the defined stripe and the injection could happen from the surface of the film into the semiconductor film deposited on top.

The growth mechanism was studied by the author by AFM, while the interface electronic structure was studied in Linköping by means of near edge x-ray absorption fine structure (NEXAFS) and ultraviolet photoemission spectroscopy (UPS) techniques on *in situ* deposited Pn films on LSMO surfaces prepared in Bologna by the author[216]. These data will be briefly presented at the end of the present section.

Pn was evaporated on LSMO films deposited on STO by Organic Molecular Beam Deposition (OMBD) at a fixed rate of $5 \pm 2 \cdot 10^{-3}$ nm/s and at a base pressure of $2.0 \pm 0.8 \cdot 10^{-8}$ mbar.

---

[211] M. V. Tiba, W. J. M. de Jonge, and B. Koopmans, Journ. Appl. Phys. 2006, **100**, 093707; M. Popinciuc, H. T. Jonkman, B. J. van Waas, Journ. Appl. Phys. 2006, **100**, 093714.
[212] T. Ikegami, I. Kawayama, M. Tonouchi, S. Nakao, Y. Yamashita, H. Tada, Appl. Phys. Lett. 2008, **92** 153304; M. Popinciuc, Ph.D. Thesis, University of Groningen, 2007.
[213] T.Ikegami, *Ibid.*
[214] M. Popinciuc, *Ibid.*
[215] V. Dediu, L.E. Hueso, I. Bergenti, C. Taliani, Nat. Mat. 2009, **8**, 707.
[216] F. Li, Q. Tang, Y. Zhan, X. Liu, M. Fahlman, **P. Graziosi**, V. Dediu, 2009 *submitted*.

The AFM images are taken by tapping mode measurements performed by means of a Nanoscope III microscope by Digital Instrument company and another AFM by Park-Systems; they are both at C.I.M. (Centro Interdipartimentale Misure *"Giuseppe Casnati"*) at Parma University. Tips used are from Mikromash, Olympus and NT-MDT. Data are processed by means of the free software, GNU licensed, Gwyddion[217].

Pn grows in extended islands with molecular steps and a peak to valley size much higher than the nominal thickness. Thus the growth time will be used instead of the thickness, especially for growth model application. The time is expressed in minutes (min).

LSMO films used as substrate for pentacene growth were 5 - 20 nm thick. Pn films were deposited at substrate temperature of 25 °C and 60 °C for a deposition time ranging from 5,5 (1 nm nominal thickness) to 55 min (20nm nominal thickness). We experienced also a deposition at 0 °C, but the resulting thickness was far from the others and it wasn't used for analyzing the growth mechanism. The film growth was conducted with the help of author's coworkers Carol Newby, Mirko Prezioso and David Brunel, while the author is grateful to prof. Massimo Ghidini for the author's "initiation" to AFM measurements. The analysis is carried on following the surface and thin film growth concepts described in the first chapter.

Table 3: samples list

Temperature	Nominal thickness	Deposition time
RT	1 nm	5'30''
RT	3 nm	17'30''
RT	6 nm	26'
RT	20 nm	55'
60 °C	1 nm	5'30''
60 °C	3 nm	16'
60 °C	7 nm	37'
60 °C	20 nm	44'

Now let's have a look at the images taken by AFM. We start observing the micrographs measured for the films of several thicknesses grown at room temperature and 60 °C. Each film has a "twin" deposited on native silica with the objective to compare the two substrates *at the same* deposition conditions: the goal is to study the growth on LSMO, the sample on silicon are simple satellite samples.

Figure 44 represents the morphology of the thinnest film of Pn deposited on LSMO. One sees very large structures with features, vertical scale, and roughness (~0,6nm), different from the

[217] www.gwyddion.net.

manganite under-layer. This could be a proof of the full coverage of the surface by the molecules and of a low nucleation barrier.

Figure 44: Two micrographs of Pn deposited on LSMO at RT for 5,5 min.

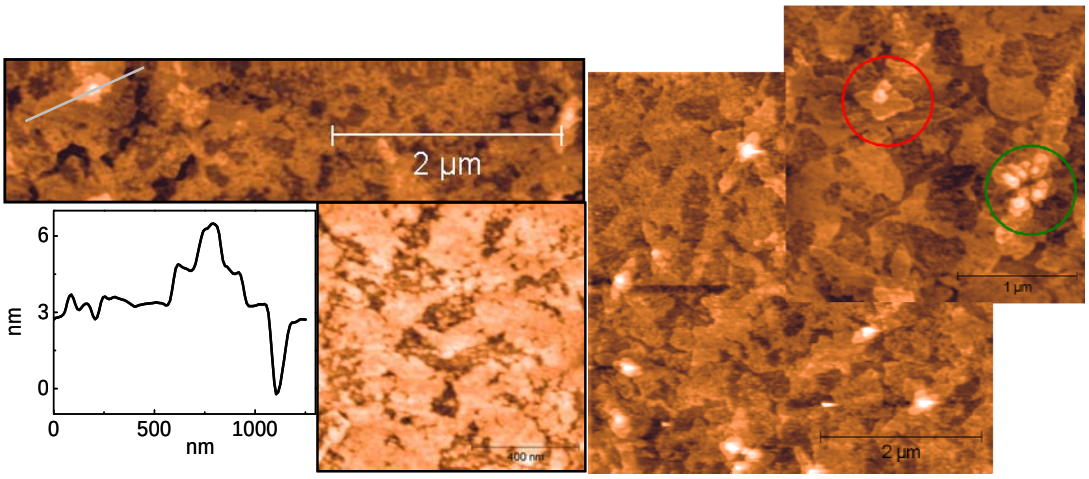

A clear and structured morphology is not defined: the first molecules possibly are in random orientation, as probed also by UPS: the valence band structure of the pentacene in the ultraviolet photoemission spectra appears only after the deposition of 2,2 nm of Pn on the LSMO surface. The first 2,2 nm molecules are thought to be disordered[218]. A similar amorphous wetting layer was found also in Pn films deposited on $BaTiO_3$[219], here it is called interfacial layer and is found only for certain temperatures (-65°C and +75°C), not for RT deposited films. This picture is possible also in the surface represented in Figure 44. The first molecules are randomly placed; on top of this layer a well ordered film start to nucleate. The ordered islands developing on the first disordered layer are characterized by regular 1,4nm high steps. This is the height of a monomolecular step: the ordered islands grow in a layer-by-layer mode, but in an anisotropic shape, which is conserved up to 20 nm thick films. Islands grow following a certain direction, as shown by the green circle in Figure 44, where the red circle lightens an already happened coalescence. We observe ordered islands already at a nominal coverage of 1 nm while the valence band features peculiar of pentacene appear only at 2,2 nm in UPS spectra[218] when a full coverage is achieved.

It appears clear that these ordered islands grow following a preferential orientation (see the green circles in Figure 45): each single island appears to be elongated in a certain direction. Pn molecules diffuse on the LSMO surface isotropically, but when they fall onto a Pn island, their diffusion becomes anisotropic, molecules accumulate along a certain direction, then an abrupt

[218] F. Li, **P. Graziosi** , Q. Tang, Y. Zhan, X. Liu, V. Dediu, M. Fahlman 2010 *submitted Phys. Rev. B* .
[219] R. Ruiz, L.C. Feldman, R.F.Haglund Jr., R.A. McKee, N.. Koch, B.A. Nickel, J. Plaum, G. Scoles, A. Khan, 2002, Materials Research Society Symposium.

jump takes place. The anisotropic diffusion of the molecules on the first Pn layer is due to an anisotropy in the molecule-molecule interaction, intrinsic in elongated rigid rod-like molecules such as pentacene, while the molecule-LSMO interaction seems isotropic. The asymmetry in the molecular potential could be ascribed to the orientation of the molecules on the LSMO surface[218]: if the molecules follow a certain direction, also the potential energy does. This leads to an anisotropy in the interaction which reflects in an asymmetry in the Ehrlich-Schwoebel (ES) barrier: when a molecule comes to the edge of a terrace, a lower density of unsaturated bonds prevents it going over the edge[220].

Figure 45: Pn films deposited on LSMO for 17,5 min (left) and 26 min (right).

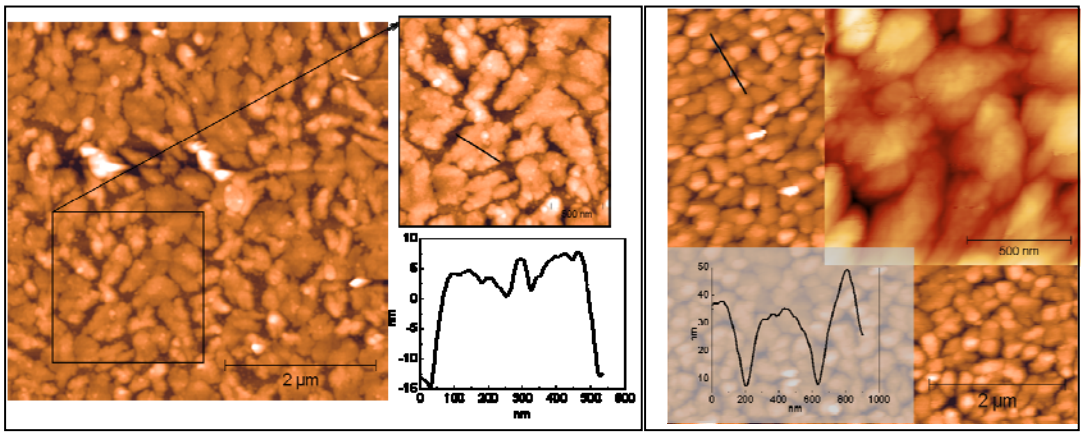

Increasing the deposition time to 17,5 min the surface aspect changes and the well ordered features of the thinnest films are lost. Why it happens is not clear, but it is thought to be caused by a decreased mobility and a faster nucleation[221]. The first Pn islands nucleated on LSMO surface constitute a sort of pentacene substrate for successive molecules, which impinge the sample falling on other molecules and not on the LSMO. As a consequence new processes happen (like intermixing) and the atomistic processes have different characteristic energies and times. Even a change from a diffusion driven growth process to another one led by sticking and/or by intermixing can take place. This change can include increased nucleation rate and decreased desorption, possibly due to the increased "affinity" between molecules and molecules in respect to molecules and oxide. Note that this increased nucleation rate and decreased desorption was found for Pn/PMMA, in comparison with Pn/SiO_2 [222].

As a consequence of the above described phenomena, the Pn film evolves by nucleation of smaller islands up to the coarsening of the film, when island size grows again and island density decreases. Also the surface width (the maximum vertical range) increase dramatically. This is

[220] M. Lagally and Z. Zhang, Nature, 2002, **417**,907.
[221] S. kowarik, A. Gerlach, F. Schreiber, J. Phys.. Condens. Matter, 2008, **20**, 184005.
[222] S. Pratontep, F. Nüesch, L. Zuppiroli, M. Brinkmann, Phys. Rev. B, 2005, **72**, 085211.

consistent with what Kowarik and coworkers observed[223]: when the Pn film thickness exceeds a certain thickness, the growth shifts from layer-by-layer to three-dimensional with a significant increase in the surface width[224]. In Figure 46 the ordered structure seems to be missed, but it is recovered in the thicker films (figure 47). This suggests that, after an initial stage, the three-dimensional islands growth evolves in a *simultaneous multilayer fashion*, where the layer-by-layer mode is restricted to each single island. So the anisotropic features of the thinnest films is kept.

Figure 46: 55 min Pn film deposited at room temperature on LSMO

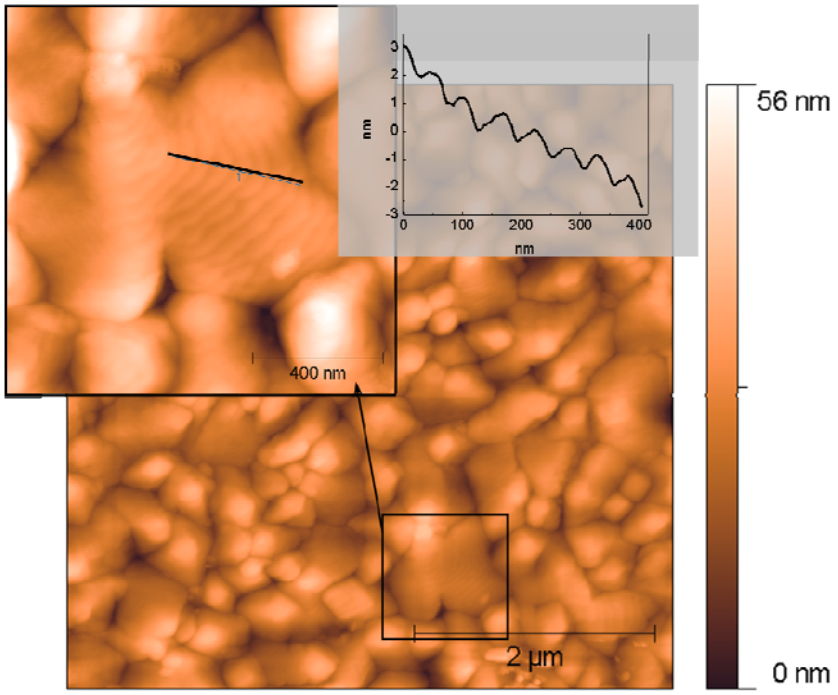

In the following the morphology evolution with the thickness for films deposited at 60°C is reported. Figure 48 catches the early islands. There are two morphologies. Large, round and flat islands and others, ragged ones grow together but with a different growth rate. The ragged islands seem to grow faster. This is perceived by involving the molecules diffusion: there are region, or islands, where the ad-molecule diffusion is easier, or isotropic. The shape becomes less ragged and the vertical growth is slow.

A clear difference in respect to the room temperature condition is that at 60°C the first islands are much wider than those grown at room temperature and the amorphous wetting layer seems to be absent. It is not possible to assert that the interisland regions resemble the LSMO, but the differences with the room temperature case, together with the low nominal thickness (1 nm) lead to this conclusion. If so, the molecules are not randomly placed on the manganite surface, but

[223] S. kowarik, *et al.*, *Ibid.*
[224] S. Kowarik *et al.*, *Ibid.,* §3.1.

stand up, as deduced from the step height in the line profiles. The first two steps are distinct and about 1,4 nm high, while the following layers, up to a 12 nm height, seem not so well ordered, suggesting the missing of the layered growth, in analogy with the room temperature case. Moreover the coverage seems to be lower. As observed by Brinkmann and co-workers[225], the minor coverage and the ragged shape of the island together with the change in the molecules orientation on the substrate can be ascribed to a change in the energy landscape felt by the molecules. As a matter of fact the diffusion on the surface and the desorption are competing processes: at approximately 60°C the desorption becomes dominant. The straight lines are a reminiscence of the STO substrate used for the deposition of the LSMO films and are due to the substrate cutting. The morphology of the interisland region resembles the LSMO. Thus the LSMO coverage is not full, differently from the RT case; the cause is possibly the desorption.

Figure 47: Images of Pn deposited on LSMO at 60°C for 5,5 min and of the interisland region, which seems much like LSMO. The line comes from the substrate, possibly as a consequence of the cleavage.

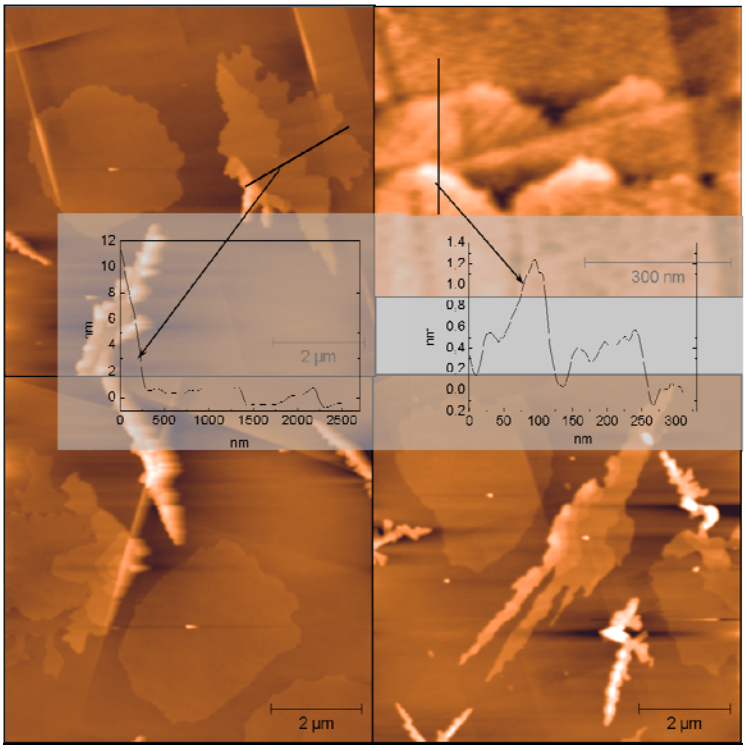

In the next steps the general evolution mimics that at room temperature. An important difference between the two deposition temperatures consists in the fact that in the 44 minutes deposited films the morphology becomes lamellae like, suggesting the onset of a thickness dependent transition[226].

[225] S. Pratontep, F. Nüesch, L. Zuppiroli, M. Brinkmann, Phys. Rev. B, 2005, **72**, 085211.
[226] T. Jentzsch, H. J. Juepner, K.W. Brzezinka, A. Lau., Thin Solid Films 1998, **315**,273.

Figure 48: 16 min deposited Pn film deposited on LSMO at 60°C temperature.

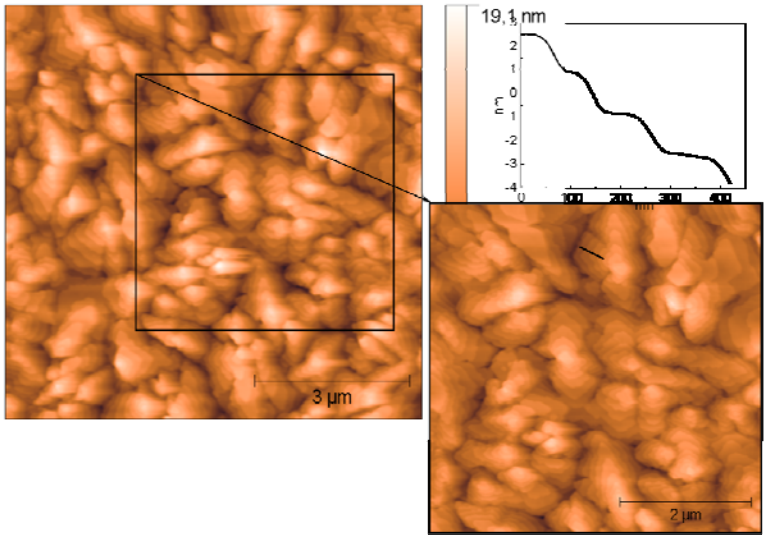

Figure 49: 37 min (left) and 44 min Pn film deposited at 60°C on LSMO.

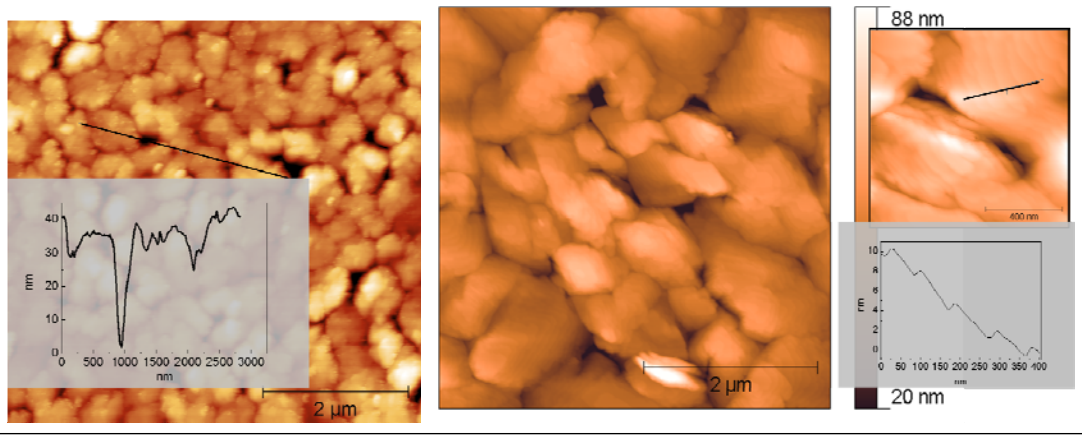

It is noticeable that 30 °C grown film topography features terraced islands with regular 1,0 ± 0,2 nm high steps, while films grown at 60°C show lamellar morphology featuring 1,0 to 2,5 nm high steps, as sketched in Figure 50c,d. Here films grown at 30 °C and 60 °C are compared with films grown at the same temperature on the bare $SrTiO_3$ substrate. Similarly to the pentacene deposited on LSMO, a dramatic effect on island size is detected. The morphology and the steps height (1,5 nm) don't change with growth temperature, differently from what happens for pentacene molecules deposited on LSMO films. This can be ascribed to a smoother morphology (the STO substrate is smoother than the LSMO film deposited on top), but also to a different interfacial chemistry which affect the dispersive interactions of the early layers, and so of the whole film. Since the different deposition time between the film represented in Figure 50c) and d), the different island size seems to be a consequence of the increased time of the deposition. Indeed

features of a coarsening transition aren't present: the larger islands could result from the evolution of largest nuclei. This is supported by a comparison between the time evolution at room temperature (Figure 44 and Figure 46) and at 60°C (Figure 47 and Figure 49).

Figure 50: Images of pentacene islands grown at room temperature (55 min deposition time) (a) and 60 °C (44 min deposition time) (b); c) pentacene thin film deposited on strontium titanate (STO) at room temperature for 17,5 min (roughness~1,5 nm) and d) at 60°C for 37 min (roughness~1,9 nm). The different scale takes count for the different islands sizes.

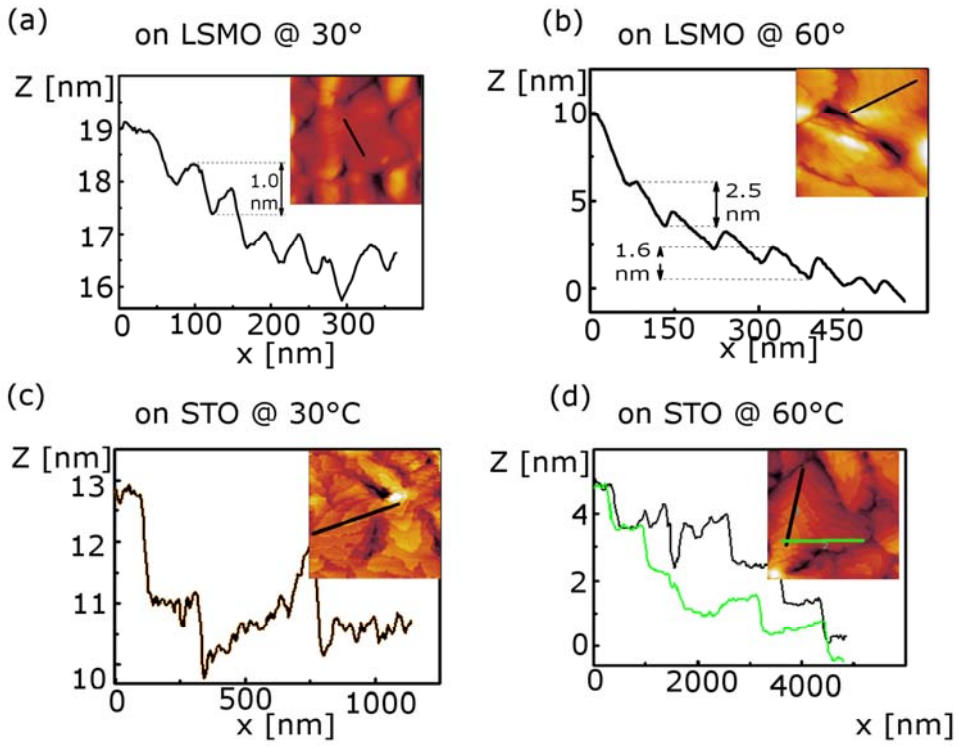

When the same amount of Pn is deposited on native silica, the surface is radically different, featuring a lot of little islands nucleated on top of it. This is due to a lower mobility of the ad-molecules. The general trends observed for Pn deposited on LSMO is kept on SiO_2: increasing the deposition time the island size initially increases, then decreases; increasing the temperatures the island size increases. The morphological transition is absent.

Figure 51: Pn deposited on Silica at room temperature for the written time.

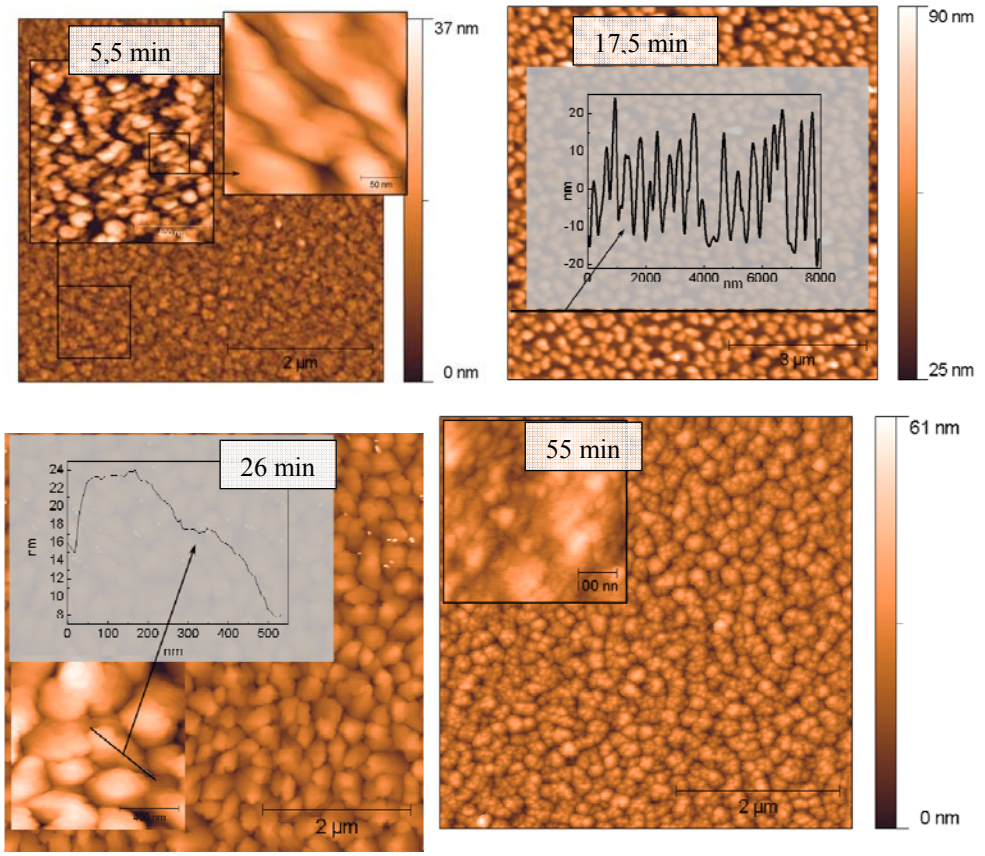

Figure 52: 37 min (left) and 44 min (right) deposited Pn thin films at 60°C on native silion oxide.

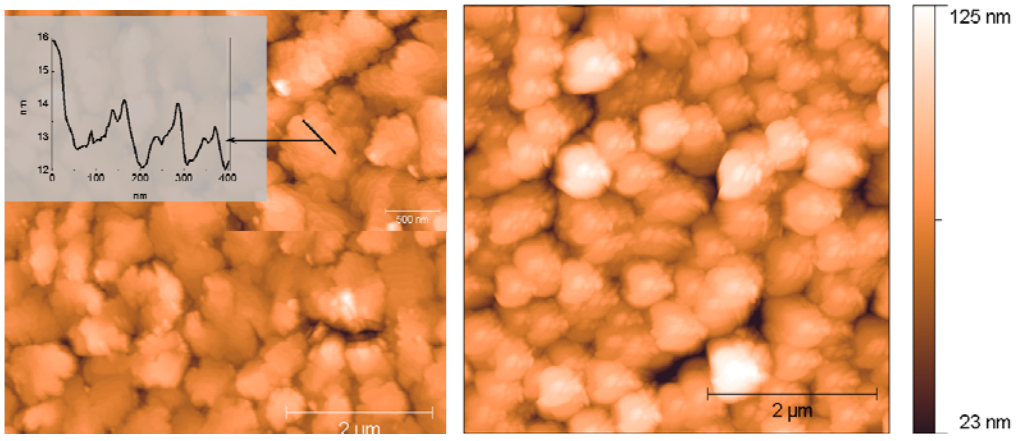

Growth model for Pn on LSMO

Increasing temperature deposition, islands size increases and islands density decreases drastically. This can be the signature of a strongly temperature activated diffusion mediated

growth, but also can indicate a change in the dominant growth processes, from a diffusion to an adsorption dominated one. We perform a more accurate analysis following the concepts described in the introduction paragraph on the thin film growth.

Each image is analyzed by means of the statistical quantities related to the surface corrugations: rms roughness and HHCF. The height-height correlation function are computed along the fast scan direction and mediated for each line of the sample. The growth is perceived in the mound-like frame[227] instead of the classical self-affine picture. This is supported by the HHCF profile analysis[228], as one can deduce by the HHCFs reported in Figure 53. The HHCF for two films of Pn on LSMO; one deposited at room temperature and the other deposited at 60°C for 26 min and 37 min respectively; they are shown as examples, in order to illustrate what information can be extracted from HHCF. The correlation length ξ is a mean measure of the mounds size, ~ 230 nm for the RT deposited film and ~ 320 nm for the 60 °C one; the second peak signed by an arrow correspond to the lateral size of the bigger mound in the middle of the image of the RT sample (~ 650 nm). From an analysis of the region near zero, far from ξ, the roughness exponent α values are extracted.

Figure 53: Height-Height Correlation Functions of a couple of samples, as in the text.

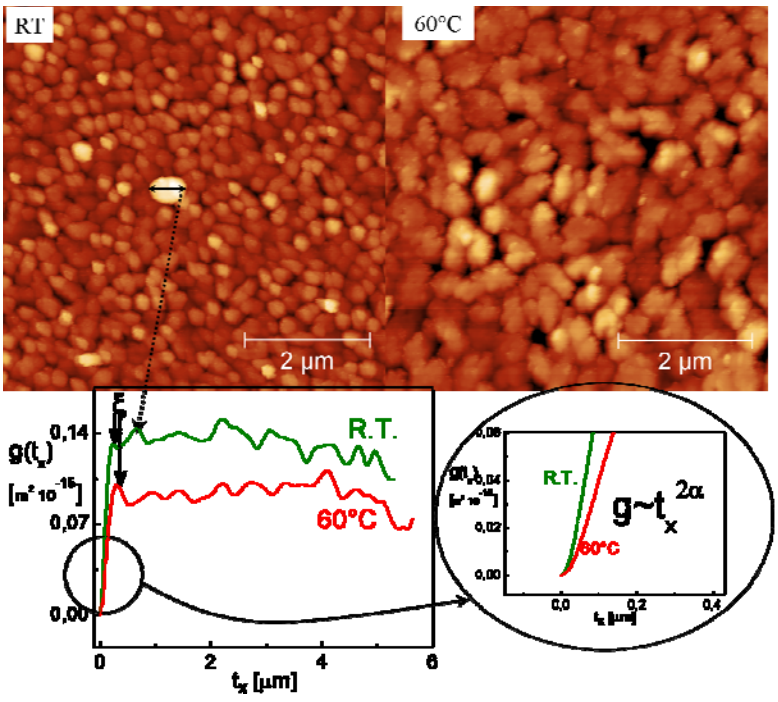

[227] J. W. Evans, P. A. Thiel, M. C. Bartelt, Surf. Sci. Rep. 2006, **61**, 1.
[228] See the paragraph 3.4, p. 15, and fig.8 of Evans *et al. ibid.* .

About the correlation length as function of both thickness and temperature, Figure 54 presents the data. Due to the morphology, it is quite hard to speak about thickness, so the scaling concepts are tested by using the deposition time as parameter. Since the film thickness is assumed as linearly increasing with the time, the extracted exponent will be the same.

Figure 54: Correlatin Length versus thickness.

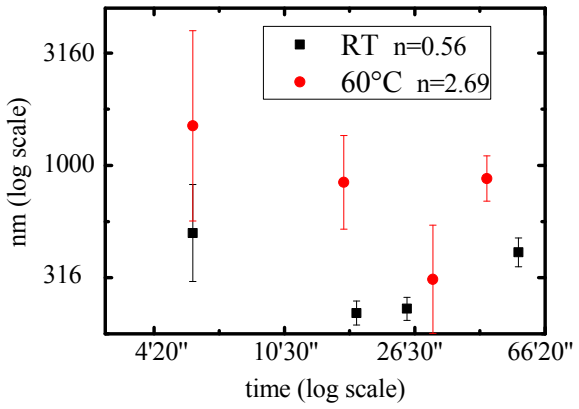

The power law trend predicted by the theory[229] is not observed. The reason is the same addicted above for the roughness versus thickness behavior. At small thickness the correlation length, i.e. the islands size, is influenced by the bottom LSMO. It includes higher diffusion, lower interaction, small nucleation rate, eventually higher re-evaporation rate. Moreover, if the desorption is happening, it will be more efficient for low coverage and higher temperature, so the critical thickness after which the substrate effects vanish are different. As a matter of fact the trend $\xi \approx t^n$ is observed after 17,5 min films at RT and after the 37min one at 60°C. These data are not sufficient for the estimation of the coarsening exponent $n=1/z$, where z is the dynamic exponent in the traditional scaling concepts pictures; anyway the fitting results for these parts of the deposition times is written in the figure. From these data one obtains z values of 1.8 for RT films and 0,37 for 60°C ones. By comparing these values with those of theoretical models[230], it is found that the growth is adsorption limited.

From the initial part of the HHCF curves one obtains the roughness exponent α, which gives insight into the height-height relationship. In the following table the measured values for α are reported for the two temperatures. It is quite hard to find a trend, we can observe that the roughness exponent decreases increasing temperature and increases with the thickness. Since the roughness exponent contains information about the short range roughness, this indicates that the

[229] Evans *et al*. *Ibid.*
[230] J. Krim and G. Palasantzas, J. Mod. Phys. B 1995, **9**, 599.

surface becomes more ragged with the thickness and less ragged with deposition temperature, probably due to diffusion variation. α values are measured in the translation range 0 - 40nm, in order to satisfy the requirement $t << \xi$, considering the finite pixel size and lateral resolution of the AFM probe. In an image of 512x512 pixels and 5 μm x 5 μm each pixel is 9,765 nm, and smaller details cannot be resolved. But in smaller images, for example 0,5 μm x 0,5 μm, each pixel represents less than 1 nm. In this case the data reliability is limited by the lateral resolution of the tip, which is 7 nm at best[231].

Table 4: roughness exponent extracted for the samples of Table 3.

Temperature	Deposition time (min)	α
RT	5,5	0,67±0,5
RT	17,5	0,76±0,04
RT	26	0,78±0,01
RT	55	0,80±0,03
60°C	5,5	0,62±0,03
60°C	16	0,75±0,06
60°C	37	0,94±0,01
60°C	44	0,77±0,01

From Table 4 we can make some consideration on the growth mechanism by comparing the roughness exponent computed from AFM micrographs with those extracted from models. A growth model which considers desorption dominating over diffusion, like the Kardar-Parisi-Zhang model[232], features α=0,385, while for the diffusion limited growth along preferential orientations α=2/3[233]. The roughness exponent reaches unity when the diffusion is isotropic and totally dominant ("pure" diffusion mechanism By comparing these values with those of theoretical models). Thus, from Table 4, we assert that the Pn growth is diffusion limited. This finding contrasts with the previous result of an adsorption limited scenario coming from the correlation length data; from the other hand such a mechanism requires lower α values[232]. Due to the scattered behavior of ξ the result from the roughness exponents, i.e. a diffusion limited growth, seems more reliable. This conclusion requires nevertheless additional confirmation, as no models exist so far which are able to take into account all the processes involved when organic molecules are deposited on inorganic substrate.

[231] See technical data about AFM probes, e.g. from www.ntmdt.com or http://probe.olympus-global.com.
[232] M. Kardar, G. Parisi, Y. Zhang, Phys. Rev. Lett., 1989, **62**, 889.
[233] J. Villain, J. Phys. I, 1991, **1**, 19.

Looking for a unique parameter able to describe the film surface, the scaling exponents and fractal dimension concepts seem most appropriate for the description of surface irregularity, smoothness and raggedness[234]. The fractal dimension D_f estimates the average irregularity of the surface: for a smooth surface the fractal dimension is 2,00. D_f is computed by means of the simple cubing counting algorithm[235]. For our samples D_f does not vary with the thickness of the film and it is 2,3 ± 0,2 in films deposited at room temperature and 2,2 ± 0,1 for 60 °C grown ones. Further extensive and careful device characterizations are necessary in order to find out threshold D_f values compatible with high device performances.

In the following a comparison with the Random Deposited (RD) model is made, where the thickness of a single molecular layer (d) is considered 1,6 nm. The RD model is computed as a function of time, so we have $W = \sqrt{dR}\sqrt{t}$, where W is the surface width, R is the deposition rate, t is the growth time. The uncertainty on the rate causes a splitting of the RD model which conserve its slope ½ (it is a double logarithmic plot), but is vertically shifted giving rise to a sort of RD region. The comparison is shown in Figure 55.

Figure 55: Comparison between rms roughness versus thickness D for the two temperatures and the pure Random Deposition model. W stands for surface width, as described in the text.

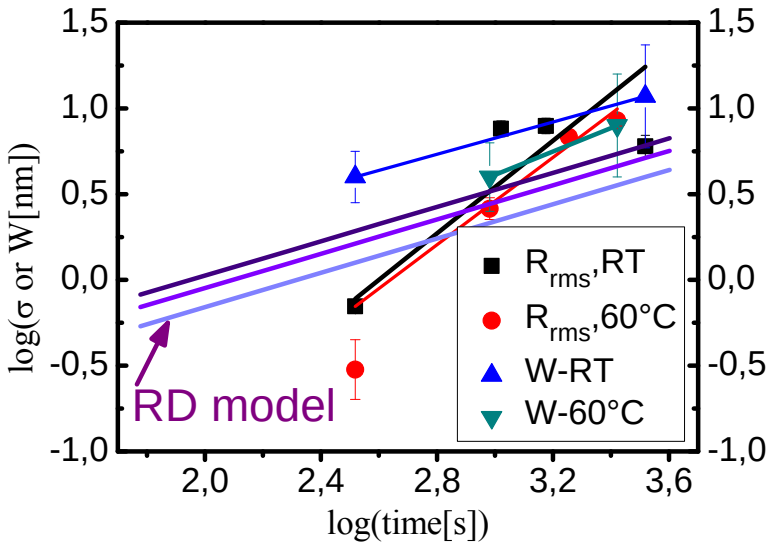

[234] W. Zhan, A. Zosch, Fresenius J. Anal. Chem. 1997, **358**, 119; F. Varnier, A. Llebaria, G. Rasigni, J. Vac. Sci. Technol. A 1990, **9**, 583; F. Varnier, N. Mayani, G. Rasigni, J. Vac. Sci. Technol. A 1988 **7**, 1289; W. Zhan, A. Zosch, Surf. Surf. Anal. 1997 **25**, 488; J. Nogues, J. L. Costa, K. V. Rao, Physica A 1992, **182**, 532; A. Van Put, A. Vertes, D. Wegrzynek, B. Treiger, R. Van Grieken, Fresenius J. Anal. Chem. 1994, **350**, 440.

[235] www.gwyddion.net/documetation.

At first we note that the roughness of our pentacene films stays (except for the first data) above the RD model, on the contrary of what observed for diindenoperylene (DIP) films[236]. This could be caused by the LSMO roughness. Nevertheless, as σ values for 1nm thick films are lower than model data, and a rapid roughening occurs after 3nm, a sort of critical thickness exists, below which the Pn-LSMO interaction is relevant. Above this thickness, the effect of the substrate vanishes and the interaction between Pn incoming-molecules and Pn deposited-molecules becomes dominant. At this stage intermixing and high nucleation rate occurs giving rise to a fast increase of the interface width[237]. These processes are not included in the RD model. Anyway the trend of the roughness evolution towards a "stabilization" on the values closed to that predicted from the RD model is observed, but more data are needed to confirm this.

The rapid roughening is supported also by the scaling law obtained:

$R_{rms} = 3 \cdot 10^{-4} t^{1,4}, RT(296K)$

$R_{rms} = 5 \cdot 10^{-4} t^{1,3}, 60°C(333K).$

The rapid roughening, i.e. a roughening faster than the RD roughening, is conceptually ascribed to the asymmetric sticking coefficient at step edge[238], which is a consequence of the intrinsic asymmetry in the intermolecular potential due to the rigid rod shape of the Pn molecule.

Assuming that the prefactor of the power law can be expressed by $\sqrt{(1-\theta_c)d}$. The coverage at which the second layer starts to nucleate approximates the unity, that is 0,999999943 and 0,9999999843 for RT and 60 °C respectively, as estimated from Figure 55 and visually confirmed by Figure 44 for RT deposited Pn, while the situation at 60° C does not agree with this result in Figure 47.

An important question arising at this stage is whether the rms roughness efficiently describes the surface width. Figure 56 reports four profiles for films deposited at RT (5,5 min and 55 min) and 60°C (16 min and 44 min).

It appears that peak to valley amplitude is a more appropriate parameter. Such values are computed as a one-dimensional roughness parameter R_t by the Gwyddion software according to the standards ASME B46.1-1995 and ISO 4287-1997. The values computed for many scan lines of these films are presented by the plots labeled W in Figure 55 and showing power law behaviour:

$W = 0,26 \cdot t^{0,47}, RT(296K)$

$W = 0,04 \cdot t^{0,68}, 60°C(333K).$

[236] J. Krug, Physica A, 2004, **340**, 647.
[237] S. kowarik, A. Gerlach, F. Schreiber, J. Phys.. Condens. Matter, 2008, **20**, 184005.
[238] Look at § 4.1.8 in J. Krim and G. Palasantzas, , J. Mod. Phys. B 1995, **9**, 599.

Figure 56: Mounds profile from selected sample deposited at room temperature and 60°C.

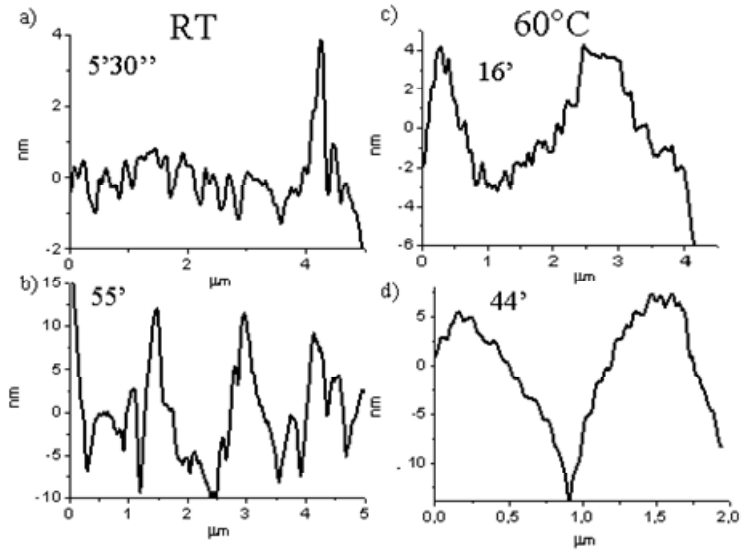

First of all we must note that the first layer pattern does not persist (see the horizontal scale): during the growth the distance between mounds changes and they become smaller in size. The persistence of the pattern is an indication of a top terrace nucleation, where the diffusion coefficient on top of the terraces is much bigger than those for edge and interlayer diffusions[239]. Thus we can assert that we are not in a presence of a pure Random Deposition system, but several other effects are active, like intermixing, interlayer diffusion, increased nucleation rate, re-evaporation.

Growth mechanism of pentacene nucleation on LSMO surfaces

In order to have a deeper insight into the growth mechanism, the effect of the substrate temperature was studied quantitatively by means of the stable island density *n*. It is exponentially proportional to the combination of several energy barriers to microscopic process in an Arrhenius type fashion. 3 nm nominal thick films have been deposited at the substrate temperatures of 45°C, 60°C, 75°C. All the islands in the 3 nm thick films micrographs are considered stable due to their many-molecule size.

[239] J. Krug, Physica A, 2002, **313**, 47.

Figure 57: Pn film deposited for 12 min at an LSMO temperature of 45°C

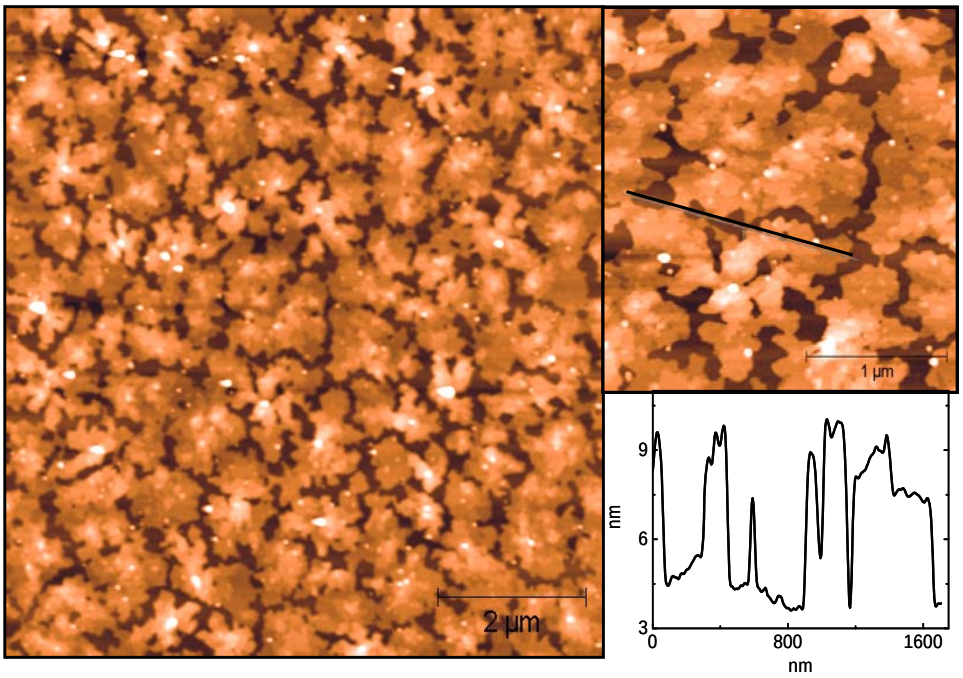

Figure 58: Pn thin film deposited on LSMO for 12 min at 60°C.

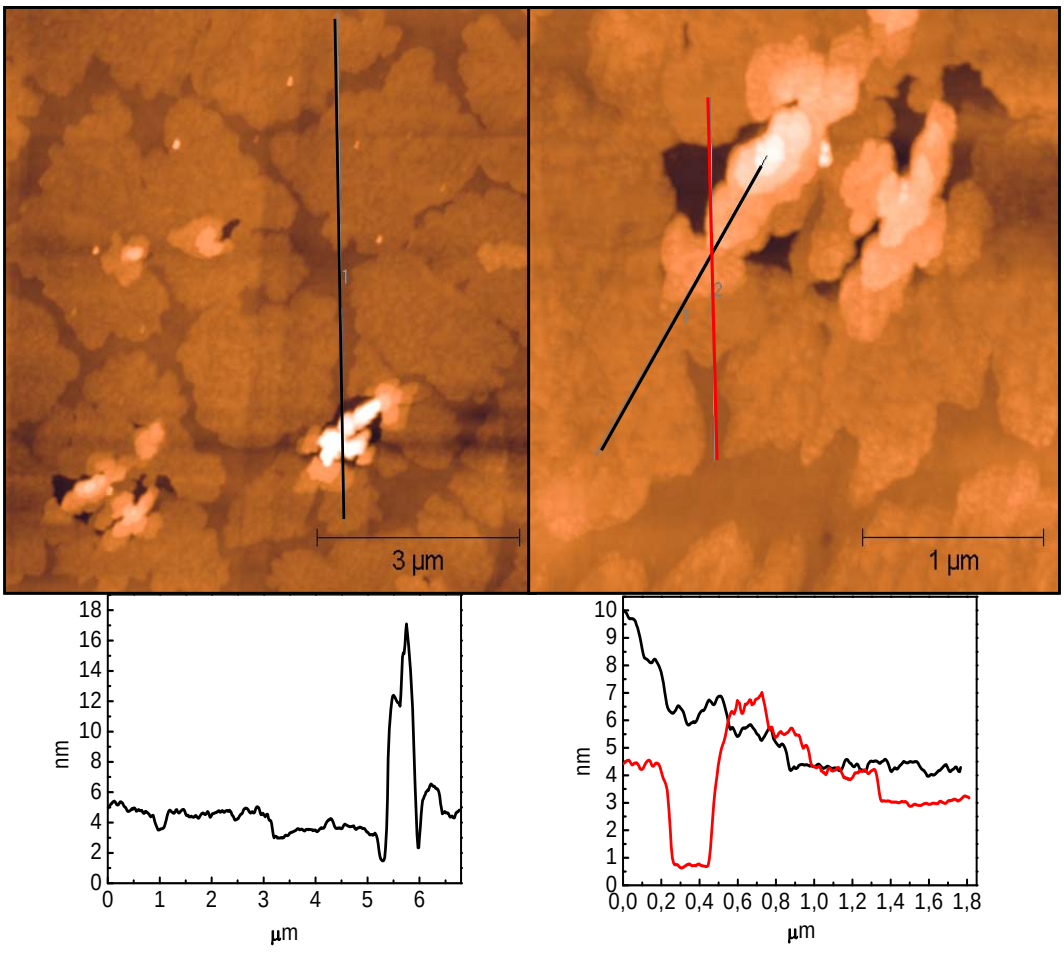

Figure 59: 75°C deposited Pn film, 12 minutes.

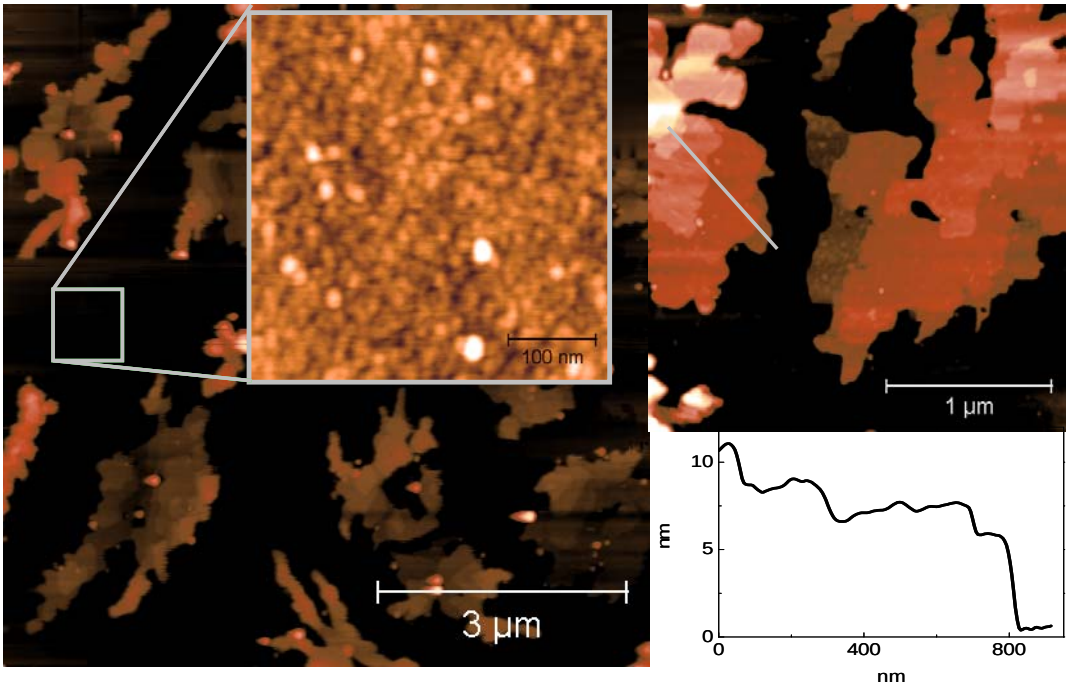

Increasing deposition temperature, the size of the Pn islands is observed to increase. When the molecules are deposited at 30°C they cover isotropically the substrate and the subsequent diffusion on the first molecular layer forms anisotropic islands, as discussed above. When the substrate temperature increases to 45°C the picture changes. The islands become bigger in size and more separated.

This trend is accentuated by increasing the substrate temperature to 75°C. In these films the Pn islands are quite far from each other. Thanks to the interisland separation, the interisland region could be imaged by AFM (Figure 59, inset). It looks similar to LSMO morphology, with a mean peak-valley roughness less than 1 nm. Islands size in these thin films is larger than in thicker ones. The first islands will constitute a sort of pentacene substrate for the following molecules which will form the smaller islands we see in thicker films. This different size comes from the difference in the LSMO-molecule interaction with respect to the molecule-molecule one.

These images lead us to formulate some consideration on the surface coverage. If the question about the surface coverage seems still open for RT grown films, it appears clear that the coverage is not complete when pentacene is deposited at 45°C. This means that a ΔT of about 15°C is enough to break the interaction with the substrate which seems very weak. This demonstrates a dramatically increased surface mobility and, possibly, a different number of critical molecules - i.e. the minimum amount of molecules giving nuclei stable against dissociation - with

respect to the 30°C situation. There isn't any wetting layer and the film nucleates with several molecules height steps and abrupt jumps, as reported in Table 5.

Table 5

Deposition temperature	1st step height [nm]	Inclination(1)	2nd , 3rd , 4th steps [nm]
30°C	1,5 ± 0,2	20°	
45°C	3,5 ± 0,6	0°	1,7
60°C	3,5 ± 1,0	0°	1,2 ; 1,4
75°C	4,6 ± 0,4	25°	1,5 ; 1,5 ; 1,7

(1) it is the angle between the molecule and the normal to the surface, assuming that a molecule extends for 1,7nm in length, and thinking to multi-molecular steps without flat lying molecules, as explained in the text.

The steps height (either the first step or the following ones, if any) is evaluated by means of the height distribution function in order to rule out possible misinterpretation of scan profile. As also reported in literature[240,241] the first step is sometimes higher than just one molecule; in particular it was found to be 2,5 nm and 2,0 nm. In the former this was attributed to the interfacial trapped water, while in the latter it was ascribed to a flat lying molecules layer between the substrate and the first standing molecules. Our vacuum conditions are better than in 240 and we performed the annealing of the substrate at 250°C for 30 min before the Pn deposition. This allows us to exclude the presence of water. As discussed above about the surface coverage, for $T \geq 45°C$ there is not a flat lying molecule layer ruling out the second explanation.

In order to explain our results we propose a different explanation. In 30°C deposited films the first step is monomolecular, while in films grown at 45 °C , 60 °C 75 °C the first step is several molecules height. The following steps are monomolecular. It is remarkable that the 20° angle found in room temperature deposited film is in excellent agreement with what found by Near-Edge X-ray Absorption Spectroscopy (NEXAFS) in Pn films deposited on LSMO[242]. Increasing the deposition temperature to 45°C the angle between the long axis of the molecule and the substrate decreases confirming that something changes in the growth mode.

So the first steps are perceived as constituted of vertically standing up molecules, up to three in 75°C grown films. This picture is similar to what described by Verlaak and coworkers[243] for weak molecule-substrate interactions. They performed a theoretical study for three OSCs (one of which was pentacene) grown on inert substrates. A detailed analysis was applied, considering the

[240] S. Wo, B. Wang, H. Zhou, Y. Wang, J. Bessette, R.L. Headrick, A.C. Mayer, G. Malliaras, A. Kazimirov, J. Appl. Phys. 206, **100** 093504.
[241] S.D. Wang, X. Dond, C.S. Lee, S.T. Lee J. Phys. Chem. B 2005, **109**, 9896.
[242] F. Li, Q. Tang, Y. Zhan, X. Liu, M. Fahlman, **P. Graziosi**, V. Dediu, 2009 *submitted.*
[243] S. Verlaak, S. Steudel, P. Heremans, D. Janssen, M.S. Deleuze, Phys. Rev. B 2003, **68**,195409.

inner pentacene film energetics (the molecule-molecule interaction along different special direction and crystallographic axis) and using the molecule-substrate interaction as parameter. Following the definitions used in the theoretical work, our growth mode is 2D with a few 3D mounds for the whole temperature range. The density of 3D mounds increases with temperatures and becomes about 1/3 of the 2D islands at the substrate temperature of 75°C. Our morphological data fit very well with the figures 3b and 4 of the work by Verlaak and co-authors. This picture is relevant for aromatic OSC thin film growth on oxide surfaces. Due to the low LSMO-molecule interaction in respect to the molecule-molecule one, Pn molecules stand on, maximizing the contact between each other and minimizing the contact with the LSMO surface. As represented in fig. 2b of the cited work by Verlaak, the formation of a first multi-molecular step is possible, especially if the tilt angle is quite high. The latter provides a good overlap between orbitals of different molecules and weak interaction with the substrate. Figure 60 sketches a possible Pn molecules nucleus.

Three molecules appears to be a reasonable number giving also stability against desorption, as we will show in the next section. One should notice that, up to now, such a wide and flat morphology was obtained only on SiO_2 and only when the growth was assisted by means of a supersonic gas flow at high molecule energy, i.e. high surface diffusivity[244]. This is another proof of the low molecule substrate interaction when pentacene grows on LSMO. We think this is related to the significant difference in the surface energies due to weak interaction with LSMO and strong Wan der Waals self-organizing interaction between molecules.

Figure 60: Pn nucleus.

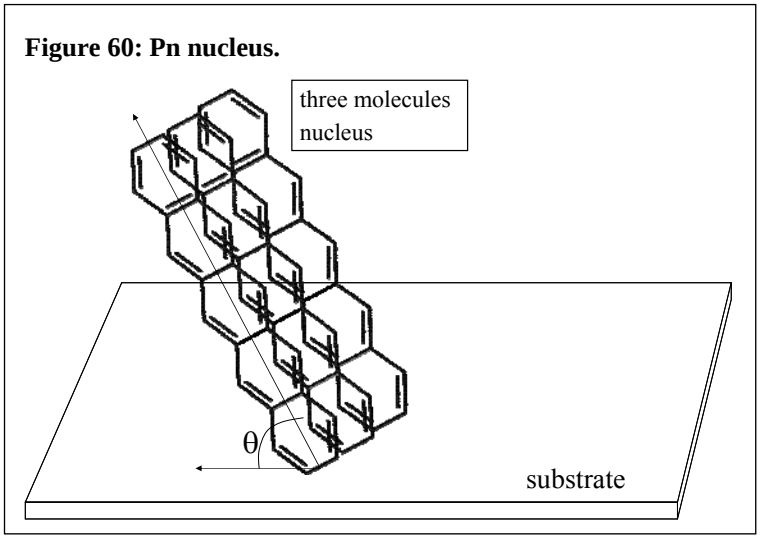

[244] T. Toccoli, A. Pallaoro, M. Tonezzer, N. Coppedé, S. Iannotta, Solid State Electr. 2008, **52**, 417;
Y. Wu, T. Toccoli, J. Zhang, N. Koch, E. Iacob, A. Palloaro, S. Iannotta, P. Rudolf, Appl. Phys. A 2009, **95**, 21.

Figure 61: 40°C Pn film on LMSO.

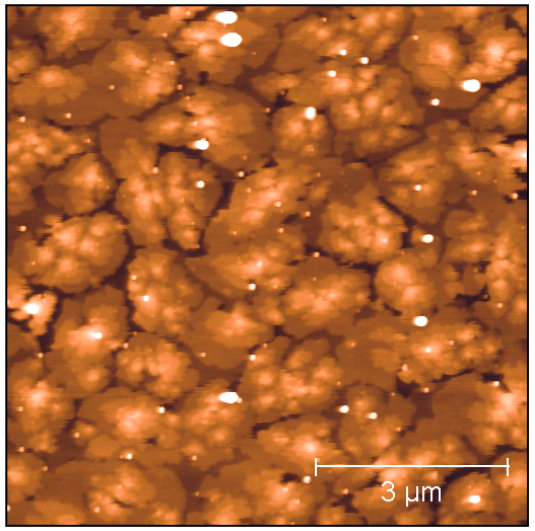

We observe changes in the substrate/molecule interactions at 45°C. Trying to plot island density versus substrate temperatures (data reported in the following) we need to exclude the point at room temperature *or* the point at 45°C in order to have a exponential plot. Thus a possible transition in the growth mechanism of Pn seems to occur around 45°C. In order to get better insight the nearby temperatures of 40°C and 50°C are investigated.

Analyzing Figures 62 and 63 one notes that the two morphologies qualitatively fit into the expected trend considering also the 45°C sample. Pn grown at 40°C forms big bottom islands and smaller on top; the islands are well connected and substrate seems fully covered. It appears clear that the early islands, nucleated on the LSMO surface, are bigger than the following nucleated on top of the previous ones: the nucleation rate for Pn on Pn is higher and the islands are smaller. Pn grown at 50°C forms bigger and well separated islands which resemble the films grown at 60°C. The height distribution function, reported in as example, gives 1,7 nm height steps for both these films.

Figure 62: 50°C Pn film on LSMO.

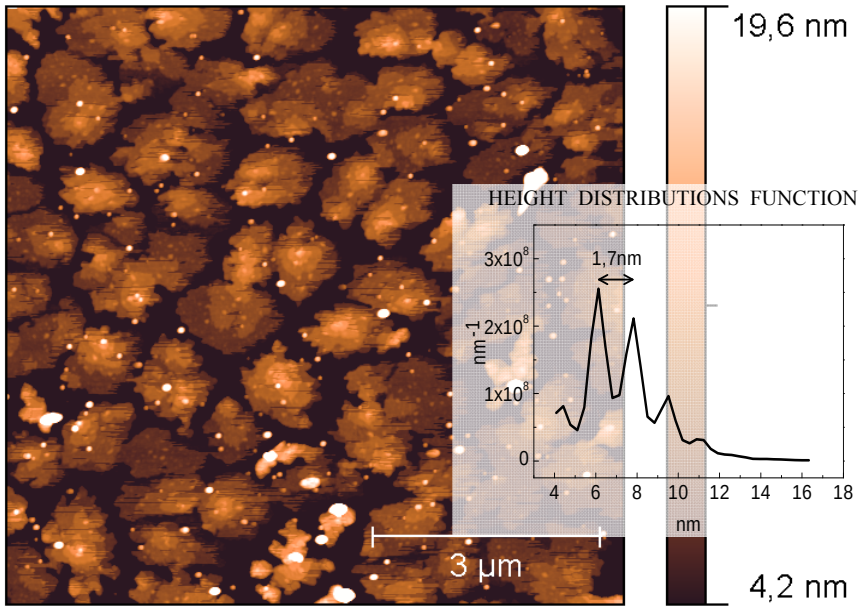

.

Additional analysis follows now in order to gain more insight. First, the data obtained from correlation and fractal analysis are described. This kind of processing let us to focus on the relevant parameters involved in the thin film formation.

Figure 63: temperature dependence of the correlation length ξ and the roughness exponent α.

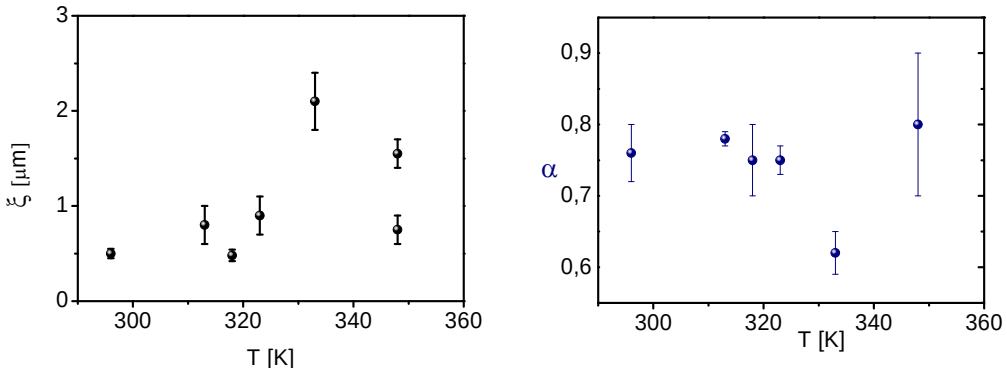

Correlation length ξ and roughness exponent α feature a complementary behavior in respect to the temperature (Figure 63). ξ increases with temperature, with a sort of jump at 45°C, but decreases again at 75°C. In the graph two values for ξ are reported at 75°C because two different values were extracted from HHCF for this sample.

The change in the trend at 75°C can be due to a very high re-evaporation rate. The same holds for the roughness exponent: increasing the deposition temperature the roughness exponent decreases, but at 75°C increases again. As it was done previously, the α values will be analyzed to

make a comparison with the theoretical model of surface evolution. The decrease of α towards 0,62 with increasing temperature means that diffusion becomes more and more relevant and anisotropic. The jump towards such an high value at 75°C could mean that desorption becomes more important.

A comparison between the coverage in films deposited at 45°C and 75°C confirms this assumption (Figure 64). It is measured by means of the grain analysis tool of the Gwyddion software. The software gives the projected area and the total volume of the grains. Comparing the coverages and thicknesses in Figure 64 a clear indication of a higher desorption at 75°C comes out.

Figure 64: Grain analysis confirms the desorption.

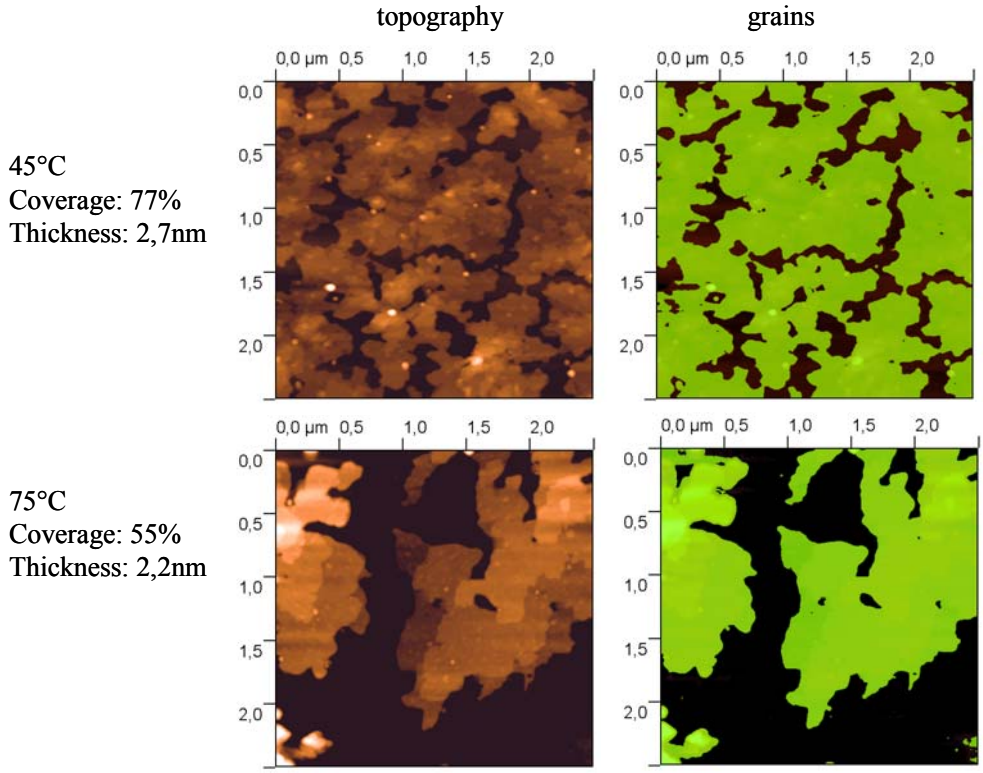

Another important finding is that D_f decreases from 2.3 to 2.17 when the deposition temperature raises up from 30°C to 75°C. A fractal dimension close to 2 means a more uniform and less ragged surface. It is reached increasing temperature possibly by an improved surface mobility of the impinging molecules. In 30°C deposited films D_f increases with the thickness. The first layers are well ordered and flat, while in thicker films the formation of islands leads to a rough surface with a three-dimensional development. Differently 60°C grown 3 nm thick and 100 nm thick films have the same D_f value: the "planarity" of the surface seems not to be lost.

ξ, α, and D_f indicates a strongly temperature activated, diffusion limited, growth mechanism. A transition in the nucleation mechanism happens at the LSMO substrate temperature of 45°C, since the absence of the disordered wetting layer and the multi-molecular first step, thanks to the increased thermal energy of the ad-molecules. The growth regime further evolves towards a desorption limited mechanism around LSMO temperature of 75°C. Speaking about condensation regime, as described in the section dedicated to thin film growth, a complete condensation takes place T < 75°C (with a transition in the nucleation path around 45°C), and becomes extreme incomplete at T ≥ 75°C. On SiO_2 the desorption becomes important at T ≥ 50°C[245], suggesting that the interaction between Pn and LSMO is similar, or a bit stronger than that with SiO_2 (this temperature difference corresponds to an energy difference of about 2 meV).

Figure 65: Picture of pentacene film evolution. Each layer consists of inclined molecules as sketche din the previous figure.

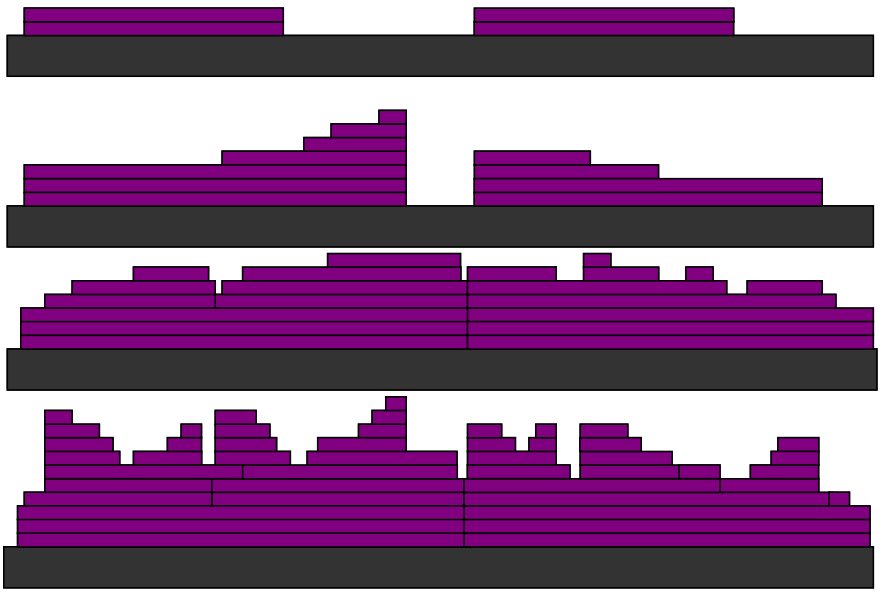

Figure 65 proposes a mechanism for Pn on LSMO growth considering the data on the time evolution at RT and 60°C and the temperature dependence on thinner films. Figure 65 applies for T > 45°C and the dark part represents the substrate. One can observe the represented rapid roughening of the surface: after a certain thickness the substrate effect vanishes. It is conceptually ascribed to the asymmetric sticking coefficient at step edge[246].

[245] S. Pratontep, F. Nüesch, L. Zuppiroli, M. Brinkmann, Phys. Rev. B, 2005, **72**, 085211
[246] Look at § 4.1.8 in J. Krim and G. Palasantzas, , J. Mod. Phys. B 1995, **9**, 599.

Activation energies for pentacene on LSMO

Looking for a quantitative analysis from the temperature dependent data, we studied the temperature dependence of the island density. From the fitting in Figure 66 a nucleation energy of 1,3 ± 0,2 eV is obtained. In order to maintain an Arrhenius trend we have to consider all the point at T ≥ 45°C and to exclude the other ones. This confirms the growth mode transition at 45°C. If we consider that at 45°C possibly the interaction with the substrate is broken and the amorphous wetting layer disappears, we can affirm that this is a transition in the nucleation mechanism, while the growth is still diffusion limited, as explained above. The different coverage for 5,5 min films deposited at RT and 60°C (compare Figure 44 and Figure 47) gives argument to the hypothesis of a transition from a complete towards an initially or extreme incomplete condensation regime.

Figure 66: T-dependence of island density and diffusion length.

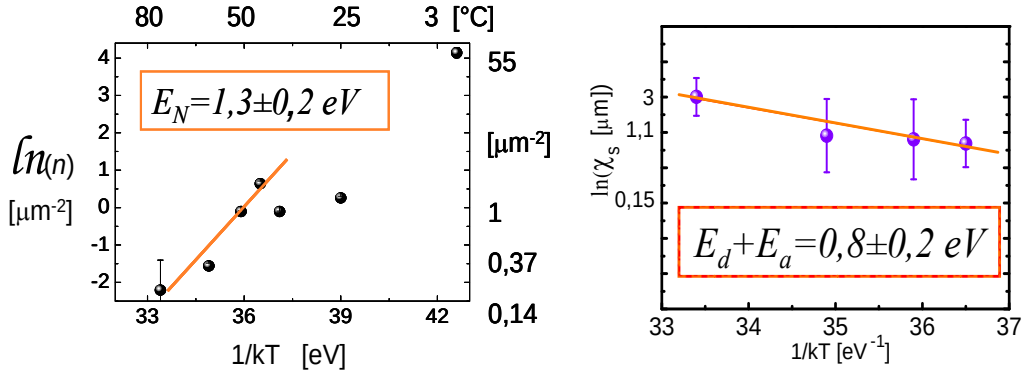

The measured E_N value can be compared with the energy found in the same range of temperature for Pn thin films grown on other oxide substrates. In fact the available data are very limited, thus the SiO_2 case is chosen as most studied substrate for applications in organic electronics. From literature we have found the values of E_N=*0,78±0,05eV* for a rate of 0,007 nm/s[247], which is similar to that used in the present experiment, while a value of E_N=*0,23±0,01eV* is deduced for a rate of 0,03nm/s[248], ten times higher than one proposed in the present work. In principle this value should be independent from the rate (according to a pure rate equation picture[249]) but Pratontep and co-workers found that the growth mechanism for Pn on SiO_2 are rate dependent: re-evaporation is more influent for slower rates[250].

At first sight it looks like pentacene nucleation on LSMO is very similar to that on SiO_2. But in the expression for E_N the nucleation energy, the diffusion barrier and the critical number of

[247] S. Pratontep, F. Nüesch, L. Zuppiroli, M. Brinkmann, Phys. Rev. B, 2005, **72**, 085211.
[248] M. Tejima, K. Kita, K. Kyuno, A. Toriumi, Appl. Phys. Lett. 2004, **85**, 3746.
[249] J. A. Venables, G. D. Spiller, M. Hanbücken, Rep. Progr. Phys. 1984, **47**, 399.
[250] S. Pratontep, M. Brinkmann, F. Nüesch, L. Zuppiroli, Phys. Rev. B 2004, **69**, 165201.

molecules play inter-related roles so that the variation of two parameters can compensate each other. Surely one can assert that Pn growth on LSMO is closer to that on SiO_2 than that on cobalt, but any further consideration does not seem straightforward.

The diffusion mechanism was analyzed in order to disentangle the diffusion and nucleation contributions. The surface diffusion length is defined as $\chi_s = \sqrt{D_s \tau_a}$, where D_s is the diffusion coefficient and τ_a is the residence time, i.e. the time the molecule moves on the substrate before to attach or to desorbs. It is traditionally calculated as the ratio between the first step eight and the rate[251], but it is known how the step height measurement from a hard surface (as LSMO is) to a soft one (as OSC are) by tapping mode AFM is affected by a great uncertainty intrinsically related to the technique[252]. Since the surface diffusion coefficient is expressed as $D_s = a^2 \nu \exp\left(E_d / kT\right)$ and $\tau_a = \nu^{-1} \exp\left(E_a / kT\right)$ where the terms a, ν, E_d and E_a are the jump distance, the jump rate, the activation energies for diffusion and re-evaporation, respectively, the diffusion distance is assumed to be $\chi_s \approx \exp\left((E_d + E_a)/2kT\right)$. Thus we plot the diffusion length versus 1/T. χ_s is estimated as the mean distance between the centre of the islands. Since the above consideration only the values for T ≥ 45°C are considered. The fitting (Figure 66) gives an energy barrier of 0,8 ± 0,2 eV.

For 45 °C ≤ T ≤ 75°C we are in a complete condensation regime, which is diffusion limited. Thus the value of 0,8 eV should be the energy barrier to the diffusion E_d. Calculations indicate that the interaction between two pentacene molecules is about 0,67 eV[253]. If so, dimer formation is favorite with respect to monomer diffusion, but this does not mean necessarily that a dimer is stable, as found when a model considering desorption has been applied to pentacene on silicon oxide[254]. Moreover, since the diffusion barrier is higher than the energy of a dimer, we can assert that Pn dimers diffuse on the top of LSMO surface.

Figure 67: sketch of energy paths for diffusion and dimer formation, dimer diffusion is possibile.

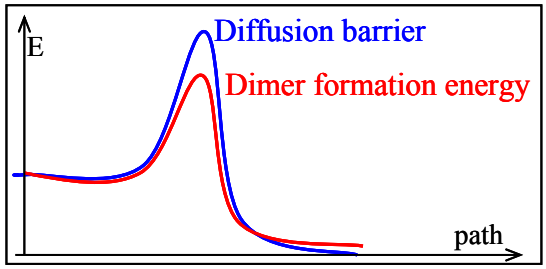

[251] B. Dam, B. Stauble-Pumpin, J. Mater. Sci.: Mater. Electron 1998, **9**, 217.
[252] P. Nemes-Incze, Z. Osvàth, K. Kamaràs, L.P. Birò, Carbon 2007, **45**, 3022.
[253] S. Pratontep *et al.* Phys. Rev. B 2005, cited
[254] S. Pratontep *et al.* Phys. Rev. B 2004, cited.

In the complete condensation regime $E_N = (E_i + i^* E_d)/i^*$. Inserting our data and considering i^*=2, that is E_N = 1,3 eV and E_d = 0,8 eV we obtain a dimer energy $E_2 \sim 1$ eV. This is somewhat close to the literature calculated 0,67 eV value. The discrepancy can be explained by involving the interfacial energy: on the LSMO surface the Pn dimer is not in vacuum, but it is *on* the LSMO surface, which owns a surface tension.

Assuming, on the other hand, $i^*=3$ leads to $\sum_{i=2}^{3} E_i \sim 1{,}5$ eV which would be the energy of formation of a trimer and is roughly double of the dimer energy. The trimer looks to us as a more convincing approach, since in a trimer formed by three stacked molecules facing two by two an interaction between the two outer molecules could happen. This agrees also with the 0,8 eV diffusion barrier energy: dimers are not stable and can diffuse (and dissocitae), trimers are stable and do not diffuse.

Pn/LSMO interface electronic structure

The electronic properties of the Pn/LSMO interface has been studied by Ultraviolet Photoemission Spectroscopy (UPS) and Near-Edge X-ray Adsorption Spectroscopy (NEXAFS) at the Linköping University by the Fahlman group[255]. The LSMO surface have been prepared in Bologna by the author and sent to Linköping University for Pn deposition and *in-situ* spectroscopy. The spectra will presented elsewhere and will not be shown in this thesis. UPS measurements reveal a dipole of about 0,1 eV for Pn/LSMO interface. It is close to the null dipole at the Pn/SiO_2 interface[256], and quite different from the Pn/Co (1 eV dipole) and Alq_3/LSMO (0,9 eV). Definitely manganite surface behaves as an inert oxide, not as a reactive metal, in respect to pentacene; the difference from the Alq_3 case is due to the huge intrinsic electric dipole of Alq_3, which Pn has not got.

NEXAFS investigated the electronic aspects of the film by measuring the adsorption of electromagnetic radiation by the electronic orbitals, by varying the incidence angle. The signal changes according to the equation $I = \frac{A}{3}(1+K) - \frac{AK}{2}\sin^2\theta$, where I is the intensity of the adsorption, A is a sort of analogous to the extinction coefficient, θ the angle between the beam and the film plane, $K=3\cos^2\alpha - 1$ is a fitting constant which gives the value of α, the angle of the vector orbital relative to the substrate normal. The intensity versus $\sin^2\theta$ plot indicates that the long axis

[255] F. Li, **P. Graziosi**, Q. Tang, Y. Zhan, X. Liu, V. Dediu, M. Fahlman, 2010 *submitted Phys. Rev. B.*
[256] H. Fukugawa, H. Yamane, T. Kataoka, S. Kera, M. Nakamura, K. Kudo, N. Ueno, Phys. Rev. B 2006, **73**, 245310.

of the molecule is inclined of about 20° relative to the substrate normal. This gives 1,5 nm steps, quite similar to that measured by AFM for the early steps: 1,4 nm.

Concluding notes and spin valves.

Pentacene thin film growth on LSMO surface is understood by involving pentacene molecules diffusion on the bare substrate; stable nuclei formation when a certain critical number of molecules meet; nuclei growth, migration, coalescence; molecule diffusion on top of nuclei. This is a standard picture for the inorganic thin film growth and it is acceptable also for pentacene films[257]. Pentacene film growth on the ferromagnetic oxide LSMO is a strictly diffusion limited and thermally activated (Arrhenius plot) process. At 30°C surface diffusion is very low and anisotropic, reflecting the intrinsic anisotropy of the pentacene molecule. Besides, when the temperature increases by just a few degrees, the ad-molecule mobility increases letting them to form very wide and extended flat islands having size of a few microns. These large structures are delimited by quite high steps: when the first molecules meet each other and build up a stable island, they stand up, because the molecule-molecule interaction is stronger than the molecule-LSMO one, and a few molecules high step is formed. Increasing the deposition temperature the molecule mobility on the surface increases drastically, but it keeps its anisotropic character; a change in the molecules orientation with respect to the surface normal takes place. Besides, a coarsening transition occurs after a certain thickness. At 60 °C deposition temperature this transition goes with a change in the film morphology, from terraced to lamellar.

Pentacene behavior on LSMO presents differences from that on Si, SiO_2, organic dielectrics[258] and cobalt[259]. This could be ascribed to the crystalline perovskite structure which is conserved also on the surface while thermally grown SiO_2 and spin coated organic dielectrics are both amorphous. Pentacene deposition on STO let us compare two perovskite surfaces. The island size follows the same trend in both the surfaces, but the islands are bigger when pentacene is deposited on STO. Moreover the terrace shape and size and the step height is different between film grown on STO and LSMO; the step height doesn't change significantly with the temperature. Due to these marked differences among the morphology of pentacene films deposited on cobalt,

[257] B. Stadlober, U. Haas, H. Marsch, A. Haase, Phys. Rev. B 2006, **74**,165302 ; M. Tejima, K. Kita, K. Kyuno, A. Toriumi, Appl. Phys. Lett. 2004, **85**, 3746; S. Pratontep, F. Nüesch, L. Zuppiroli, M. Brinkmann, Phys. Rev. B, 2005, **72**, 085211.

[258] T. Yokoyama, C.B. Park, K. Nagashio, K. Kita, A. Toriumi, Appl. Phys. Expr. 2008, **1**,041801; T. Toccoli, A. Pallaoro, M. Tonezzer, N. Coppedé, S. Iannotta, Solid State Electr. 2008, **52**, 417; R Ruiz, D Choudhary, B Nickel, T Toccoli, KC Chang, A.C. Mayer, P. Clancy, J. M. Blakely, R.L. Headrick, S. Iannotta, G. G. Malliaras Chem. Mater. 2004, **16**, 4497; B. Stadlober, U. Haas, H. Marsch, A. Haase, Phys. Rev. B 2006, **74**,165302.

[259] M. V. Tiba, W. J. M. de Jonge, and B. Koopmans, Journ. Appl. Phys. 2006, **100**, 093707; M. Popinciuc, H. T. Jonkman, B. J. van Waas, Journ. Appl. Phys. 2006, **100**, 093714.

LSMO, STO, Si, SiO_2 and various organic dielectrics, one has to consider that it is not possible to extrapolate a general pentacene behavior. A careful investigation the pentacene growth mode on the specific surface shall be performed.

From the point of view of the strength of the interactions, a very weak energy landscape was found at the pentacene/LSMO interface. Both morphological analysis and UPS measurements confirm a weak interaction between pentacene molecules and LSMO surface. Since it was shown that interfacial energetics is crucial to understand organic spintronics devices[260], we think what we found can be useful in the fabrication of pentacene based spin valves.

Prototypical pentacene-based spin valve devices were produced. The characterized structure was Co/Al_2O_3 (2nm)/Pn (100nm)/LSMO. They show negative magnetoresistance up to 300 K (-0,3%), but the device resistance is very low. The zero field resistance dependence on the temperature is semiconducting, which rules out the presence of shorts circuits; anyway the mound morphology let us suppose that the transport occurs ion thin regions between the islands reducing the effective transport distance between the electrodes. The two "V-shapes" (the global inverted "V" and that in the middle of the curve) are not yet understood. Since the low voltage used it is difficult they are due to Organic Magnetoresistance effect (OMAR)[261].

Figure 68: Pn based Spin Valve, -100 mV bias.

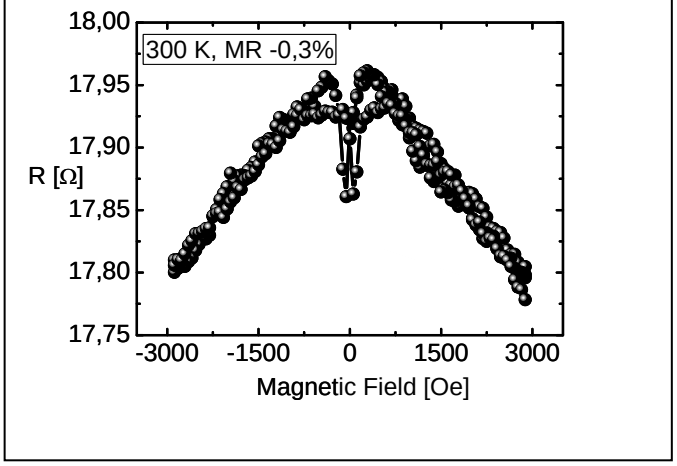

[260] V.Dediu, L.E. Hueso, I. Bergenti, A. Riminucci, F. Borgatti, **P. Graziosi**, C. Newby, F. casoli, M.P. De Jong, C. Taliani, Y. Zhan, Phys. Rev. B 2008, **78**, 115203.
[261] V. Dediu, L.E. Hueso, I. Bergenti, C. Taliani, Nat. Mat. 2009, **8**, 707.

4. Conclusions and final remarks

During the PhD course the author achieved few important and innovative results:

(1) New protocols have been developed for the growth of manganite films via Electron Beam Ablation technique (channel spark version, CSA). The main novelty consisted in a significant modification of the working gas pressure: it was doubled from $2 \cdot 10^{-2}$ mbar to $4 \cdot 10^{-2}$ mbar. This resulted in extremely low roughness surfaces, about 1 nm, similarly to the best reported in literature roughnesses (mainly achieved by PLD). At the same time the films maintain high and robust surface magnetic properties as ascertained by spectroscopic and transport investigations.

(2) The achievement of low roughness values for manganite films naturally led to a considerable improvement of sharpness at the bottom interface in LSMO based vertical devices.

(3) A radical modification of the top interface in vertical devices, that is the Alq_3/Co interface, was performed by inserting an insulating tunnel barrier of Al_2O_3. This interfacial buffer layer was found to provide a considerably improved reproducibility and improved interfacial and bulk ferromagnetism in the top electrodes. The growth and properties of the buffer layers and of the subsequent metallic layers were investigated in detail by different experimental techniques.

(4) The performed engineering of the interfaces and device components allowed to achieve stable room temperature operation of LSMO/Alq_3/Co vertical devices.

(5) The growth mechanism of pentacene organic semiconductor thin film on top of manganite layers was studied in a wide temperature interval and for different thicknesses. A transition from diffusion limited to desorption limited growth at about 75°C was observed. In addition, at 45°C the nucleation dynamics was found to switch from a disordered flat lying molecules to standing up interacting molecules.

This author acknowledges the financial support from EU-FP6-STRP under Grant No. 033370 OFSPIN. He is grateful to the whole stuff of the spintronic devices group at the ISMN-CNR, in particular Alek Dediu, Federico Bona, Ilaria Bergenti, Alberto Riminucci, Mirko Prezioso and Eugenio Lunedei for their invaluable help.

Patrizio Graziosi
patrizio.graziosi@gmail.com